

2023-07

Intelligent Interpretation of Geopotential Data for Subsurface Modeling

Bagheriashena, Zahra

Bagheriashena, Z. (2023). Intelligent interpretation of geopotential data for subsurface modeling (Doctoral thesis, University of Calgary, Calgary, Canada). Retrieved from <https://prism.ucalgary.ca>.
<https://hdl.handle.net/1880/116780>

Downloaded from PRISM Repository, University of Calgary

UNIVERSITY OF CALGARY

Intelligent Interpretation of Geopotential Data for Subsurface Modeling

by

Zahra Bagheriashena

A THESIS
SUBMITTED TO THE FACULTY OF GRADUATE STUDIES
IN PARTIAL FULFILMENT OF THE REQUIREMENTS FOR THE
DEGREE OF DOCTOR OF PHILOSOPHY

GRADUATE PROGRAM IN GEOMATICS ENGINEERING

CALGARY, ALBERTA

JULY, 2023

© Zahra Bagheriashena 2023

Abstract

Geophysical inversion involves determining the subsurface properties of the earth by analyzing geophysical data. Conventionally, geophysical inversions have encountered several challenges including non-unique solutions, nonlinearity, low-resolution and noisy data analyses, mandatory constraints and simplifications, computational costs, and subjective interpretations. Addressing these challenges necessitates the development of advanced inversion algorithms to enable a more comprehensive and robust analysis of subsurface properties.

Implementing deep neural networks, this thesis conducts nonlinear inversions of gravity and magnetic data for subsurface modeling by learning complex patterns and relationships in large training datasets. Nevertheless, a key challenge lies in the scarcity of large-scale training datasets required for the intelligent inversion problem. To address this issue, a novel technique has been developed to simulate geopotential datasets that represent the characteristics of real-world subsurface properties and their corresponding geopotential data. The technique's adaptability to diverse subsurface complexities allows for more comprehensive and accurate nonlinear inversion of geopotential data.

The dataset simulation technique adopts forward modeling to visualize the subsurface into crustal layers and incorporates physic-based constraints into the process. To ensure comprehensive coverage of geological complexities in the forward models, the technique incorporates multiple structural parameters. This results in randomized changes in the topography and depth of the subsurface layers. The forward model simulations are followed by calculating their synthetic gravity and magnetic anomalies. The final training dataset is created by putting together the calculated gravity and magnetic anomalies of the forward models as input features and the topography of the subsurface layers as labels.

The application of the proposed technique is practiced on airborne gravity and aeromagnetic anomalies offshore Abu Dhabi, United Arab Emirates. Using simulated datasets, several deep neural network models are trained to implement inversion of gravity anomalies, inversion of magnetic anomalies, and joint inversion of gravity and magnetic anomalies. The performance of the models is evaluated on actual and noise-added synthetic gravity and magnetic anomalies. By leveraging the trained models, the salts and basement structures are investigated, providing valuable insights into the geological structures of hydrocarbon reservoirs in this region.

Preface

This thesis is an original, unpublished, independent work by Zahra Bagheriashena.

Chapter four of this thesis has been presented as:

- Ashena, Zahra., Kabirzadeh, Hojjat., Wang, Xin., Kwon, Sun Il., Lee, Youngsoo., Ali, Mohammed., Kim, JW. Supervised Learning Analysis of gravity and magnetic data to predict potential regions of hydrocarbon reservoirs at offshore Abu Dhabi, UAE. Abu Dhabi International Petroleum Exhibition & Conference 15 - 18 Nov 2021.
- B. Ashena, Zahra., Kabirzadeh, Hojjat., Wang, Xin., Kim, JW. Clustering Analysis of a Geophysical Database for delineating regions of higher potential for hydrocarbon reservoirs. GeoConvention Conference, Calgary, Canada, August 31 - September 2, 2020.
- B. Ashena, Zahra., Kabirzadeh, Hojjat., Wang, Xin., Ali, Mohammed., Lee, Gyoo Ho., Woo, Ik., Kim, JW. Unsupervised Learning Analysis of a multi-parameter geophysical database for Abu Dhabi Hydrocarbon Reservoirs. Abu Dhabi International Petroleum Exhibition & Conference 11 - 14 Nov 2019.

Chapter five and chapter six of this thesis have been presented and published as:

- Ashena, Z., Kabirzadeh, H., Wang, X., Lee, Y., Woo, I., Ali, M., Kim, J.W., 2022. DNN Inversion of Gravity Anomalies for Basement Topography Mapping. Presented at the ADIPEC, OnePetro. <https://doi.org/10.2118/211800-MS>.

Chapters five through eight of this thesis have been submitted to two peer-reviewed journals:

- Ashena, Z., Kabirzadeh, H., Kim, J.W., Wang, X. and Ali, M, 2023, Joint Inversion of Gravity and Magnetic Anomalies to Image Salt-Basement Structures of Offshore Abu Dhabi, UAE using Deep Neural Networks, submitted to SPE (Society of Petroleum Engineers) Reservoir Evaluation & Engineering - Formation Evaluation, FE-0523-0009, in-review.
- Ashena, Z., Kabirzadeh, H., Kim, J.W., Wang, X. and Ali, M, 2023, A novel 2.5D Deep Network Inversion of Gravity Anomalies to Estimate Basement Topography, SPE (Society of Petroleum Engineers) Reservoir Evaluation & Engineering – Formation Evaluation. 1–14. SPE-211800-PA, <https://doi.org/10.2118/211800-PASPE-211800-PA> (reviewed among the top 20% of papers reviewed), June 30, 2023. (2.672, Q2)

Acknowledgments

I would like to express my deepest gratitude and appreciation to the individuals who have played a significant role in the completion of my thesis.

First and foremost, I am profoundly grateful to my esteemed supervisors, Dr. Jeong Woo Kim and Dr. Xin Wang for their invaluable expertise, insightful guidance, and continuous encouragement that empowered me to explore new frontiers in my research. I am truly appreciative of the opportunities they have provided me and the knowledge I have gained under their mentorship.

I am sincerely grateful to the members of my examination committee, Dr. Steve Liang, Dr. Elena Rangelova, Dr. Kangsoo Kim, and Dr. Nasser Kazemi. Their meticulous evaluation, constructive feedback and insights have immensely contributed to the refinement and quality of this thesis. I am sincerely grateful for their time, dedication, and expertise.

Additionally, I offer my sincerest gratitude to my colleagues and friends, Dr. Hojjat Kabirzadeh and Dr. Mohammad Javad Dehghan, for their unwavering support and significant assistance. Their insightful comments and collaboration have been precious in shaping my ideas and enhancing the overall quality of this work. Their friendship has made my Ph.D. journey more enjoyable and rewarding.

I would also like to acknowledge my dear friends Mandeep, Alborz, Babak, and Sina for their continuous support and presence throughout the challenging parts of this journey. Your encouragement, motivation, and belief in me have been a tremendous source of strength, helping me overcome obstacles and persevere.

Lastly, I extend my deepest thanks to my parents and siblings who have stood by me during this academic endeavor. Their understanding, encouragement, and steady belief in my abilities have been a constant source of inspiration. I am truly grateful for your love, support, and patience.

To my beloved sister, Leila, for being a shining example of what it means to be selfless, caring, and loving.

To my wonderful parents, for their endless love and support.

Contents

Abstract	ii
Preface	iii
Acknowledgments	iv
List of Figures	viii
List of Tables	xii
List of Abbreviations.....	xiii
List of Symbols	xiv
Chapter One: Introduction	1
1.1 Research Background	1
1.2 Research Objectives	7
1.3 Thesis Outline.....	9
Chapter Two: The Study Area.....	12
2.1 Geological Setting	12
2.2 Basement and Salt Structures of the UAE.....	12
2.3 The Geopotential Data.....	14
2.3.1 Airborne gravity data	15
2.3.2 Aeromagnetic data	16
Chapter Three: Machine Learning Analysis of Geopotential Data	18
3.1 Introduction	18
3.2 Clustering Analysis of the Ghasha Dataset	19
3.3 Supervised Learning Analysis of the Geopotential Data	22
3.4 Conclusion.....	24
Chapter Four: Geophysical Inversion using DNNs Techniques.....	26
4.1 Introduction	26
4.2 Conventional Geophysical Inversions	27
4.3 Deep Neural Networks Inversion	30
4.3.1 Model Evaluation.....	34
Chapter Five: Dataset Simulation for the DNN Inversion	37
5.1 Introduction	37
5.2 Forward Model Simulation.....	38
5.3 Geopotential Anomalies Calculation.....	41

5.3.1 Gravity Anomaly	41
5.3.2 Magnetic Anomaly	42
5.4 Conclusion	45
Chapter Six: DNN Inversion of Gravity Data	46
6.1 Introduction	46
6.2 Gravity Dataset Simulation	47
6.3 DNN Gravity Inversion	50
6.3.1 Error Analysis	51
6.4 DNN Gravity Model Evaluation	52
6.5 Results and Discussion	56
6.6 Conclusion	63
Chapter Seven: DNN Inversion of Magnetic Data	64
7.1 Introduction	64
7.2 Magnetic Dataset Simulation	64
7.3 DNN Magnetic Inversion	65
7.4 DNN Magnetic Model Evaluation	67
7.5 Results and Discussion	72
7.6 Conclusion	75
Chapter Eight: Joint DNN Inversion of Gravity and Magnetic Data	76
8.1 Introduction	76
8.2 Joint Gravity and Magnetic Dataset Simulation	77
8.3 DNN Joint Inversion of the Gravity and Magnetic Data	81
8.3.1 Error Analysis	81
8.4 DNN Joint Inversion Model Evaluation	82
8.5 Results and Discussion	83
8.6 Conclusion	93
Chapter Nine: Conclusion and Recommendations for Future Studies	94
9.1 Conclusion	94
9.2 Recommendations for Future Studies	97
References	100

List of Figures

Figure 2-1: Structural and tectonic map of the Arabian Plate, modified from Al-Husseini (2000); Martin (2001) and Stern and Johnson, (2010). The red polygon outlines the study area with the Jabal Dhanna highlighted with a blue star.	13
Figure 2-2: Study area in the western offshore Abu Dhabi, UAE.	15
Figure 2-3: (a) Bouguer gravity anomaly; (b) reduced-to-pole magnetic (DRTP) anomaly with hydrocarbon reservoir (oil-water) boundaries. The dotted white enclosures illustrate the boundaries of oilfields.....	17
Figure 3-1: The study area offshore Abu Dhabi, U.A.E. Ghasha region (right bottom blue box). Zakum region (left up purple box).	19
Figure 3-2: Clustering analysis results on Ghasha oilfield region, a) with two clusters; b) with three clusters.	21
Figure 3-3: (a) Prediction results of the logistic regression model. (b) Prediction results of the neural network model on the Zakum, Nasr, and Umm Shaif oilfields.	24
Figure 4-1: A deep feedforward network architecture comprising l hidden layers(h_1, h_2, \dots, h_l). with different numbers of units in each layer. d is the input vector and m is the output. $\theta(\theta_1, \theta_2, \dots, \theta_l + 1)$ is a learnable weight parameter matrix transmitting inputs through the hidden layers.....	31
Figure 4-2: The step-by-step research procedure.	36
Figure 5-1: Schematic view of the 2.5D forward model and observation points (red dots) on the surface.	39
Figure 5-2: An example of synthetic forward model simulation.	41
Figure 5-3: Geomagnetic field components.	43
Figure 6-1: Schematic view of 2.5D forward model and observation points (red dots) on the surface.	48
Figure 6-2: Samples of a simulated dataset. The red curve represents the synthetic gravity in mGal. The subsurface model is depicted with gray and dark blue colors, corresponding to sediments, and basement layers, respectively.	49
Figure 6-3: Plot of Training versus and validation accuracy against epochs.....	51
Figure 6-4: Samples of DNN gravity model prediction results. The red curve represents the synthetic gravity fed into the DNN model. The dashed blue curve represents the estimated gravity of the predicted subsurface structure. The predicted subsurface structure is depicted with gray, and dark blue colors, corresponding to sediments, and basement layers, respectively. The white dashed curve represents the actual basement topography.....	53

Figure 6-5: Samples of DNN model prediction results. The red curve represents the 5% Gaussian noise-added synthetic gravity anomaly fed into the DNN model. The dashed blue curve represents the estimated gravity anomaly of the predicted subsurface structure. The predicted subsurface structure is depicted with gray, and dark blue colors, corresponding to sediments, and basement layers, respectively. The white dashed curves represent true basement topography.... 54

Figure 6-6: Samples of DNN model prediction results. The red curve represents the 10% Gaussian noise-added synthetic gravity anomaly fed into the DNN model. The dashed blue curve represents the estimated gravity anomaly of the predicted subsurface structure. The predicted subsurface structure is depicted with gray, and dark blue colors, corresponding to sediments, and basement layers, respectively. The white dashed curves represent true basement topography.... 55

Figure 6-7: Location of the profiles over pseudo-gravity anomalies map of the study area together with its hydrocarbon reservoir (oil-water) boundaries. 57

Figure 6-8: Result of the DNN inverse model prediction across profile 1. The predicted subsurface structure is depicted with gray, and dark blue colors, corresponding to sediments, and basement layers, respectively..... 58

Figure 6-9: Result of the DNN inverse model prediction across profile 2. The predicted subsurface structure is depicted with gray, and dark blue colors, corresponding to sediments, and basement layers, respectively..... 59

Figure 6-10: Result of the DNN inverse model prediction across profile 3. The predicted subsurface structure is depicted with gray, and dark blue colors, corresponding to sediments, and basement layers, respectively..... 59

Figure 6-11: Representation of the 3 profiles, profile 1, profile 2, and profile 3..... 60

Figure 6-12: Basement topography estimation results using different density contrasts..... 61

Figure 7-1: Samples of a simulated dataset. The red curve represents the synthetic magnetic in nT. The subsurface model is depicted with magnetic and dark blue colors, corresponding to sediments, and basement layers, respectively..... 66

Figure 7-2: Plot of Training and validation accuracy against epochs. 68

Figure 7-3: Samples of DNN magnetic model prediction results. The red curve represents the synthetic magnetic fed into the DNN model. The dashed blue curve represents the estimated magnetic of the predicted subsurface structure. The predicted subsurface structure is depicted with gray and dark blue colors, corresponding to sediments and basement layers, respectively. The white dashed curve represents the actual basement topography. 69

Figure 7-4: Samples of DNN model prediction results. The red curve represents the 5% Gaussian noise-added synthetic magnetic anomaly fed into the DNN model. The dashed blue curve represents the estimated magnetic anomaly of the predicted subsurface structure. The predicted subsurface structure is depicted with gray and dark blue colors, corresponding to sediments and basement layers, respectively. The white dashed curves represent true basement topography. 70

Figure 7-5: Samples of DNN model prediction results. The red curve represents the 10% Gaussian noise-added synthetic magnetic anomaly fed into the DNN model. The dashed blue curve represents the estimated magnetic anomaly of the predicted subsurface structure. The predicted subsurface structure is depicted with gray and dark blue colors, corresponding to sediments and basement layers, respectively. The white dashed curves represent true basement topography.	71
Figure 7-6: Location of the profiles over pseudo-gravity anomalies map of the study area together. The dotted white enclosures illustrate the boundaries of oilfields.....	73
Figure 7-7: Result of the DNN inverse model prediction across Profile 1. The predicted subsurface structure is depicted with gray and dark blue colors, corresponding to sediments and basement layers, respectively.....	73
Figure 7-8: Result of the DNN inverse model prediction across Profile 2. The predicted subsurface structure is depicted with gray and dark blue colors, corresponding to sediments and basement layers, respectively.....	74
Figure 7-9: Result of the DNN inverse model prediction across Profile 3. The predicted subsurface structure is depicted with gray and dark blue colors, corresponding to sediments and basement layers, respectively.....	74
Figure 8-1: Samples of a simulated dataset. The red curve represents the synthetic gravity in mGal, and the blue curve represents the DRTP anomaly in nT. The subsurface model is depicted with gray, light blue, and dark blue colors, corresponding to sediments, salts, and basement layers, respectively.....	80
Figure 8-2: Plot of Training versus and validation accuracy against epochs.....	82
Figure 8-3: Samples of DNN model prediction results. The red curve represents the synthetic gravity and DRTP anomalies fed into the DNN model. The dashed blue curve represents the estimated gravity and magnetic anomalies of the predicted subsurface structure. The predicted subsurface structure is depicted with gray, light blue, and dark blue colors, corresponding to sediments, salts, and basement layers, respectively. The white dashed curves represent actual salt and basement topography.	84
Figure 8-4: Samples of DNN model prediction results. The red curve represents the 5% Gaussian noise-added synthetic gravity and DRTP anomalies fed into the DNN model. The dashed blue curve represents the estimated gravity and magnetic anomalies of the predicted subsurface structure. The predicted subsurface structure is depicted with gray, light blue, and dark blue colors, corresponding to sediments, salts, and basement layers, respectively. The white dashed curves represent true actual salt and basement topography.....	85
Figure 8-5: Samples of DNN model prediction results. The red curve represents the 10% Gaussian noise-added synthetic gravity and DRTP anomalies fed into the DNN model. The dashed blue curve represents the estimated gravity and magnetic anomalies of the predicted subsurface structure. The predicted subsurface structure is depicted with gray, light blue, and	

dark blue colors, corresponding to sediments, salts, and basement layers, respectively. The white dashed curves represent true actual salt and basement topography.	86
Figure 8-6: (a) Bouguer gravity anomaly; (b) reduced-to-pole magnetic (DRTP) anomaly. The dotted white enclosures illustrate the boundaries of oilfields. Profiles P1, P2, and P3 are used for the DNN joint inversion modeling.	87
Figure 8-7: Results of the DNN joint inversion model prediction across Profile 1. Sediments, salts, and basement are illustrated with gray, light blue, and dark blue colors, respectively.	89
Figure 8-8: Results of the DNN joint inversion model prediction across Profile 2. Sediments, salts, and basement are illustrated with gray, light blue, and dark blue colors, respectively.	89
Figure 8-9: Results of the DNN joint inversion model prediction across Profile 3. Sediments, salts, and basement are illustrated with gray, light blue, and dark blue colors, respectively.	90
Figure 8-10: Representation of the 3 profiles, profile 1, profile 2, and profile 3.	90
Figure 8-11: Basement topography estimation from magnetic inversion and joint gravity and magnetic inversion over Profile 1.	91
Figure 8-12: Basement topography estimation from magnetic inversion and joint gravity and magnetic inversion over Profile 2.	92
Figure 8-13: Basement topography estimation from magnetic inversion and joint gravity and magnetic inversion over Profile 3.	92

List of Tables

Table 3-1: Location of cluster centroids considering 2 clusters.	22
Table 3-2: Location of cluster centroids considering 3 clusters.	22
Table 6-1: Random parameter ranges of the forward models.....	48
Table 6-2: Density uncertainty analysis results on basement topography estimations.	61
Table 8-1: Random parameter ranges of the salt and basement layers considering a forward model with 80 km length.	79

List of Abbreviations

Abbreviations	Definition
ADNOC	Abu Dhabi National Oil Company
AI	Artificial Intelligence
AIRGrav	Airborne Inertially Referenced Gravimeter
ANNs	Artificial Neural Networks
CNNs	Convolutional Neural Networks
DNNs	Deep Neural Networks
DRTP	Differentially Reduced To Pole
ELU	Exponential Rectified Linear Unit
IGRF	International Geomagnetic Reference Field
ML	Machine Learning
MSE	Mean Squared Error
NE	Northeast
NW	Northwest
NN	Neural Network
ReLU	Rectified Linear Unit
RMSE	Root Mean Squared Error
RTP	Reduced To Pole
RC	Reservoir Characterization
SGD	Stochastic Gradient Descent
SGL	Sander Geophysics Limited
SE	Southeast
SVMs	Support Vector Machines
SW	Southwest
VES	Vertical Electrical Sounding
UAE	United Arab Emirates

List of Symbols

Symbols	Definition
h_a	Height of anomaly
B_0	Geomagnetic main field
C_l	Magnetic constant
M_I	Induced Magnetization
l_a	Length of anomaly
\hat{p}	Probability of class label \hat{y}
p_j	Center location of anomaly
G_{dnn}	DNN model
\hat{m}	Predicted subsurface model
μ_0	Vacuum magnetic permeability
ρ_j	Density of each prism
d	Dataset
E	Sum of squared error between objects in each cluster
G	Sensitivity function
h	Hidden layer
k	Number of Clusters
l	Number of layers
m	Subsurface model
n	Length of input data
mGal	Unit of Gravity field
nT	Unit of Magnetic field
p	Length of the outputs
X	Input matrix
Λ	Eigenvalue matrix

B	Total magnetic field
C	Cluster
D	Declination
I	Inclination
J	Objective function
Q	Covariance matrix
T	Anomalous magnetic field
$e(z)$	Exponential rectified linear unit function
$r(z)$	Rectified linear units function
γ	Gravitational constant
θ	Weight matrix
λ	Regularization parameter
μ	Centroid of Cluster
χ	Susceptibility
ϵ	Learning rate

Chapter One: Introduction

1.1 Research Background

Geophysical inversions apply the principles of physics and mathematics to transform geophysical data into models of subsurface properties (Camacho et al., 1999; Chunduru et al., 1997; Grana, 2020; Lines and Treitel, 1984; Oldenburg and Li, 2005; Sambridge, 1999; Sambridge et al., 2022; Tarantola, 2005). Such models are useful for mapping geological anomalies; for example, to identify potential reservoirs in oil and gas exploration. Depending on the choice of geophysical data and inversion technique, geophysical inversion can estimate a wide range of subsurface properties (Menke, 2018), for instance:

- Physical properties: density, magnetic susceptibility
- Structural properties: location and geometry of geological features such as sedimentary strata, basement structures and hydrocarbon reservoirs.

When applying geophysical inversions, it is important to bear in mind the associated challenges listed below:

- Geophysical inversion solutions are nonunique-i.e., different models can explain the observed data equally well.
- Accuracy and resolution of inversion results are affected by the physical formulation and quantity and quality of the geophysical data.

To address the issues listed above, inverse problems need to be constrained or simplified, which by itself may lead to further uncertainties in the solutions if not attentively carried out .

As briefed below, a variety of geophysical inversion techniques have been developed to solve ill-posed inverse problems:

- Regularization techniques apply constraints and smoothness to the problems to reduce non-uniqueness and avoid overfitting (Constable et al., 1987; Guillemoteau et al., 2022; Li and Oldenburg, 1996; Zhdanov, 2002).
- Bayesian inversion uses Bayes' theorem to compute a posterior distribution of the model parameters given the data. This involves specifying a prior distribution on the model

parameters and computing the likelihood of the data given the model (Grana, 2020; Izquierdo et al., 2020; Malinverno, 2002; Nawaz and Curtis, 2019; Sen and Stoffa, 1996).

- Joint inversion techniques conduct simultaneous inversion of different types of geophysical data to create more accurate solutions of the subsurface properties (Carrillo et al., 2022; Fregoso et al., 2020; Gallardo and Meju, 2007; ; Lin and Zhdanov, 2018; Gross, 2019; Haber and Oldenburg, 1997; Kabirzadeh et al., 2021)

The conventional inversion techniques listed above are based on direct mathematical and physical concepts and functions/calculations, making them prone to subjectivity and computational complexity, especially when dealing with large-scale datasets. Categorized under Artificial Intelligence (AI), Machine learning (ML) has introduced new approaches to geophysical processing and interpretation. ML techniques can learn the patterns and relationships that exist within large datasets and, often, provide more accurate results faster. As summarized below, ML techniques have been applied to a variety of geophysical datasets, including seismic, electromagnetic, and gravity data.

Neural networks (NNs) in geophysical applications are discussed in van der Baan and Jutten (2000). They described techniques to improve the performance of static and feedforward neural networks such as choice of neural network architecture, suitable preprocessing techniques, training algorithm and generalization measure, and configuration estimation. Following, they illustrated the performance of these techniques for the detection and extraction of reflections, ground roll, and other types of noise in a deep seismic reflection experiment.

Reservoir Characterization (RC) involves estimating petrophysical parameters of a reservoir, such as density, porosity, permeability, and water saturation, using well logs and seismic data. The heterogeneity of the subsurface makes it challenging and inefficient to estimate RC solely from well data. Seismic attributes provide information about the lateral variation of reservoir properties, making them valuable for RC prediction. In the study by Alfarraj and AlRegib (2018), Recurrent Neural Networks (RNNs) are used to train a model that approximates the functional relationship between seismic and log data. This involved using known reservoir properties and physical parameters from well data and seismic attributes at well locations to estimate density and p-wave impedance using artificial neural networks (ANNs) (Mohaghegh et al., 1996), Support Vector Machines (SVMs) (Akanle et al., 2015; Anifowose et al., 2015), conventional computational intelligence techniques and hybrid intelligent systems (Anifowose et

al., 2017). Machine learning techniques have been utilized in the detection of faults in seismic traces. Zhang et al. (2014) discussed an automated fault detection technique applied to pre-migrated seismic data. They constructed velocity models with varying fault parameters to generate a set of seismic traces. An ML classifier is then trained using these seismic traces to predict the presence or location of faults in unseen traces. In a study by Xiong et al. (2018), a Convolutional Neural Network (CNN) was employed to train a model using annotated seismic image cubes derived from field data. The training data was created by interpreters who label each point in the seismic image as either a fault or a non-fault feature. The trained CNN model is then used for fault detection in unseen seismic data. Araya-Polo et al. (2017) addressed the challenge of labeling fault locations by a limited number of domain experts, which can be impractical. To overcome this limitation, they generated synthetic 3D velocity models containing fault structures related to hydrocarbon reservoirs. From these synthetic models, thousands of random models were generated, and their corresponding seismic traces were derived using wave equations. This approach enables the creation of a larger dataset for training ML algorithms.

Seismic data interpolation is a technique used to reconstruct missing traces in sparsely distributed seismic records. Jia and Ma (2017) proposed the use of Support Vector Regression (SVR) for seismic data interpolation. They defined a regression hyperplane that relates the input data with missing traces to output completed data. The SVR technique is used to find the optimal regression hyperplane, which can then be utilized to interpolate the under-sampled seismic traces.

Microseismic methods have applications in different geoscience areas such as hydraulic fracturing monitoring, reservoir characterization, geothermal studies, and underground mines (Eaton., 2018). Zhang and van der Baan (2019) proposed a denoising method using an unsupervised learning algorithm and the Indian Buffet Process. The approach was learning a dictionary from the noisy data, which may contain missing traces. The signal of interest is then obtained by multiplying the dictionary with sparse coefficients derived from the Markov Chain Monte Carlo technique. (Chen, 2020) addressed the challenge of noise in arrival picking for weak microseismic or earthquake events. They applied ML to the recognition of seismic waveforms within the data. The fuzzy clustering algorithm clustered the time samples into waveform points and non-waveform points.

Since the early 1990s researchers have applied ML for geophysical inversion:

(Raiche, 1991) explored the application of ANNs as an adaptive pattern recognition paradigm to the inversion of geophysical data. They presented a philosophical exploration of adaptive pattern recognition paradigms for geophysical data inversion. It emphasized the adaptive nature of adaptive pattern recognition methods and their ability to handle incomplete data, noise, and data distortions. The application of adaptive pattern recognition to inversion was discussed within the context of NN implementations, considering input and output space representation concepts. The paper concluded that NN paradigms have reached a sufficient level of capability to warrant further research into implementing adaptive pattern recognition methods for geophysical inversion.

(Röth and Tarantola, 1994) used a NN to invert seismic reflection data for 1-D velocity models. The NN was designed to take a synthetic common shot, which is a set of seismograms obtained from a single seismic source, as its input pattern. The objective is to compute the corresponding one-dimensional large-scale velocity model as the network's output.

The research conducted by Devilee et al. (1999) addressed the application of NNs to solve nonlinear inverse problems in geophysics. Specifically, the study focused on determining the crustal thickness from surface wave velocities and obtaining a full posterior distribution of the crustal thickness. The paper discussed the advantages and limitations of using NNs for solving nonlinear inverse problems. Spichak and Popova (2000) investigated the 3-D inversion of geoelectric data by incorporating three layers of ANNs. Their synthetic model is composed of a dipping dyke in the bottom layer of two-layer earth in contact with the overburden. The model parameters were related to the dimensions and conductivity contrast of the dyke. They trained six ANNs, each having one output neuron corresponding to each model parameter. Then, they assessed the performance of the ANNs models on different hyperparameters.

ANNs are also applied to the geophysical inversion of vertical electrical sounding and seismic waveform data to obtain formations' resistivities and layer thicknesses (Calderón-Macías et al., 2001). The authors employed a two-layer feedforward neural network that was trained to predict earth models based on measured data. The training of feedforward neural networks involved using the back-propagation algorithm and a hybrid back-propagation-simulated-annealing method for the vertical electrical sounding and seismic inverse problems, respectively.

In their paper, Meier et al. (2007) presented a NN approach for inverting surface wave data to estimate the global model of crustal thickness along with corresponding uncertainties. The

authors proposed modeling the a posteriori probability distribution of Moho depth using a mixture of Gaussians, with the parameters of the mixture model determined by the outputs of a conventional NN. The NN was trained on a set of random samples to approximate the inverse relation in a compact and computationally efficient manner. The trained NNs were applied to real data, specifically fundamental mode Love and Rayleigh phase and group velocity maps.

The research paper by Das et al. (2018) explored the application of surrogate regression modeling for rapid seismogram generation and detection of microseismic events in heterogeneous velocity models. The study focused on the application of surrogate regression modeling using machine learning techniques to overcome the computational expense of solving the elastic wave equation. Synthetic simulations of forward seismic shots are conducted using a pseudo-spectral solution of the elastic wave equation on Graphics Processing Units (GPUs). These simulations served as the training data for the surrogate models, which were trained using machine learning techniques.

Following the classic research cases briefed above, recent studies explore further premises such as Deep Neural Networks (DNNs) and CNNs. In their paper, Puzyrev (2019) investigated the application of deep learning methods for electromagnetic inversion and proposed an approach for 2-D inversion based on fully CNNs. The training data set was generated by fully 3D simulations of models with different 2D resistivity anomalies.

(Yang and Ma, 2019) proposed a method for building velocity models from raw seismograms using a supervised deep fully CNN. They believed that the method eliminates the need for human interaction and quality control, and it is faster than traditional methods like tomography or full-waveform inversion. The deep-learning method was used to extract multilayer features automatically without the need for an initial velocity setup.

(Hu et al., 2021)) used DNNs to obtain the distribution of orebodies from the inversion of magnetic data. The authors used DNNs to recover the distribution of physical properties of buried magnetic orebodies from surface and airborne magnetic anomaly data. Two DNN structures were tested to assess the feasibility and generalization of the proposed method using two-dimensional (2D) synthetic examples. They believed that the predicted distribution of magnetization intensity obtained exhibits higher concentration and better resolution in determining the boundary of the magnetic body compared to conventional methods.

In another notable study, (Guo et al., 2021) created 3D images of subsurface geological structures by using CNN and regression models for the inversion of magnetic data. Using the PyNoddy library, they created a dataset comprising sample images of geological structures including faults and folds. CNN architecture was also been implemented for the 3D inversion of gravity data. The dataset was used to train their CNN model which was then applied to synthetic and real magnetic data.

In their study, Moghadas (2020) demonstrated an approach based on deep learning inversion via CNN to estimate subsurface electrical conductivity layering from electromagnetic induction data. The fully convolutional network was trained on a large synthetic data set generated using a 1D electromagnetic induction forward model. The accuracy of the model was assessed through various synthetic scenarios and was applied to real-world electromagnetic induction data. Huang et al. (2021) demonstrated the 3D density distribution of subsurface anomalies by conducting a sparse inversion of gravity data derived from image segmentation. They used the random walk method to simulate different geological models required to create the training set. Zhang and Curtis (2021) elaborated on the advantages of invertible NNs over neural mixture density networks as an alternative approach for solving geophysical inverse problems. They incorporated data uncertainties as additional model parameters and trained the network by maximizing the likelihood of the training data. The method was applied to two imaging problems: one-dimensional surface wave dispersion inversion and two-dimensional travel time tomography. The results were then compared to those obtained using Monte Carlo methods and mixture density networks.

(Rasht-Behesht et al., 2022) proposed a new approach to solve the wave propagation and full waveform inversions (FWIs) using physics-informed neural networks (PINNs) and tested the method with both forward models and full waveform inversion case studies. They believed that PINNs can solve wave propagation and FWIs by relying on information from governing partial differential laws when there is limited data available and can perform inversions with multiple events with limited additional memory or computational cost.

Inversion of large-scale geophysical data is a computationally challenging task. The conventional inversion techniques require gradient calculation of excessively large matrices. Based on the applied search algorithms, optimization methods are categorized as local or global techniques. Local optimization (or deterministic) algorithms start from an initial point and search

the misfit function downhill to find the minimum. The success of the algorithm to find the global minimum is dependent on the starting model. The deterministic methods are based on computing the gradient of misfit functions. Some of these algorithms are conjugate gradient, Newton's method and quasi-Newton methods that approximate the Hessian with past gradients. Global optimization (or stochastic) methods, unlike local minimum search approaches, seek the whole model space to find the global minimum thus well suited to quantify large data sets and estimate uncertainties. However, the computational cost of probabilistic analysis is notoriously high especially when searching for large model spaces (Sen and Stoffa, 2013).

All this motivates the development and practical use of new inversion methods that have modest computational demands while being robust and efficient.

1.2 Research Objectives

Conventional inversion techniques rely on mathematical and physical models to interpret the data. These methods can often be computationally expensive and require expert knowledge of the underlying physics and the ability to interpret the implications of the inverted parameters within the context of the problem. Geophysical inversion using ML techniques presents a promising alternative with several notable advantages. ML-based approaches have the capability to learn intricate nonlinear patterns and relationships within extensive datasets. This allows for faster and more accurate results compared to conventional inversion methods. ML inversion differs from conventional one in that it does not explicitly rely on physics-based models to interpret the data. Instead, ML techniques aim to learn the underlying patterns and relationships directly from the data itself, without explicit knowledge of the physics governing the system. Therefore, the physics is indirectly captured through the training data.

Despite the potential advantages of using ML techniques for geophysical inversion, several challenges need to be addressed:

- **Data quality and quantity:** One of the most significant challenges is the lack of high-quality data to train ML models. In geophysical inversion, ensuring data integrity, accuracy, and sufficiency becomes crucial for reliable ML model training.

Data integration: Simultaneous interpretation of multiple geophysical data types can be challenging and computationally expensive. Joint inversion involves integrating multiple geophysical datasets. A significant challenge is effectively combining these diverse datasets,

which often have different resolutions, sensitivities, and uncertainties. The ML algorithms used for joint inversion need to be efficient and scalable to handle the larger dataset and the increased computational requirements. This thesis addresses the challenges associated with geophysical inversion using ML techniques. It introduces a novel data simulation technique, applies DNNs for joint inversion of gravity and magnetic data, and develops a comprehensive software package for implementation and visualization. The thesis contributions provide a valuable framework for enhancing the accuracy and efficiency of geophysical inversion and offer insights into the subsurface structures for hydrocarbon exploration purposes in offshore UAE.

Some of the main objectives of this thesis are as follows:

- A novel technique is developed for simulating datasets required for DNN inversion of gravity data, inversion of magnetic data, and joint inversion of gravity and magnetic data. This flexible and adaptable technique allows for the simulation of large volumes of data in a short period of time, mitigating the issue of limited training data. The flexibility of the technique lies in its ability to accommodate diverse subsurface complexities. Moreover, the technique allows for parameter exploration and configurations based on the complexity of the subsurface such as the number of geological layers, presence of anomalies, and choice of priori parameters. One notable aspect of this technique is its flexibility, which allows for the simulation of diverse datasets across different geophysical methods. Whether it is gravity data, magnetic data, or a combination of both
- DNN inversions of gravity data and magnetic data are implemented to model the topography of basements adopting the dataset simulation technique.
- Addressing the challenges of combining multiple geophysical data, the joint inversion of gravity and magnetic data using DNNs is conducted to reduce the ambiguity and uncertainty of the inversion solution. The performance of the DNN models is evaluated on noise-free and noise-added data, ensuring the robustness of the proposed technique.
- To facilitate the implementation and usage of the developed technique, a comprehensive software package is developed and published (https://github.com/zara-ashena/GrvMag_DnnInv.git). This software package handles various aspects, including data simulation, DNN model training, model predictions, and visualization. It offers the flexibility to incorporate new data and test different hypotheses, providing a versatile tool for researchers and practitioners in the field.

- The application of proposed techniques has been applied to interpret the subsurface structures over hydrocarbon reservoirs in offshore United Arab Emirates (UAE). The main objectives include mapping the sedimentary stratum, determining the depth to the crystalline basement, delineating the surface of salt bodies, and predicting regions with a higher potential for hydrocarbon reservoirs.

By addressing the challenges and developing a robust and adaptable technique, this research contributes to the advancement of geophysical inversion using ML methods and provides valuable insights into hydrocarbon exploration and resource assessment in study regions.

1.3 Thesis Outline

The workflow of this thesis is summarized as follows:

Chapter one serves as an introduction, providing a background of the research objectives and outlining the content covered in subsequent chapters.

Chapter two delves into the geological setting of the study area, offshore Abu Dhabi, UAE. It explores the evolutionary history of the Arabian Plate and discusses the structures of its salts and basement. Additionally, this chapter provides an overview of the available airborne gravity and aeromagnetic data, including their coverage and resolution.

Chapter three introduces an innovative technique employed in this research to identify potential hydrocarbon reservoirs. Datasets are created using gravity data, magnetic data, and salt thickness information from offshore Abu Dhabi, UAE. ML techniques, such as clustering, logistic regression, and neural networks, are implemented on the dataset. Initially, a clustering approach is applied to partition the oil field regions into two areas with low and high hydrocarbon potential. The resulting clustered data are then used to train logistic regression and neural network classifiers, which are subsequently utilized to make predictions on unseen regions.

The principles of DNNs are explained in chapter four. The traditional inversion is compared to DNN inversion. The feedforward perceptron is used to construct the DNN architecture. For the DNN model to be trained, a set of hyperparameters need to be configured, including: the number of hidden layers and the units in each layer; an initializer to start the random weights of the layers; an activation function; the optimizer and its parameters including the learning rate; the regularization technique to avoid overfitting the model; and a loss function to measure the

difference between the network outputs and the actual labels. The chapter provides comprehensive descriptions of the DNN model architecture, training procedure, hyperparameter fine-tuning, and model evaluation.

Chapter five of this thesis presents the novel technique of dataset simulation required for the DNN inversion of geopotential data. Forward models are designed based on the target subsurface modeling objectives and are partitioned into two- or three-layers representing sediments, salts, and the basement. These layers are created by assembling rectangular prisms that are isolated from their surrounding geological environment. The forward model incorporates predefined physical parameters as well as random structural parameters. The step-by-step procedure for dataset simulation is meticulously outlined in this chapter.

In chapter six, a gravity inversion technique has been conducted to estimate basement topography. The training dataset is simulated by adopting the technique explained in chapter five. The forward model is partitioned into sediments and basement layers. Employing parallel computing algorithms, thousands of forward models of the subsurface with their corresponding gravity anomalies are simulated in a few minutes. A DNN model is trained based on the simulated dataset to conduct the nonlinear inverse mapping of gravity anomalies to basement topography in offshore Abu Dhabi, UAE. The performance of the trained model is assessed by making predictions on noise-free and noise-contaminated gravity data. Eventually, the DNN inversion model is employed to estimate the basement topography using pseudo-gravity anomalies.

Chapter seven investigates the estimation of basement topography using magnetic data. The same simulation procedures employed in chapter six are followed, including dataset simulation, DNN model training, and prediction on real case study data.

Chapter eight tackles the joint inversion of gravity and magnetic data. The training dataset simulation is presented considering a three-layer forward model of the subsurface, incorporating sediments, salts, and the basement. Utilizing multi-processing algorithms, thousands of training examples comprising gravity and magnetic anomalies as input features, and depth-to-salt and depth-to-basement as labels, are simulated. The proposed technique is applied to interpret salt-basement structures over hydrocarbon reservoirs in offshore UAE.

Lastly, chapter nine offers a summary of the techniques presented throughout the thesis and provides a comprehensive overview of the obtained results. Additionally, it offers conclusions drawn from this research and provides recommendations for future studies in the field.

Chapter Two: The Study Area

2.1 Geological Setting

The study area is in the western part of offshore Abu Dhabi, UAE, on the southern shore of the Persian Gulf (Figure 2-1). UAE is located in the northeast of the Arabian tectonic plate (Alsharhan, 1989). The Arabian Plate is bounded on its western side by the Dead Sea transform fault and the Red Sea spreading/rifting axis. Toward the northern and northeastern boundaries, it is bounded by the Anatolian fault and Zagros collision zone. On the eastern side, it is demarcated by the Makran Basin and Owen Fracture Zone. Finally, the southern extent of the Arabian Plate is defined by the Gulf of Aden spreading axis and Oman Mountains (Khattab, 1995; Stern and Johnson, 2010). The evolution of the Arabian plate includes several complicated geological events. From ca. 715 to 610 Ma, the Arabian Plate was involved in the Neoproterozoic compressional event that led to the formation of the Arabian margin of Gondwana. During Neoproterozoic to late Devonian (ca. 610 to 364 Ma) the Arabian Plate was located in northeastern Gondwana, which was separated from the Eurasian Plate by the Paleo-Tethys Ocean (Al-Husseini, 2000; Ali et al., 2017).

In the early Permian, the evolution of the Neo-Tethys Ocean initiated between the Eurasian Plate to the north and the north-eastern margin of the Arabian Plate. This process involved the emplacement of the Iranian microcontinent over the Eurasian Plate (Berberian and King, 1981; Searle et al., 2004). By the late Cretaceous, the closure of the Neo-Tethys Ocean was started. The collision of the Arabian Plate with the Iranian Plate during the Cenozoic led to the formation of the Zagros fold-and-thrust belt and the ongoing subduction of Arabia beneath Eurasia (Stern and Johnson, 2010). The collision led to the inclination of the Proterozoic basement toward the northeastward along the Zagros mountains while gradually deepening towards the Persian Gulf.

2.2 Basement and Salt Structures of the UAE

The crystalline basement of Arabia is exposed in the Arabian Shield, Yemen, and in the Dhofar region of Oman. The basement exposures are predominantly mid-Neoproterozoic in age and made up of highly deformed metamorphic rocks intruded by granitic dykes (Bowring et al., 2007; Mercolli et al., 2006; Nehlig et al., 2002).

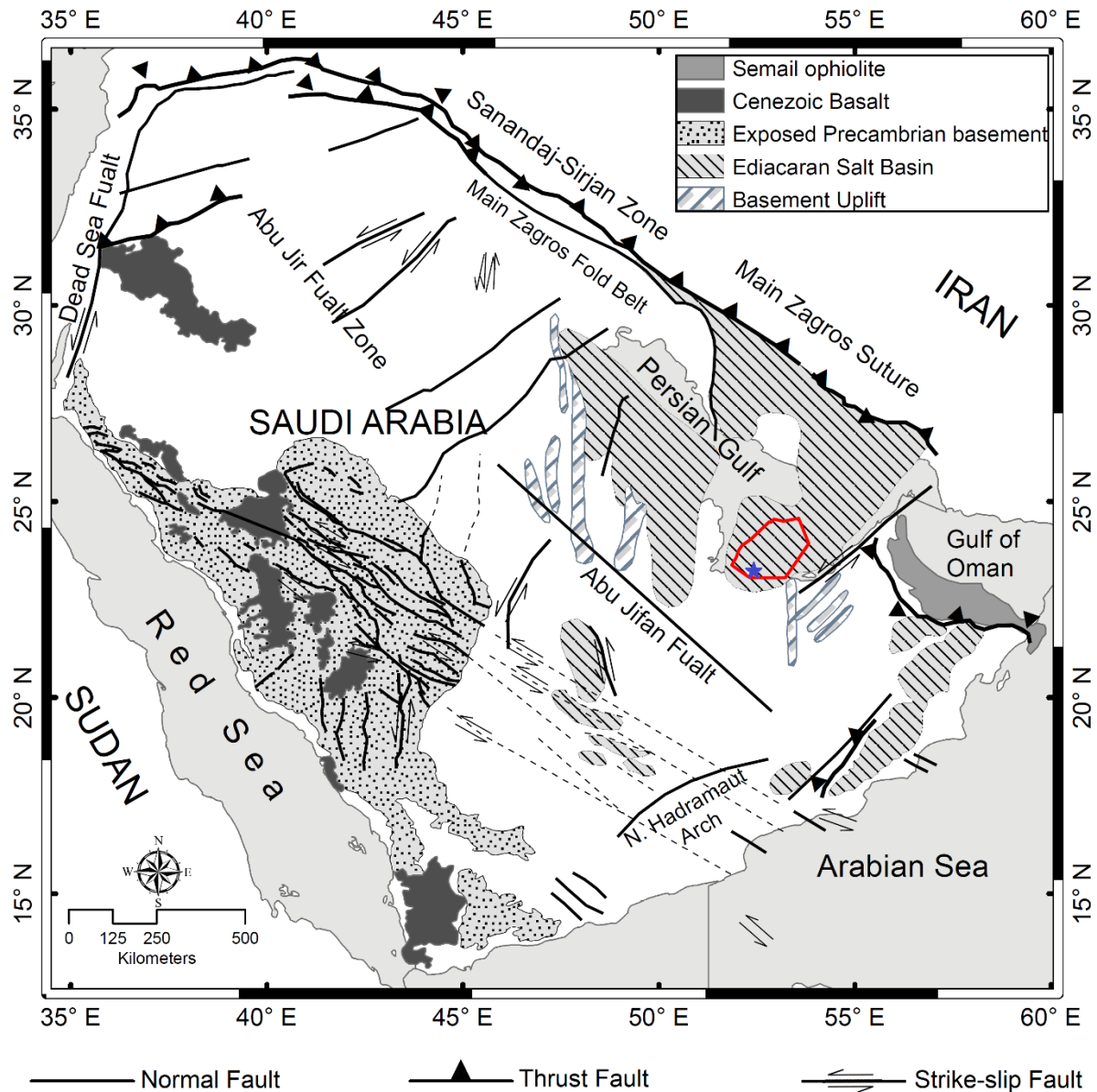


Figure 2-1: Structural and tectonic map of the Arabian Plate, modified from Al-Husseini (2000); Martin (2001), and Stern and Johnson, (2010). The red polygon outlines the study area with the Jabal Dhanna highlighted with a blue star.

The basement of the UAE is overlain by a thick sequence of volcanic and sedimentary Infracambrian rocks. The sedimentary strata contain successions of salt bodies that have formed as several diapiric salt islands offshore Abu Dhabi (Al-Husseini, 2000; Thomas et al., 2015). The salt diapirs originate from a thick succession of Ediacaran-Cambrian evaporates known as Hormuz salt. A compressional event that occurred during the Late Cretaceous period resulted in the mobilization of seated Infracambrian Hormuz salt bodies, folding of the overlying sediments,

and formation of domal oilfield structures (Ali and Farid, 2016; Kabirzadeh et al., 2021). The salt-related oil fields in the UAE exhibit distinctive features including dome-shaped structures, independent closures, radial faults within the structures, and a multi-step structural evolution. Prominent examples of such fields are Zakum, Umm Shaif, and Fateh. The salt domes contain exotic clasts of igneous, sedimentary, and low-grade metamorphic rocks of the Arabian basement that have been brought to the surface from depths of over 8 km (Al-Husseini, 2000; Thomas et al., 2015).

The categorization of oilfields in the UAE is based on the types of salt structures, specifically pillow and salt diapir structures (Alsharhan and Salah, 1997; Obaid et al., 2014). Low-relief salt pillows are closely associated with the most significant oilfields in the UAE including Zakum and Ghasha. The sedimentary trends observed above a salt pillow are typically depositional in nature; however, they are often complicated by closures resulting from faulting subsequent to burial, as is the case in the majority of offshore oil fields. The non-piercing high-relief salt diapir structures are characterized by sub-vertical, deep-seated faults with radial fault patterns that penetrate both deep and overlying shallower sedimentary sequences. Turtle structure anticlines are formed during the diapirs stage as observed in Dalma, Hair Dalma, and Mandous oilfields. During this stage, the salt is in close proximity to the surface, causing the previously deposited sediments above the diapir to experience uplift and erosion, leading to the formation of these distinctive anticlinal structures.

2.3 The Geopotential Data

The available geopotential data of the study area include airborne gravity and aeromagnetic anomalies (Ali et al. 2009) acquired by Sander Geophysics Limited (SGL) in 2007- 2008. The survey area is predominantly over the Persian Gulf and consists of almost the entire offshore part of Abu Dhabi (Figure 2-2). There is a small on-shore region along the south of the survey block which stretches for approximately 10 km inland. The survey area was bounded by the international boundaries with Qatar and Iran in the West and North respectively, and partially by the boundaries of neighboring Emirates in the East. In the offshore area, there are a number of islands, mostly located near the shore along the southern edge of the survey area, with a few located further out into the Persian Gulf.

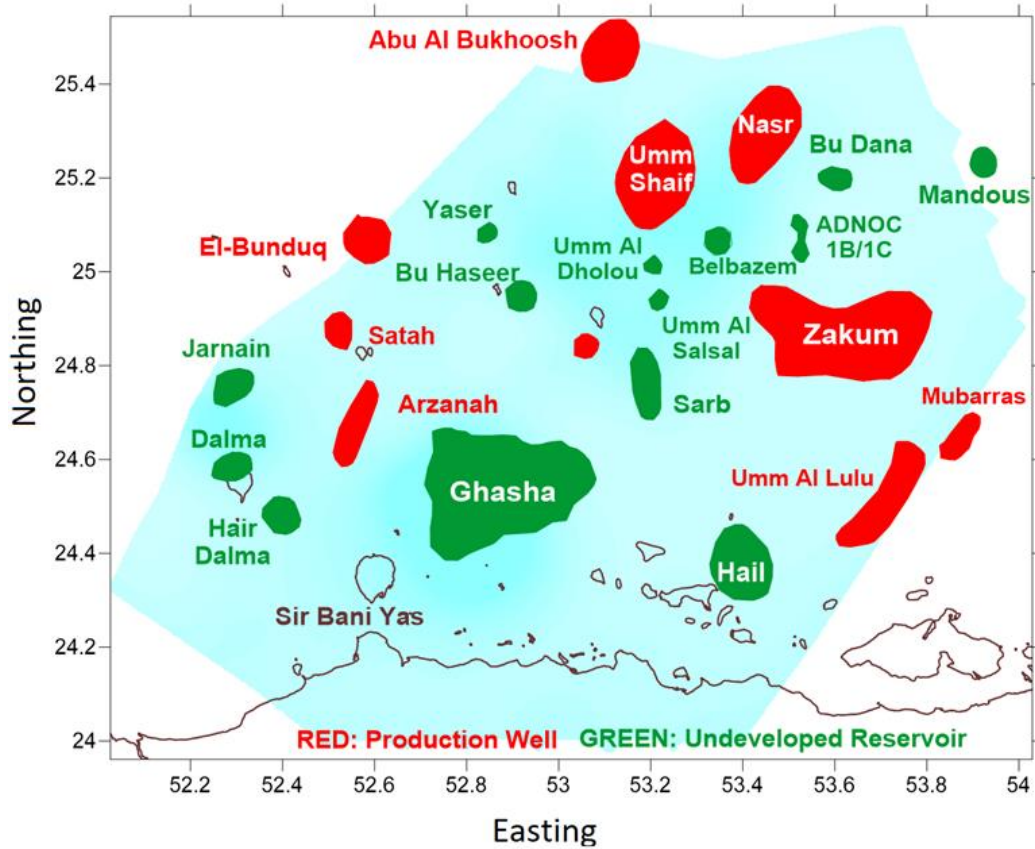


Figure 2-2: Study area in the western offshore Abu Dhabi, UAE.

2.3.1 Airborne gravity data

The high-resolution airborne gravity data was acquired by SGL using an airborne gravity system designated AIRGrav (Airborne Inertially Referenced Gravimeter). To obtain the complete Bouguer anomaly, several corrections, including the standard Eötvös, free air, slab Bouguer, the curvature of the earth, terrain, and static and level corrections, were applied to the gravity anomalies. Terrain correction was applied using Shuttle Radar Topography Mission data with a density of 2600 kg.m^3 for land areas and a density of 1020 kg.m^3 for sea water. The final data for the survey was filtered with a 3 km half-wavelength filter. The gravity anomalies illustrated in Figure 2-3a are gridded with a grid cell size of 1 km.

Ali et al. (2014), applied an upward continuation on the gravity data by removing the long wavelength regional component of the observed gravity to obtain the regional gravity.

The gravity anomaly map of the offshore UAE reflects the composite effects of the shallow and deep-seated density variations. Prominently, the map displays two significant gravity lows over the Zakum and Umm Shaif oilfields. Toward the west and northwest of the region, the

gravity anomalies exhibit higher values over Ghasha and some of the smaller oilfields including Bu Haseer, Satah, and Arzanah.

2.3.2 Aeromagnetic data

The aeromagnetic data was acquired by SGL using Caesium optically pumped magnetometers. Data were recorded at 10 Hz with a sensitivity of 0.001 nT and a sensor noise of 0.02 nT. The airborne survey was conducted at an altitude of 250 m above mean sea level with a total of 13,804 line-kilometers of data acquired with a survey line spacing of 2 km and a control line spacing of 10 km. Ground magnetometer data were inspected for cultural interference and edited as needed. All ground station magnetometer data were then filtered using a 67-point low-pass filter. The aeromagnetic data were corrected for diurnal variations by subtracting the corrected ground station data. Ground station magnetometer data were corrected for the International Geomagnetic Reference Field (IGRF) using the IGRF 2005 model and the fixed ground station location and the recorded date for each flight. Differentially-reduced-to-the-pole (DRTP) map is obtained after IGRF correction of aeromagnetic data, at a declination of 1.26° and an inclination of 37.16° . The DRTP map of the study area is shown in Figure 2-3b with a grid cell size of 1 km.

The high magnetic anomalies observed in the region primarily stem from the magnetic basement, which consists of a complex assemblage of microcontinents, magmatic arcs, accretionary wedges, and ophiolitic terranes. In contrast, sedimentary rocks generally have lower magnetic susceptibilities and therefore contribute less to the overall magnetic field.

The magnetic anomaly map of Figure 2-3b identifies three prominent magnetic highs coinciding with Ghasha and Umm Shaif, Sarb, and Dalma oilfields.

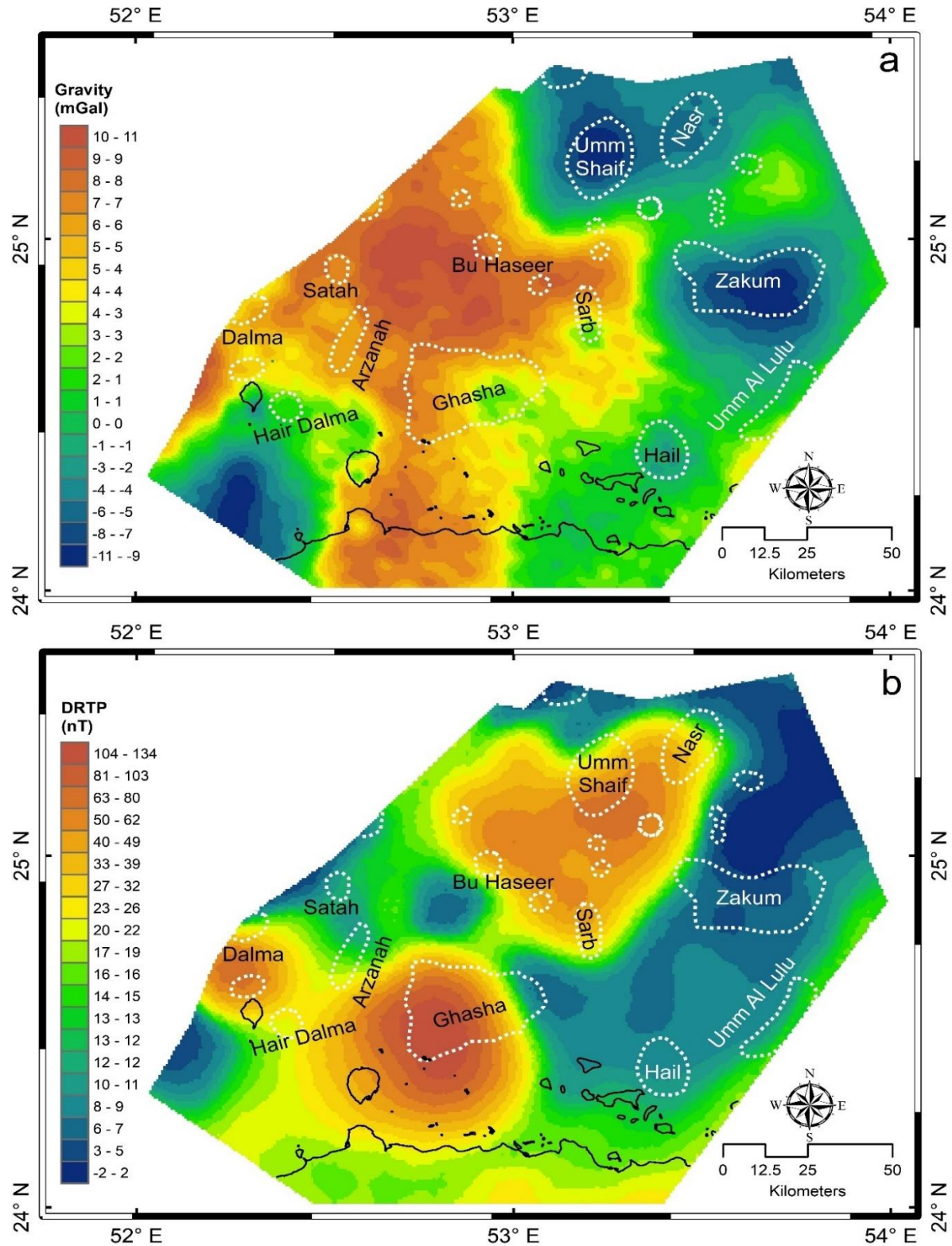


Figure 2-3: (a) Bouguer gravity anomaly; (b) reduced-to-pole magnetic (DRTP) anomaly with hydrocarbon reservoir (oil-water) boundaries. The dotted white enclosures illustrate the boundaries of oilfields.

Chapter Three: Machine Learning Analysis of Geopotential Data

3.1 Introduction

An innovative technique is implemented to delineate locations of potential hydrocarbon reservoirs offshore Abu Dhabi, UAE (B. Ashena et al., 2019). The region comprises approximately 8-10 km of crystalline sedimentary strata as part of the Arabian Plate, which is detached from the underlying basement by the latest Neoproterozoic–Lower Cambrian Hormuz evaporates (Ali et al., 2017) (Figure 3-1). Hormuz evaporates exposure as several salt domes offshore Abu Dhabi. Salt domes are specific geological features that are created when a buried salt layer with low density intruded upward into overlying denser sedimentary layers and arch them to shape a domed form (Hudec and Jackson, 2007). Due to their low-density contrast and almost zero magnetic susceptibility, salt structures can be detected by geopotential data analysis.

To identify potential hydrocarbon reservoirs, two datasets are created for the Ghasha and Zakum regions (Figure 3-1). The datasets include gravity, magnetic, depth to basement, and depth to Infracambrian salts. The basement and salt depths are obtained from 3D joint inversion modeling of gravity and magnetic data offshore Abu Dhabi (Kabirzadeh et al., 2021). A set of ML techniques are implemented on the datasets including clustering, logistic regression, and NNs to locate the regions of potential hydrocarbon reservoirs.

Initially, a clustering technique is applied to divide the Ghasha dataset into regions with low and high potential for hydrocarbons. Subsequently, the clustered Ghasha dataset is utilized to train two distinct machine learning models: logistic regression and NN. These trained models are then applied to predict the potential hydrocarbon regions over Zakum.

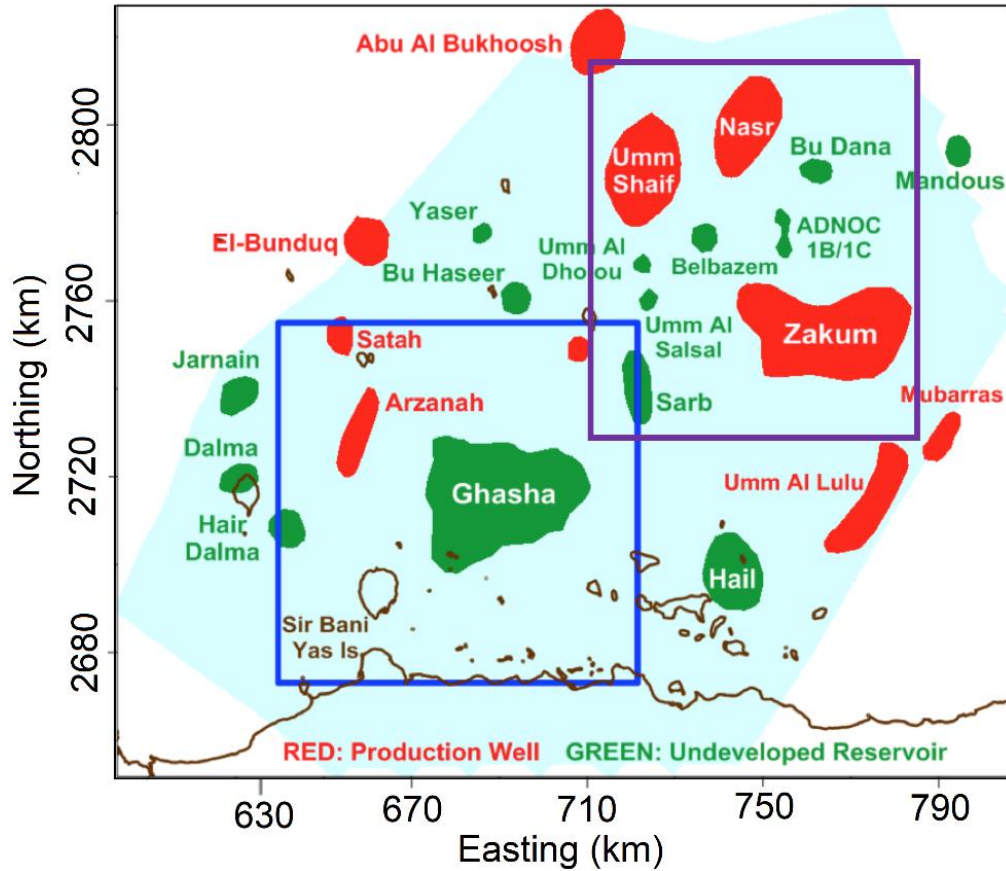


Figure 3-1: The study area offshore Abu Dhabi, U.A.E. Ghasha region (right bottom blue box). Zakum region (left up purple box).

3.2 Clustering Analysis of the Ghasha Dataset

Integrating different geophysical data and information that are sensitive to different physical and structural parameters in a single scheme result in more constrained and accurate geophysical interpretations. However, the interpretation of geophysical models is a challenging task in geophysics as it has been traditionally subjective, relying on the interpreter's knowledge. ML techniques can potentially provide effective automated interpretation tools by merging all information in a unified framework.

Clustering is an ML technique used in geophysical interpretation to identify spatial patterns and relationships within datasets (Florio and Lo Re, 2018; Melo and Li, 2016; Paasche et al., 2010; Song et al., 2010; Paasche and Eberle, 2009; Coléou et al., 2003). In this research K-means clustering technique (Di et al., 2018; MacQueen, 1965) is applied to delineate regions with higher potential of hydrocarbon reservoirs offshore Abu Dhabi, UAE.

The K-means clustering algorithm is a widely used method for partitioning observed data into distinct clusters. It aims to group similar objects by assigning them to the nearest centroid, which represents the mean value of the objects within the cluster. The algorithm proceeds as follows:

- Initially, k centroids are randomly placed in the data space.
- Each object is assigned to the nearest centroid based on a chosen distance measure, such as Euclidean distance. This step shapes the initial clusters C_1, C_2, \dots, C_k .
- The centroids are recalculated based on the objects within each cluster. The new centroids represent the mean values of the objects within their respective clusters.
- Steps 2 and 3 are repeated iteratively until a convergence criterion is met. The convergence criterion is typically based on the stability of the centroids and the assignments of objects to clusters.

Each cluster is represented by a centroid which is the mean value of the objects within the cluster, $\mu_i, i = 1, 2, \dots, k$. The distance between the objects $d \in C_i$ and centroids μ_i , are calculated by a distance measure $dist(d, \mu_i)$. The optimization procedure is to minimize the sum of squared error between objects in each cluster and their centroid μ_i .

$$E = \sum_{i=1}^k \sum_{d \in C_i} dist(d, \mu_i)^2 \quad (3.1)$$

To avoid a local optimum solution, the algorithm replicated several times by starting from different seed centroids and then the solution with the smallest sum-of squares-distances of the objects was chosen as a final solution.

The Ghasha dataset, \mathbf{D} , included 4 attributes: gravity, magnetics, depth-to-basement, and depth-to-salts. Before applying the clustering technique, each attribute $\mathbf{D}^{(j)}$ ($j = 1, 2, 3, 4$) is normalized $\mathbf{D}_{norm}^{(j)}$ to ranges with zero mean and covariance matrix given by the identity matrix (Klemelä, 2009).

$$\mathbf{D}_{norm}^{(j)} = \Lambda^{-1/2} Q^T (\mathbf{D}^{(j)} - \mu^{(j)}) \quad (3.2)$$

where the columns of Q are the eigenvectors obtained from the sample covariance matrix, Λ that is a diagonal matrix of the corresponding eigenvalues, $\mu^{(j)}$ is the mean value of each attribute.

The clustering algorithm is applied to divide the Ghasha oil field area into regions with low and high potential for hydrocarbons. To find the approximate number of clusters, the silhouette

index is implemented (Rousseeuw, 1987) which measures the compactness and separation of the clusters. Accordingly, the K-means technique is conducted considering two and three clusters. The results considering two clusters are shown in Figure 3-2a. The yellow cluster encompasses the majority of known oil fields in the region with smaller reservoirs mostly appearing at its border. Table 3-1 shows the properties of the cluster centroids. The cluster with a higher probability of hydrocarbon (yellow cluster) is related to shallower salts and basements and higher gravity and magnetic anomalies.

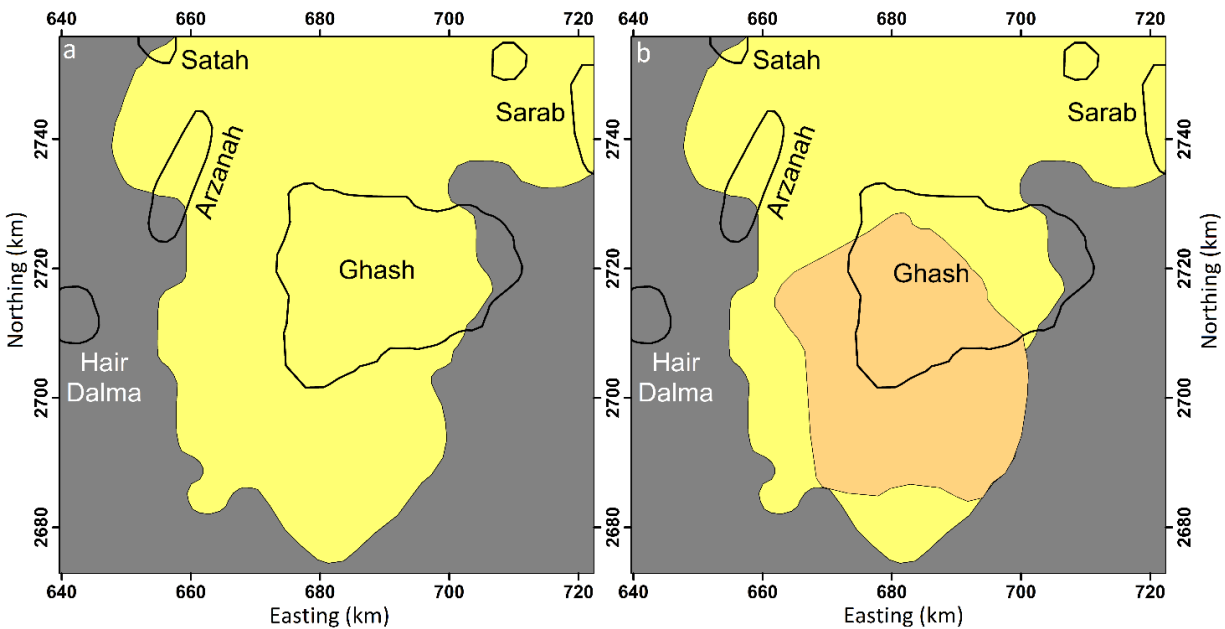


Figure 3-2: Clustering analysis results on Ghasha oilfield region, a) with two clusters; b) with three clusters.

The analysis of the Ghasha oil field and smaller oil fields within the Ghasha dataset reveals interesting geological characteristics. The presence of a giant oil field like Ghasha is likely associated with an anticline trap, which is a type of structural trap where hydrocarbons accumulate in an unfolded structure of rock layers. This suggests that the oil accumulation in Ghasha is primarily attributed to the structural deformation and folding of the subsurface rocks. In contrast, the smaller oil fields are located at the slope of the salt dome, indicating a probable fault trap mechanism. A fault trap occurs when hydrocarbons are trapped along the fault planes, which act as barriers to the upward migration of fluids. The presence of smaller oil fields in these areas suggests that the faulting and movement along the fault lines have created favorable conditions for hydrocarbon accumulation. The transition from positive to negative anomalies at the edges of the clusters provides further evidence for these geological interpretations.

Table 3-1: Location of cluster centroids considering 2 clusters.

Cluster	Gravity (mGal)	Magnetics (nT)	Depth-to-Basement(m)	Depth-to-Salt (m)
Gray	0.36	-280	-8,998	-8,100
Yellow	2.02	-253	-8,402	-7,325

The K-means clustering is applied to the Ghasha dataset considering 3 clusters. The results are illustrated in Figure 3-2b. Furthermore, the location of the cluster centroids is provided in Table 3-2. According to the results, the orange cluster dominates the central area of the map and roughly overlaps with the location of the Ghasha oilfield. The estimated values of the location of cluster centroids are interrelated for both clustering cases.

The high susceptibility metamorphic basement rises upward at some regions which causes picks on the magnetic anomaly map. However, the gravity anomaly map represents the composite gravity effects of various subsurface bodies, including sediments, salts, and the basement. In the case of the Ghasha region, the higher gravity anomaly can be indicative of a shallower basement, which masks the negative gravity anomaly associated with the salts in that particular region. On the other hand, the lower gravity anomaly over the Zakum oil field suggests the presence of a deeper basement and thicker salts in that area. These observations highlight the significance of gravity anomalies in identifying and characterizing different subsurface features and their relationship to potential hydrocarbon reservoirs.

Table 3-2: Location of cluster centroids considering 3 clusters.

Cluster	Gravity (mGal)	Magnetics (nT)	Depth-to-Basement (m)	Depth-to-Salt (m)
Orange	2.27	-275	-8691	-7747
Yellow	1.51	-208	-7781	-6502
Gray	0.03	-280	-9027	-8101

3.3 Supervised Learning Analysis of the Geopotential Data

To delineate regions with a higher probability of hydrocarbon using supervised learning, two separate databases for Ghasha and Zakum regions are created, each comprising three attributes: gravity, magnetic, and salt thickness. The k-means clustering is applied to the Ghasha dataset

considering 2 clusters (Figure 3-2a). The clustering result serves as the training dataset for the training ML models, comprising gravity, magnetic, and salt thickness as input features and the clusters' number as labels. By leveraging the knowledge gained from the clustering analysis on the Ghasha dataset, the models can provide insights into potential hydrocarbon reservoirs in the Zakum region.

Two ML models are trained including logistic regression and NN models. Logistic regression is an ML technique that aims to model the relationship between independent variables and a binary dependent variable. It transforms the linear combination of the independent variables into a probability value between 0 and 1, which represents the likelihood of belonging to a specific class. During training, the logistic regression model takes the training data as input through the input layer (Géron, 2019). The sum of weighted inputs X , is passed through the sigmoid activation function σ , to predict the probability of class label \hat{y} , 0 or 1,

$$\hat{p} = h_{\theta}(X) = \sigma(X^T \theta) \text{ and } \sigma(X^T \theta) = \frac{1}{1 + \exp(-X^T \theta)}$$

$$\hat{y} = \begin{cases} 0 & \text{if } \hat{p} < 0.5 \\ 1 & \text{if } \hat{p} \geq 0.5 \end{cases} \quad (3.3)$$

The NN model was trained using the Keras library, a high-level Application Programming Interface of TensorFlow developed by Google. The model hyperparameters are obtained through trial and error. Accordingly, a perceptron feedforward architecture is constructed from 2 hidden layers with 50 neurons in each layer and a binary output. Other hyperparameters include the sigmoid activation function; binary-cross-entropy loss function and “adam” optimizer with a learning rate of 0.001.

To assess the performance and accuracy of the models, the dataset is split into training and test sets. The training set contains 80% of the data, while the remaining 20% is used as the test set to calculate the generalization error. Additionally, a validation set, comprising 10% of the training set, is used to validate the model during the training process. After training the models for 30 epochs, the training accuracy and validation accuracy of the NN model reached 95% and 94% respectively. The test accuracy of the NN model, which indicates the model's performance on the test set, was 91%. In comparison, the logistic regression model achieved a score of 99% accuracy on the test set.

When applied to the Zakum dataset, both the logistic regression and NN models successfully identified the areas with a higher probability of hydrocarbon reservoirs, as indicated by the

yellow regions on the map (Figure 3-3). The models were able to roughly outline the oil fields boundaries, particularly the larger ones such as Zakum, Umm Shaif, Nasr, and Sarb. However, the NN model allocated a larger area to potential regions of hydrocarbon compared to the logistic regression model.

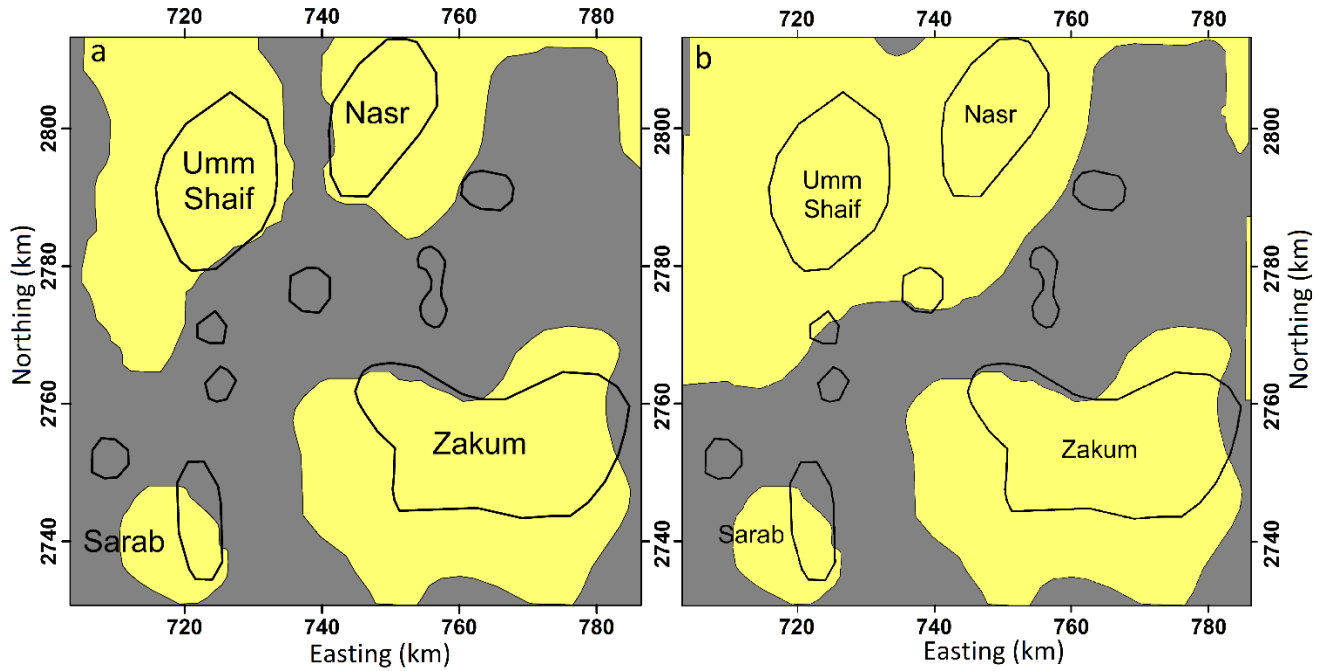


Figure 3-3: (a) Prediction results of the logistic regression model. (b) Prediction results of the neural network model on the Zakum, Nasr, and Umm Shaif oilfields.

3.4 Conclusion

In this study, multi-attribute potential field datasets comprising gravity and magnetic field anomalies and salt thickness were analyzed using various ML techniques, including k-means clustering, logistic regression, and NNs. The objective was to recognize the boundaries of the regions with high potential for hydrocarbon reservoirs offshore Abu Dhabi.

The clustering analysis divided the Ghasha database into two distinct clusters which were in good agreement with the location of known oil fields in that region. Ghasha was connected to high gravity and magnetic anomalies which demonstrates the effectiveness of the basement undulations in the generation of trapping structures.

Furthermore, the logistic regression and NN classifiers trained on the clustered outputs satisfactorily predicted the potential regions with hydrocarbon fields in acceptable agreement with the boundary of the known fields of the Zakum, Umm Shaif, Nasr, and, Sarb.

The findings indicate that by combining information derived from gravity and magnetic anomalies with the characterization of salt structures, valuable insights can be obtained regarding the probable locations of hydrocarbon fields. This information can be particularly useful in subsequent chapters of this thesis to guide the selection of profiles for the inversion of geopotential data regarding subsurface modeling.

Chapter Four: Geophysical Inversion using DNNs Techniques

4. 1 Introduction

Artificial Intelligence refers to the broad field of solving problems by computers that are intellectually difficult for humans (Goodfellow et al., 2016). It lets the computer learn from experience and establish rules based on the provided knowledge. One of the challenging tasks of artificial intelligence is to devise ways to present intuitive knowledge of the world to computer languages. In knowledge base approaches to artificial intelligence, humans encode knowledge to computers to infer logical inference rules. The hard-coded knowledge base approaches have the drawback of being subjective which typically deteriorates the solution. ML methods overcome this difficulty by automatically extracting knowledge from the raw data. However, their performance depends on how data are represented to the system, or in other words to the different information (i.e., features) in the representation. Therefore, some features are extracted from the data and mapped to the outputs through the machine learning system.

Choosing the right set of features is challenging for many artificial intelligence tasks. A viable remedy to this problem, rather than manual feature extraction, is applying a representation learning technique that can detect a set of features for any complicated task. In real-world cases, we may have high-level abstract features which cannot be easily extracted by representation learning methods that input features to outputs. Deep learning technique, as a type of machine learning, introduces a remedy to this problem, by creating complex features from simpler ones. From the input layer, simple features are extracted which contain information in the observed data, also known as the visible layer. It is followed by a series of hidden layers to extract abstract and complex features of simpler representations in sequence. Following a detailed description of DNNs is presented.

This research has employed the DNN technique to conduct nonlinear inversion of gravity and magnetic data. Geophysical inversions are the techniques for simulating the physical and structural characteristics of the subsurface model using the observed geophysical data.

Conventional geophysical inversion differs from deep neural network inversion in the method they use to solve the inverse problem. Conventional geophysical inversion involves formulating an inverse problem as an optimization problem, where the objective is to minimize the misfit between the observed data and the predicted data using a forward model. This approach typically

involves selecting an appropriate regularization parameter to balance the misfit and regularization term such as the smoothness.

Deep neural network inversion, on the other hand, uses a deep neural network to directly learn the mapping between geophysical data and subsurface properties. This involves training the network using a large dataset of geophysical data and corresponding subsurface models. Once trained, the network can be used to predict subsurface properties from new geophysical data.

One advantage of deep neural network inversion is that it can handle complex non-linear relationships between geophysical data and subsurface properties, which can be difficult to capture using conventional inversion methods. Additionally, deep neural network inversion does not require explicit knowledge of the physical relationships between the geophysical data and subsurface properties, making it a more general approach. Instead, it uses a neural network model to learn the complex relationships between the input geophysical data and the output subsurface properties.

4.2 Conventional Geophysical Inversions

Geophysical inversion involves the development of mathematical techniques aimed at modeling subsurface physical and structural parameters based on surface geophysical data. The relation between the subsurface model (\mathbf{m}) and observed data (\mathbf{d}) is defined through the following general mathematical model (Aster et al., 2019).

$$\mathbf{d} = G(\mathbf{m}) \quad (4.1)$$

The function G which describes the physical process of mapping the model space to data space is known as sensitivity or Jacobian matrix. It can take different forms based on the linear or nonlinear relationship between data and the subsurface model. The inverse problem determines the subsurface model

$$\mathbf{m} = G^{-1}(\mathbf{d}) \quad (4.2)$$

by minimizing a loss function of the residual between observed data \mathbf{d} , and the mathematical model $G\mathbf{m}$.

$$\mathbf{r} = \mathbf{d} - G\mathbf{m} \quad (4.3)$$

In the context of linear inverse problems, the operator G is often represented as a linear kernel. When dealing with real-world scenarios, the observed data is typically affected by some level of noise. In this case, the general linear mathematical model can be expressed as the sum of

noiseless data, d_{true} and a noise component. The noise component accounts for the random fluctuations or errors that are present in the measured data.

$$\mathbf{d} = G\mathbf{m}_{true} + \mathbf{n} = \mathbf{d}_{true} + \mathbf{n} \quad (4.4)$$

Noise characteristics are not usually known, and hence it becomes necessary to make certain assumptions about its statistical distribution. Therefore, we assume data as a random variable whose statistical characteristics are known.

As a solution, we seek the best model \mathbf{m} , given observations \mathbf{d} , that maximize a likelihood function. Consider the special case when G is full rank (i.e., overdetermined problems) and data errors are independent and normally distributed with zero-mean and covariance matrix of $C^{(d)}$. The joint probability density for a vector of independent observations \mathbf{d} will be

$$f(\mathbf{d}|\mathbf{m}) = f_1(d_1|\mathbf{m}) f_2(d_2|\mathbf{m}) \dots f_m(d_m|\mathbf{m}), \quad (4.5)$$

and the probability density of each data point d_i , $i = 1, 2, \dots, m$ is defined as

$$f_i(d_i|\mathbf{m}) = \frac{1}{(2\pi)^{1/2} \sigma_i} e^{-(d_i - (G\mathbf{m})_i)^2 / 2\sigma_i^2} \quad (4.6)$$

The likelihood function for the complete data set takes the following form.

$$L(\mathbf{m}|\mathbf{d}) = \frac{1}{(2\pi)^{m/2} \prod_{i=1}^m \sigma_i} \prod_{i=1}^m e^{-(d_i - (G\mathbf{m})_i)^2 / 2\sigma_i^2} \quad (4.7)$$

By maximizing the likelihood function, the problem becomes independent and Gaussian-distributed, then the maximum likelihood principal solution is the weighted least squares solution.

$$\mathbf{m}_{ML} = (G^T C^{(d)-1} G)^{-1} G^T C^{(d)-1} \mathbf{d} \quad (4.8)$$

The function G , is typically ranked deficient. This results in ill-posed geophysical inverse problems. Moreover, geophysical inversion solutions are nonunique which means infinite solutions may fit the data. To address these issues, regularisation is used to stabilize ill-posed inverse problems by introducing prior information about the model in the loss function, such as the minimum norm solution.

$$\min ||G\mathbf{m} - \mathbf{d}||_2^2 + \lambda ||\mathbf{m}||_2^2 \quad (4.9)$$

where λ is the regularization parameter.

The optimization process concerns minimizing the loss function to find the optimal values for the model parameters that best match the observed data and provide the most accurate representation of the subsurface (Sen and Stoffa, 2013). The loss function of nonlinear problems can take a complicated form including several minima and maxima. For solving nonlinear

problems $\mathbf{d} = G(\mathbf{m})$, a common approach is to linearize the mathematical function using a Taylor series expansion around a starting model, m_0

$$G(m_0 + \Delta m) = G(m_0) + J(m_0) \Delta m \quad (4.10)$$

where $J(m_0)$ is the Jacobian of partial derivatives evaluated at m_0 .

Applying linear theory to evaluate posterior properties may be suitable for weakly nonlinear problems. The posterior covariance matrix for nonlinear inversion is not exact and it depends on the accuracy of the linearization.

Regarding fully nonlinear inverse problems, the Bayesian inversion technique is an alternative to the classical approach which defines a probability distribution for the model parameters (Izquierdo et al., 2020; Rossi et al., 2016; Sen and Stoffa, 1996). Bayesian inversion provides a framework for integrating prior information about the probability distribution of the model, denoted as $p(\mathbf{m})$ which is independent of data information. By considering both the data and the model as random variables, we can quantify the likelihood, $p(\mathbf{d}|\mathbf{m})$ which represents the probability of observing the data, \mathbf{d} given a particular model, \mathbf{m} . The posterior probability distribution of model parameters $p(\mathbf{m}|\mathbf{d})$ given the data can be obtained from Bayes' theorem (Aster et al., 2018).

$$p(\mathbf{m}|\mathbf{d}) = \frac{p(\mathbf{d}|\mathbf{m})p(\mathbf{m})}{p(\mathbf{d})} \quad (4.11)$$

This posterior distribution represents our updated knowledge about the model parameters considering the available data. The model parameters are estimated by maximizing the posterior as

$$m_{MAP} = \text{Arg}_{max} \{p(\mathbf{m}|\mathbf{d})\} \quad (4.12)$$

or mean model

$$\bar{m} = \int \mathbf{m} p(\mathbf{m}|\mathbf{d}) d\mathbf{m} \quad (4.13)$$

which requires numerical optimization and integration. The integration is conducted through a point-wise evaluation of the posterior over parameter space, which is known as Bayesian sampling. The global optimization methods, Simulated Annealing, and Genetic algorithms are examples of random walk sampling methods (Boschetti et al., 1996; Farrell et al., 1996; Putra et al., 2019; Sambridge and Mosegaard, 2002; Sen and Stoffa, 1991).

4.3 Deep Neural Networks Inversion

The intelligent inversion through the DNN technique has a notable difference from the conventional definition. In this case, the sensitivity function refers to the DNN model to be determined. In other words, given a training dataset, a DNN model is trained by approximating weight parameters θ . Later, we use the DNN model G_{dnn} , to conduct nonlinear mapping from the geophysical data \mathbf{d} to subsurface model \mathbf{m}

$$\mathbf{m} = G_{dnn}(\mathbf{d}; \theta) \quad (4.14)$$

To train a DNN model we need to design the architecture of the network, including the number of layers, the number of nodes of each layer, how these layers should be connected to each other, the activation function, optimization parameters, etc.

Perceptron feedforward architecture has been used to construct and train our DNN model (Figure 4-1). In the feedforward model, information flows from input (geophysical data) to output (subsurface model), while there are no feedback connections from the outputs (Raiche, 1991).

Deep feedforward networks comprise l hidden layers that are connected in a chain structure whose length defines the depth of the model. Each hidden layer has a vector of hidden units that are input to the proceeding layer and are computed by functions $\mathbf{h}_1 = G^{(1)}(\mathbf{d}, \theta^1)$, $\mathbf{h}_2 = G^{(2)}(\mathbf{h}_1, \theta^2), \dots \mathbf{h}_l = G^{(l)}(\mathbf{h}_{l-1}, \theta^l)$. The output layer is $\hat{\mathbf{m}} = G_{dnn}(\mathbf{d}; \theta) = G^{(l+1)}(\mathbf{h}_l, \theta^{l+1})$. The complete model $G_{dnn}(\mathbf{d}; \theta) = G^{(l+1)} \dots (G^{(2)}(G^{(1)}(\mathbf{d}; \theta^1)))$ is obtained by learning the weight parameters.

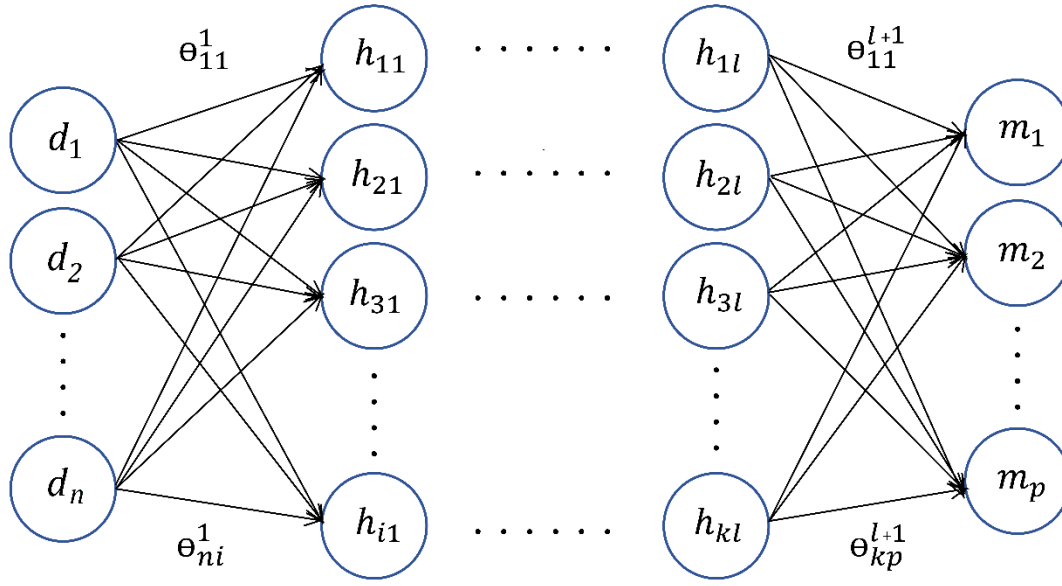


Figure 4-1: A deep feedforward network architecture comprising l hidden layers (h_1, h_2, \dots, h_l), with different numbers of units in each layer. d is the input vector and m is the output. $\theta(\theta^1, \theta^2, \dots, \theta^{l+1})$ is a learnable weight parameter matrix transmitting inputs through the hidden layers.

The training data are constructed from a combination of the geophysical data $\mathbf{d}_i, i = 1, 2, \dots, n$ and their associated labels $\mathbf{m}_j, j = 1, 2, \dots, p$. The input data are fed into the network through the input layer. The sum of weighted inputs is passed through an activation function to compute the outputs. The activation function is a nonlinear function that can take different forms for each hidden layer $\mathbf{G}^{(1)}, \mathbf{G}^{(2)}, \dots, \mathbf{G}^{(l+1)}$. The rectified linear unit (ReLU) is commonly used as the activation function of the hidden units (Glorot et al., 2011). One drawback to rectified linear units, $r(z) = \max\{0, z\}$ is that for $z < 0$ they output zero. Therefore, while using gradient-based methods, the algorithm cannot learn whenever activation is zero. Exponential rectified linear unit (ELU) is similar to ReLU except that it has negative values that bring the mean of activations closer to zero and so enable faster learning. Bringing the mean of activations closer to zero helps prevent the dying neuron problem, promotes smooth and continuous gradients, and aligns the activations with the data distribution.

$$elu(z) = \begin{cases} z & z > 0 \\ \alpha(e^z - 1) & z \leq 0 \end{cases} \quad (4.15)$$

The hyperparameter α controls the value to which an ELU saturates for negative net inputs.

A loss function is required to measure the difference between the neural network predictions and true values. Mean squared error (MSE) is chosen as the loss function considering that the training data are numeric. It measures the expected deviation between the model prediction, $\hat{\mathbf{m}}$ and the true output, \mathbf{m}

$$J = \frac{1}{n} \sum_{i=1}^n (\hat{m}_i - m_i)^2 \quad (4.16)$$

The loss function takes the outputs of the network and the labels to compute a distance score. An optimizer uses this score to adjust the value of the weights in a direction that will lower the loss score.

The back-propagation algorithm is applied to calculate the gradient of the loss function with respect to the weight parameters. Backpropagation works by starting with the final loss value and using the chain rule to work backward from the top layers to the bottom layers, computing the contribution of each parameter to the loss value.

To train a neural network using gradient-based optimization algorithms, the primary objective is to minimize the loss function $J(\theta)$ with respect to the network parameters, θ .

To minimize the loss function, we need to find the direction in which J reduces the fastest. During the training process, the network's parameters are iteratively adjusted to minimize the loss function. This adjustment is performed by computing the gradients of the loss function with respect to the network parameters, which indicate the direction of the steepest descent in the parameter space. Therefore, the derivative of J is taken in the direction of a unit vector \mathbf{u} .

$$\min_{\mathbf{u}} \mathbf{u}^T \nabla_{\theta} J(\theta) \quad (4.17)$$

In fact, J decreases in the direction of a negative gradient. This is known as the steepest descent or gradient descent method. The new point is defined as

$$\hat{\theta} = \theta - \epsilon \nabla_{\theta} J(\theta) \quad (4.18)$$

where ϵ is the learning rate, a positive scalar that determines the size of the step. The learning rate is a hyperparameter that needs to be adjusted during the training.

Optimization techniques that use entire training examples simultaneously to update the parameters are called batch or deterministic gradient methods. These algorithms are computationally expensive. Alternatively, instead of computing the gradient of the loss function for the entire dataset, stochastic optimization computes the gradient for a randomly selected subset of the data, called a mini-batch to update the model parameters.

The mini-batch size is often selected to be small enough to fit into memory while still being sufficiently enough to obtain a reliable approximation of the true gradient. This strategy is computationally efficient and results in a faster convergence than the batch optimization techniques.

There are various versions of stochastic gradient descent (SGD) that vary in how they calculate the next weight update. Instead of only considering the current gradients, these variants also consider previous weight updates (Duchi et al., 2011; Kingma and Ba, 2017).

For example, RMSProp (Root Mean Square Propagation) is an optimization algorithm commonly used in deep learning for training neural networks. It is an extension of the SGD algorithm that adapts the learning rate during training to improve convergence and stability. The steps of the RMSProp algorithm are as follows:

- Initialize the model parameters randomly.
- Initialize an exponentially decaying average of squared gradients.
- Iterate over mini-batches of training samples.
- Compute the gradients of the model parameters.
- Update the moving average of squared gradients using a decay rate.
- Update the model parameters using the computed gradients and the moving average.
- Repeat the above steps until convergence or for a fixed number of iterations (epochs).

RMSProp adapts the learning rate for each parameter based on the moving average of squared gradients, allowing for larger learning rates for parameters with small gradients and smaller learning rates for parameters with large gradients. This helps improve convergence speed and stability during the training of neural networks.

The training process is as follows:

- A batch of training samples and their corresponding labels are drawn from the dataset.
- The weights of the network are initially given random values, also called random initialization.
- The samples are fed into the network to make predictions. The loss of the network is calculated on the batch. The first output of the network is expected to be far from the optimum, and as a result, the loss score is rather high.

- The weights are updated in a way to gradually reduce the loss. Eventually, a model is trained with the minimum loss on training data.

There are two more network patterns that must be considered to train high-performance models that generalize well to new data: data normalization and regularization.

Data normalization is a technique aimed at improving model performance by making the scale of dataset features more comparable to each other. It involves transforming the data in a way that helps the model learn more effectively. One commonly used data normalization technique is batch normalization (Ioffe and Szegedy, 2015). Batch normalization is a layer in the DNN model that can adaptively normalize the data, even as the mean and variance change over time during training. It achieves this by internally maintaining an exponential moving average of the batch-wise mean and variance of the data observed during training. This normalization technique helps stabilize and accelerate the training process by reducing the internal covariate shift (Chollet, 2021).

Another important network pattern for training high-performance models is regularization. Regularization techniques are used to prevent overfitting, which occurs when a model performs well on the training data but fails to generalize to new, unseen data. Any adjustment to a learning algorithm that aims to lower its generalization error but not its training error is known as regularisation. One popular regularization technique is dropout (Srivastava et al., 2014). Dropout randomly sets a fraction of input units to zero during each training step, which helps prevent the model from relying too heavily on any single input feature. This regularization technique encourages the model to learn more robust and generalized representations of the data. The dropout rate, typically set between 0.1 and 0.5, is the percentage of features that are dropped. During the testing phase of a neural network, the dropout technique does not discard any units as it does during training. Instead, to compensate for the fact that more units are typically active during testing compared to training, the output values of the layer are adjusted by scaling them down. This scaling factor is equal to the dropout rate that was used during training.

4.3.1 Model Evaluation

Overfitting is a typical issue in model training that can arise when a model is too complex or has too many parameters in comparison to the quantity of training data that is available. Overfitting can be captured when the model performs well on the training set but poorly on unseen data.

Techniques like regularisation, cross-validation, and early stopping can be employed to reduce overfitting and improve the model to generalize better on unseen data.

To evaluate the model, the dataset is split into three sets: training, validation, and test set. The model is trained on the training data and is tested on the test data. Model hyperparameters including the number of layers, number of nodes, type of activation and optimizer, etc. are not configured by the learning algorithm. The validation set is held out to evaluate the model during training and to configure the hyperparameters.

A common practice to evaluate the model during training is K -fold cross-validation (Bengio and Grandvalet, 2003). Instantiating it involves partitioning the training data into K folds and creating K similar models. Each model is trained on the $K-1$ folds and is evaluated on the remaining partition. The validation score is the average of the K validation scores.

MSE is used as the scoring metric. It incorporates both bias and variance required to compare the model's functionality. Bias and variance measure two different sources of error in a model. Bias measures the expected deviation from the true value of the function or parameter. Variance, on the other hand, provides a measure of the deviation from the expected model value that any particular sampling of the data is likely to cause (Goodfellow et al., 2016). The model with a smaller MSE is our desirable model.

A flowchart containing the main steps taken to complete this research is displayed in Figure 4-2.

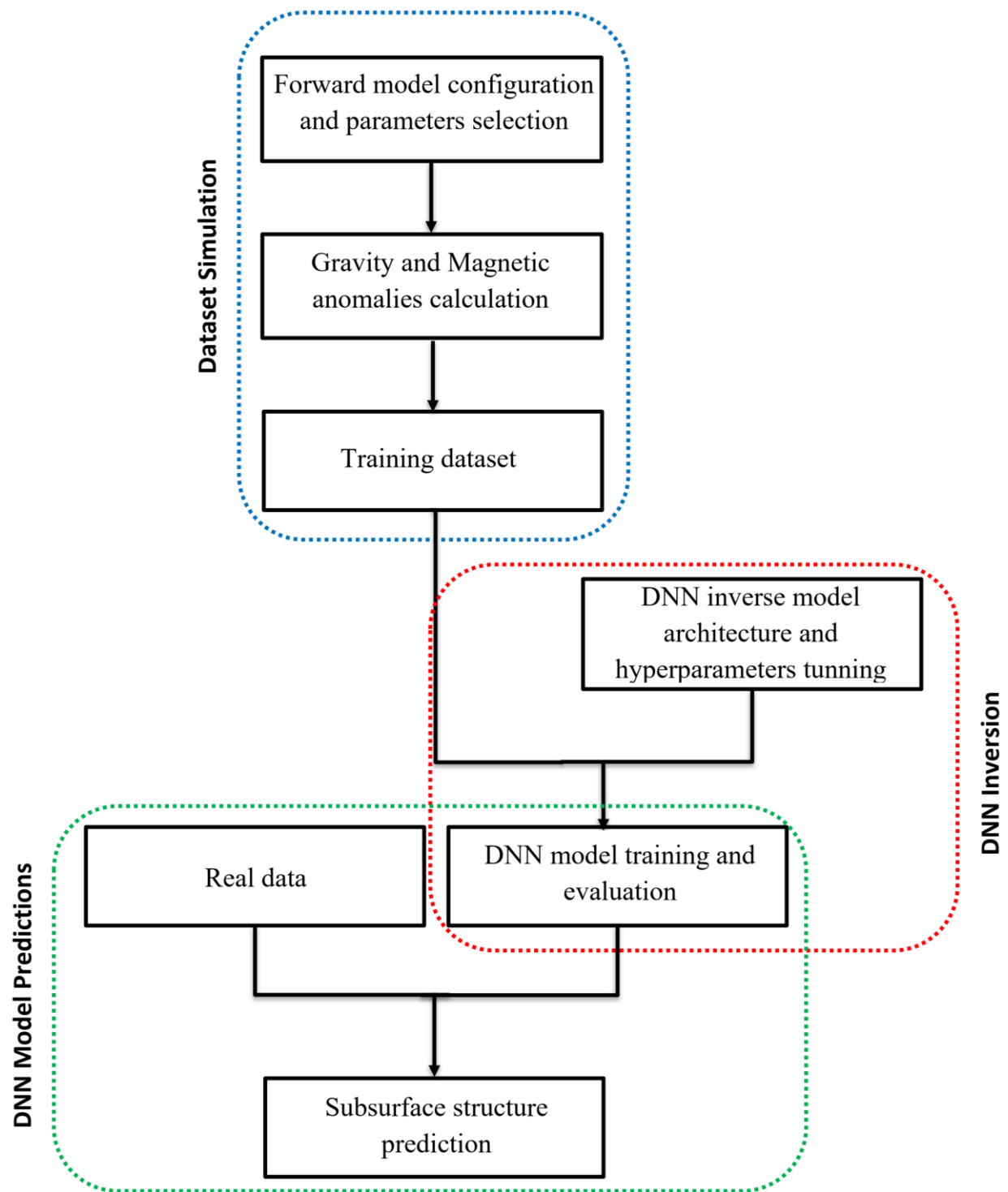


Figure 4-2: The step-by-step research procedure.

Chapter Five: Dataset Simulation for the DNN Inversion

5.1 Introduction

Training datasets, composed of inputs or features and corresponding outputs or labels, are required to optimize the parameters of the ML models. However, in geophysical inversion with ML, a significant challenge arises due to the limited availability of real-world training datasets. To overcome this challenge, the datasets need to be simulated. The dataset simulation in geophysical inversion is the practice of creating synthetic data of subsurface structures that resemble the behavior of the geological features to be studied.

Addressing this issue, a new technique is developed to simulate the training dataset required for the DNN inversion of geopotential data (Ashena et al., 2023). Initially, a forward model is designed that represents the target geological features i.e., crustal structures. The physical parameters of the forward model are assigned based on a priori information. The structure of the forward model is altered to create different configurations of the subsurface model having set some random structural parameters. Subsequently, the geopotential anomalies of the subsurface models are calculated proceeding. Synthetic geopotential data are coupled with subsurface models to create the simulated dataset.

The primary objective of this study is to develop models of the crustal structure, encompassing sediments, salts, and basement. To achieve this, the subsurface is conceptualized as either a two-layer or three-layer structure, depending on the geopotential data used in the inversion.

For the DNN inversion of gravity or magnetic data, a two-layer forward model is adopted (chapter six and chapter seven). This means that the subsurface is divided into two distinct layers: the sedimentary strata and the basement. To further enhance the complexity of the subsurface, the joint inversion of gravity and magnetic data is conducted in chapter eight using a three-layer forward model. The three-layer forward model partitions the subsurface into sediments, salts, and the basement.

The remainder of this chapter concerns the proposed technique for dataset simulation considering the three-layer forward model example.

5.2 Forward Model Simulation

Forward modeling is the process of simulating the subsurface geological structures and estimating their synthetic geophysical anomalies over the observation points. Since this research seeks to investigate hydrocarbon reservoir structures, a 2.5D forward model is created that partitions the upper crust into three (or two) layers, as sediments, salts, and basement (Figure 5-1). Each layer is discretized into an assembly of m rectangular prisms isolated from their surrounding geological environment. The physical parameters including density and susceptibility of the layers, are incorporated into the model as a priori information. The priori information is acquired from geophysical and geological studies, well logs, and the tectonic setting of the region.

The total length of the model and each prism are specified based on the dimensions and resolutions of the anomalies being investigated. In the context of geophysical modeling, a 2.5D model refers to a simplified representation of a 3D subsurface structure. It assumes that the subsurface varies in two dimensions (along the X direction (or length of the model) and depth) but remains constant in the third dimension (Y direction (or width of the model)). This simplification allows for computational efficiency while still capturing important variations in the subsurface.

When it is mentioned that the width of the 2.5D model is going to infinity, it implies that the extent of the subsurface in the Y direction is considered infinitely large. In other words, the model assumes that the subsurface variations are consistent in the Y direction. This assumption is often made to simplify calculations and avoid dealing with complexities arising from lateral variations or boundaries. A width of 20 times a prism's length is used to mathematically satisfy the infinite width of the 2.5D model. The model is then extended at both lateral sides to avoid potential edge effects. The edge effect arises due to the incomplete coverage of the subsurface model or gravity data leading to inaccuracies in observed anomalies near the edges of the model. To avoid the edge effect one method is to add padding around the edges of the available gravity data. This involves extending the study area by including additional cells surrounding the existing data points.

The adopted dimensions of the forward model cannot be modified during the dataset simulation and remain fixed.

To create numerous representations of the forward model structure, the topography of the salts and basement layer randomly changes. To this end, several random structural parameters are defined that select their values from predefined ranges.

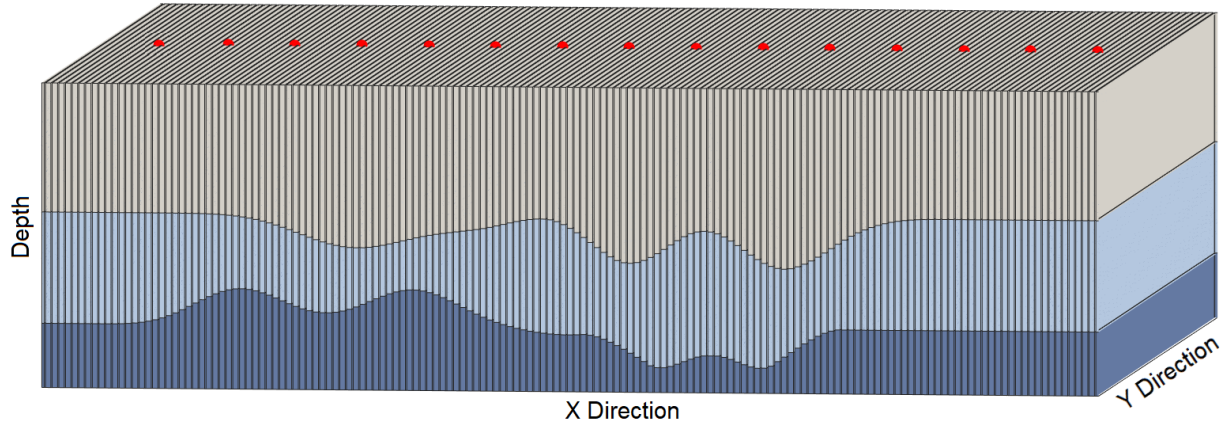


Figure 5-1: Schematic view of the 2.5D forward model and observation points (red dots) on the surface.

The following bullet points discuss examples of the random parameters briefly:

- The average depths of the salts and basement layers
- The number of anomalies to be loaded on top of the salts and basement layers
- The origin coordinate of the anomalies
- The heights of the anomalies (topography variations)
- The lengths of the anomalies

Given the number of training data, by assignation from the list of the parameters, a different forward model is generated in each iteration, and its synthetic gravity and magnetic anomalies are calculated correspondingly.

First, in each iteration, two average depths are randomly selected from the corresponding range parameter and assigned to salts and basement layers. To prevent the salt and basement layers to overlap, a tolerance of 200 *m* is imposed as the required minimum gap between these two layers. To change the topography of the layers, my strategy is to create some random anomalies with different lengths and heights and have them loaded on top of the prisms. The Gaussian function is used to generate anomalies with zero mean and standard deviation equal to the lengths of the anomalies.

The number of anomalies and their corresponding lengths and heights are randomly selected from the number of anomalies, length of anomalies, and height of anomalies ranges. Moreover,

the center location of each anomaly is also randomly chosen from a range equal to the number of prisms. Having the width, random length l_a , height h_a , and center location $(x_j, 0)$, the Gaussian function is used to create each anomaly with zero mean and standard deviation equal to half of the random length,

$$f(x, y) = h_a e^{-\left(\frac{(x-x_j)^2}{2(l_a/2)^2} + \frac{y^2}{2(w_a/2)^2}\right)} \quad (5.1)$$

The choice of the Gaussian function for creating random anomalies depends on the specific characteristics and objectives of the study. The Gaussian function is a smooth and bell-shaped curve. This smoothness can be advantageous in certain cases where we want to generate anomalies with gradual variations or subtle changes in amplitude. Since we are interested in creating anomalies that smoothly blend with the surrounding geology or have gradual variations in their intensity, then the Gaussian function can be a suitable choice. Moreover, the Gaussian function allows us to control the length or standard deviation of the anomalies, which influences their shape and spatial extent. This flexibility can be beneficial if you want to simulate anomalies of varying sizes and shapes in your forward model. It should be noted that depending on the specific context and characteristics of the study, alternative functions or distributions can be considered for generating anomalies. For example, sharp or abrupt changes in the anomalies are expected, and other non-Gaussian distributions can be explored that better represent such features.

To illustrate how the topography of the layers changes, a visual representation is provided in Figure 5-2. This is an example of a two-layer model which can be expanded to the three-layer case. Here, the algorithm randomly selected six anomalies to be created, each generated from a Gaussian function with random heights and depths. These anomalies were then added to the lower layer with an initial constant average depth. Due to the random placement, anomalies may overlap and produce different shapes, as seen in the bottom panel of Figure 5-2.

With the random selection of structural properties, a diverse range of synthetic datasets are generated that closely mimic the complexities of real-world subsurface structures. This demonstrates the versatility of our dataset simulation approach.

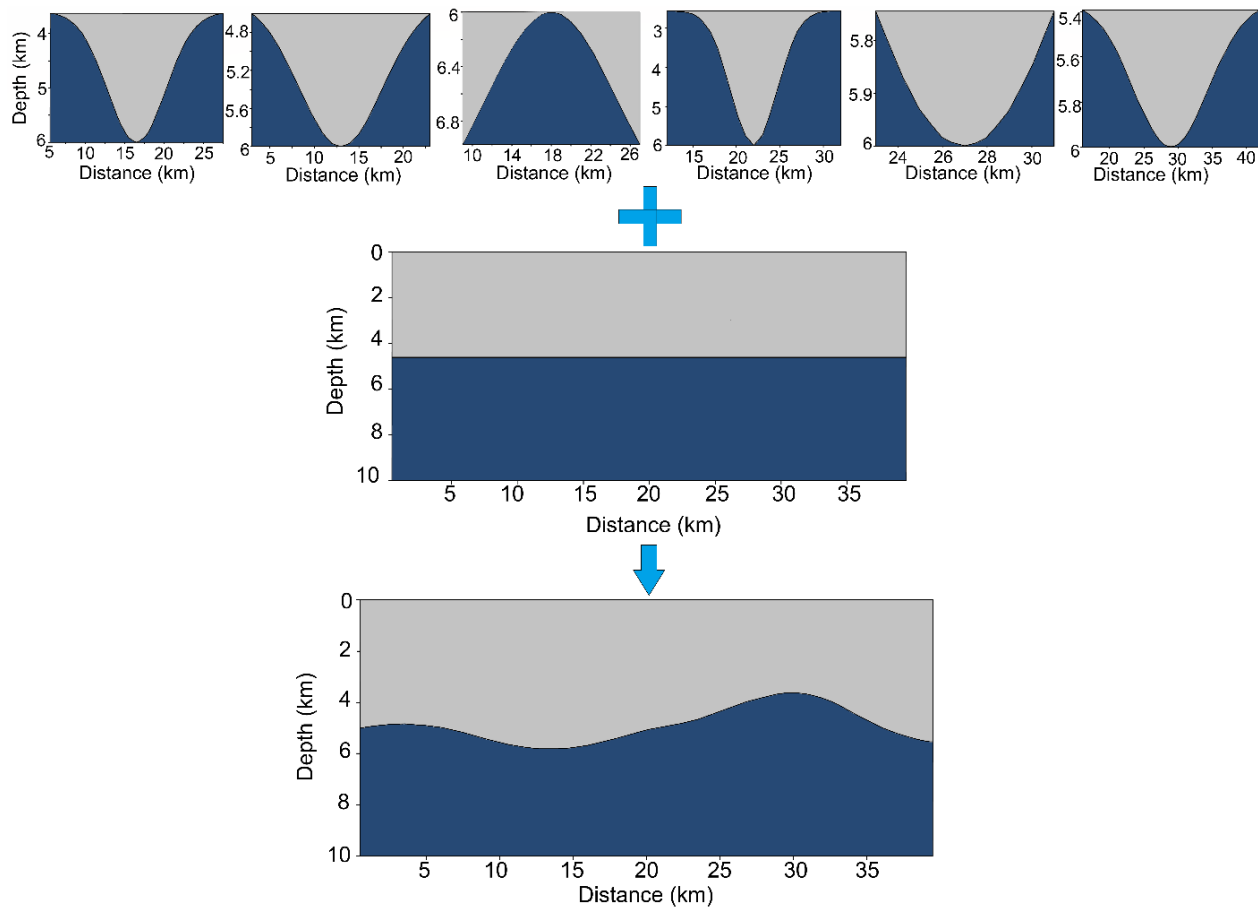


Figure 5-2: An example of synthetic forward model simulation.

5.3 Geopotential Anomalies Calculation

Once the forward models are simulated their gravity and magnetic effects are calculated over the observation profile, with the center of the profile set as the origin coordinate of the model.

5.3.1 Gravity Anomaly

Gravity field variations arise from heterogeneous mass distribution in Earth's crust and upper mantle and are measured using sensitive gravimeters over the observation stations on the Earth's surface. The gross variation of gravity on Earth quite closely corresponds to what is expected from an idealized Earth with no lateral variations of structure and density, which would occur if a fluid accommodated perfectly to the forces arising from self-gravitation and rotation. Such an Earth is referred to as the "normal Earth". Gravity anomaly results from the deviation of the observed gravity from an expected normal field.

To calculate gravity anomalies, the forward modeling approach is employed, which involves simulating the gravity effects of the subsurface structures. The forward model consists of three layers, each representing a distinct geological unit, such as sediments, salts, or basement. Each layer is created from an assembly of rectangular prisms.

To calculate the gravity anomaly of the forward model, the density contrast between the layers and a reference is considered. The gravitational anomaly of each prism is calculated using the principle of superposition, where the contributions from all prisms are summed to obtain the total gravity anomaly. The gravity attraction of each cell j ($j = 1, \dots, m$), at each observation point i ($i = 1, 2, \dots, n$), considering a constant density ρ_j is given by (Chakravarthi and Sundararajan 2007).

$$g_{ij} = -\gamma \rho_j \sum_{p=1}^2 \sum_{q=1}^2 \sum_{s=1}^2 \mu_{pqs} \times \left[a_p \ln(b_q + \mu_{pqs}) + b_q \ln(a_p + \mu_{pqs}) - c_s \arctan\left(\frac{a_p b_q}{c_s r_{pqs}}\right) \right]$$

where,

$$\mu_{pqs} = (-1)^p (-1)^q (-1)^s, \quad p, q, s = 1, 2$$

$$a_p = x_i - x'_{pj}, b_q = y_i - y'_{qj}, c_s = z_i - z'_{sj} \quad (5.2)$$

and $(x'_{pj}, y'_{qj}, z'_{sj})$ are the coordinates of the eight corners of the j th prism. The distance between a corner of the prism and the observation point is given by $r_{pqs} = (a_p^2 + b_q^2 + c_s^2)^{1/2}$.

5.3.2 Magnetic Anomaly

Whereas the gravity field of the earth is largely time-invariant, except for relatively minor or long-term changes due to redistribution of mass, the geomagnetic field varies in both direction and intensity over time scales ranging from milliseconds to millennia (Blakely, 1995).

The geomagnetic field is composed of both internal and external sources. External sources refer to the factors outside the Earth that influence the geomagnetic field. The most significant external source is the solar wind, which is a stream of charged particles that flows out from the Sun. When the solar wind encounters the Earth's magnetic field, it can cause disturbances that affect the field.

Internal sources refer to the processes that occur within the Earth's core, which generate the main component of the geomagnetic field. The motion of molten iron in the Earth's outer core

generates electrical currents, which in turn create the magnetic field. The high-order terms in the energy density spectrum of the geomagnetic field are related to the magnetization of crustal rocks. Magnetic investigations can therefore yield important data about geological structures. By analogy with gravity anomalies, we define a magnetic anomaly as the difference between the measured (and suitably corrected) magnetic field of the Earth and that which would be expected from the IGRF (Campbell, 2001; Lowrie and Fichtner, 2020).

The Earth's magnetic field intensity is expressed in units of nanotesla (nT). The geomagnetic elements are taken to be components parallel to the geographic north and east directions and the vertically downward direction (Figure 5-3).

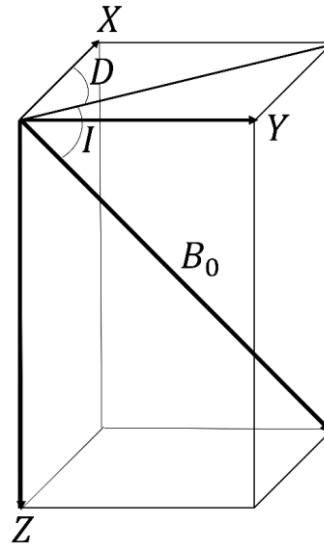


Figure 5-3: Geomagnetic field components.

The magnitude of the magnetic vector is given by the field strength B_0 ; its direction is specified by two angles. The declination D is the angle between the magnetic meridian and the geographic meridian; the inclination I is the angle at which the magnetic vector dips below the horizontal. The Cartesian (X, Y, Z) and spherical polar (B_0, D, I) sets of geomagnetic elements are related to each other as follows,

$$\begin{aligned}
 B_0^2 &= X^2 + Y^2 + Z^2 \\
 X &= B_0 \cos(I) \cos(D), Y = B_0 \cos(I) \sin(D), Z = B_0 \sin(I), \\
 D &= \arctan\left(\frac{Y}{X}\right), I = \arctan\left(\frac{Z}{\sqrt{X^2 + Y^2}}\right)
 \end{aligned} \tag{5.3}$$

The magnetic anomaly results from the contrast in magnetization of rocks with different magnetic properties adjacent to each other.

The combination of the anomalous magnetic field (T) and the earth's main field (B_0) is the quantity measured by the airborne magnetometers (B). The main magnetic field that originates from the core of the earth and contains the long wavelength of the total magnetic field can be obtained from global models such as the IGRF. After subtraction of the main field from the observed data, the residual magnetic field is transformed into DRTP anomalies map. The DRTP corrects for regional variations in inclination and declination on the assumption that all magnetization is induced. In fact, the anomalous component of the observed magnetic field originates from crustal magnetized rocks that are composed of both remnant magnetization and induced magnetization. The induced magnetization is defined by

$$M_I = \frac{B\chi}{\mu_0(1+\chi)} \quad (5.4)$$

where $\mu_0 = 4\pi \times 10^{-7} \text{ H/m}$ is vacuum magnetic permeability, and χ is the susceptibility that denotes how much a material will become magnetized in an applied magnetic field. It is often difficult to distinguish remnant magnetization from induced magnetization, and therefore in this study, it is assumed that the basement only has induced magnetization.

Considering the same prismatic model, the total magnetic field anomaly T of a rectangular prism at origin represents as (Blakely, 1996)

$$T = EI \times C_m [l \quad m \quad n] \times \begin{bmatrix} -\tan^{-1}\left(\frac{yz}{xr}\right) & \ln(r+z) & \ln(r+y) \\ \ln(r+z) & -\tan^{-1}\left(\frac{xz}{yr}\right) & \ln(r+x) \\ \ln(r+y) & \ln(r+x) & -\tan^{-1}\left(\frac{xy}{zr}\right) \end{bmatrix} \begin{bmatrix} \Delta x_2 \\ \Delta y_2 \\ \Delta z_2 \end{bmatrix} \begin{bmatrix} \Delta x_1 \\ \Delta y_1 \\ \Delta z_1 \end{bmatrix} \times \begin{bmatrix} L \\ M \\ N \end{bmatrix} \quad (5.5)$$

where, $\Delta x_p = x_i - x'_j$, $\Delta y_p = y_i - y'_j$, $\Delta z_p = z_i - z'_j$ and r is the distance between the measurement station at (x_i, y_i, z_i) and prism at (x'_j, y'_j, z'_j) ; l, m, n are directive cosines of the geomagnetic field at the station; and L, M, N are directive cosines of the geomagnetic field at each prism. Moreover, $C_l = 1$ is a dimensionless magnetic constant in electromagnetic units.

5.4 Conclusion

In this chapter, an original approach for the dataset simulation was provided. The developed technique presents a flexible and adaptable solution for simulating large volumes of data required for specific DNN inversion tasks. In the following chapters (chapter six to chapter eight), the proposed technique is exploited for the simulation of diverse datasets tailored to inversion of gravity data, inversion of magnetic data, and joint inversion of gravity and magnetic data offshore UAE.

Chapter Six: DNN Inversion of Gravity Data

6.1 Introduction

Interpretation of the gravity field holds a significant place in comprehending the Earth's subsurface. The Earth's mass distribution and shape are governed by the central force of gravity, which is counteracted mainly by the molecular and atomic forces that resist compression and deformation. Thermal perturbations of the equilibrium, which gravity strives to achieve, maintain, or restore, are the main generators of ongoing geodynamic processes. These processes create density distributions that generate observable gravity signals, which serve as the focus of gravity studies. Geological structures resulting from previous geodynamic processes are preserved over extended periods near the Earth's surface in the crust.

Gravity interpretation refers to the interpretation of gravity anomalies. Gravity anomalies are continuous variations in space while gravity values are observed over discrete points on the Earth. Defining an anomaly from discrete observations is part of gravity interpretation.

Inversion of gravity anomalies is the mathematical derivation of geometrical or density parameter distributions of the subsurface. However, gravity inversion is a notoriously non-unique problem, while the forward problem of determining the gravity effects of given mass distributions is unique. It means that there are always infinite solutions that fit the data equally well. The ambiguity arises from the trade-off between the depth of the anomalous mass and its density distribution.

The infinity of solutions can be reduced by invoking a priori information which is mandatory for gravity inversion. The a priori information can be obtained from different sources such as geological and geophysical data. Moreover, essential knowledge of gravity data and density distribution is required for reducing this ambiguity. However, the additional knowledge may be limited. If the a priori information were complete, there would be no problem left to be solved.

Gravity inversion is an important geophysics tool that provides insights into the subsurface structure and composition such as hydrocarbon reserves and the Earth's crust. Different gravity inversion approaches with varying complexity and accuracy are developed based on the applied method, the usage of prior information and constraints, and the geological feature to be

investigated (B. Ashena et al., 2018; Bear et al., 1995; Boulanger and Chouteau, 2001; Camacho et al., 2002; Cella and Fedi, 2012; Last and Kubik, 1983; Li and Oldenburg, 1998).

Gravity inversion using DNN is a relatively new approach to the interpretation of gravity data (Ashena et al., 2022; Li et al., 2022; Yang et al., 2022; Huang et al., 2021; Zhang et al., 2019; Yang and Ma, 2019). DNN inversion is capable to map nonlinear and complex relationships between large amounts of gravity data and the subsurface model. DNN gravity inversion involves training a neural network on a set of simulated or real gravity data and corresponding subsurface models. The trained DNN model can then be used to invert unseen gravity data to obtain a subsurface model that explains the observed data.

The remainder of this chapter discusses our intelligent inversion software developed for modeling basement topography. First, our technique for simulations of training datasets is explained, including forward model creation, parameter selection, and gravity data calculations. Following this, the DNN inversion model is trained using the simulated dataset for basement topography estimation in the offshore UAE. The DNN model architecture, training procedure, and hyperparameters fine-tuning are described in detail. The performance of the trained model is then evaluated with unseen noise-free and noise-added synthetic data. Eventually, the model is run to estimate the basement topography from pseudo-gravity data over the Ghasha hydrocarbon reservoir in the offshore UAE.

6.2 Gravity Dataset Simulation

A 2.5D forward model of the target area partitioned the subsurface into two layers (Figure 6-1). The upper layer constitutes the sedimentary strata, volcanic rocks and the Hormoz evaporates. The lower layer is assigned to the Proterozoic basement. The 86 km length of the profiles is set as the length of the forward model. The model is then extended at both lateral sides by half the length of the biggest random anomaly (20 km) to avoid potential edge effects. The basement of the UAE is overlain by a thick sequence of sedimentary strata and thus cannot be reached by exploration wells and seismic exploration. However, the crystalline basement of the UAE is exposed in the Arabian Shield and Dhofar region of Oman (Mercolli et al., 2006; Nehlig et al., 2002). The basement exposures are composed of high-grade metamorphic and igneous rocks (Allen, 2007; Bowring et al., 2007). Based on this information, the density of 2800 kg.m^{-3} is considered for the Proterozoic basement. Assuming the density of 2600 kg.m^{-3} for the

background, the density contrast of the basement against that of the background would be 200 kg.m^{-3} . We set the density contrast of the sediments to zero to disregard its mass changes from the simulated gravity anomaly. Consequently, the gravity anomaly solely reflects the effects of the basement.

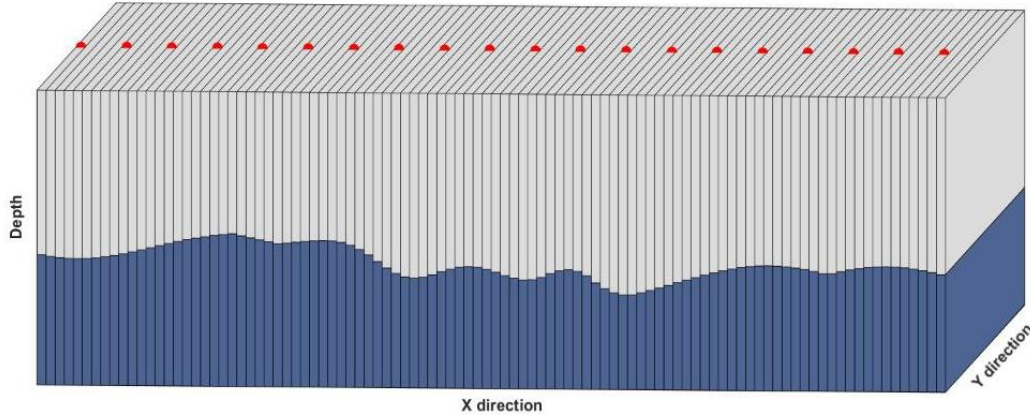


Figure 6-1: Schematic view of 2.5D forward model and observation points (red dots) on the surface.

The basement is simulated from an assembly of rectangular prisms each 1 km long and 20 km wide. The lower boundary of the lower layer is fixed at 12 km. The heights of the prisms are adjusted during the dataset creation process by adopting random parameters. The ranges of random parameters are provided in Table 6-1. The average depth and topography parameters are set to 5 km to 9 km and 3 km to 11 km respectively. Moreover, we chose the number of the anomalies and length of the anomalies to be 1 to 8 anomalies and 8 km to 40 km respectively.

Applying these parameters, a dataset has been simulated of 200,000 instances with gravity anomaly as inputs and basement topography as labels. Dataset creation was completed in 19 minutes using the multiprocessing library to accelerate the process on a PC with Intel Core-i7CPU 3GHz and 16.0 GB RAM.

Table 6-1: Random parameter ranges of the forward models.

The lower layer (Basement)	
Average depth (km)	5-9
Topography range(km)	3-11
Length of anomalies (km)	8-40
Number of anomalies	1-8

Figure 6-2 shows some samples of the simulated gravity dataset including their simulated forward models together with their calculated gravity anomalies.

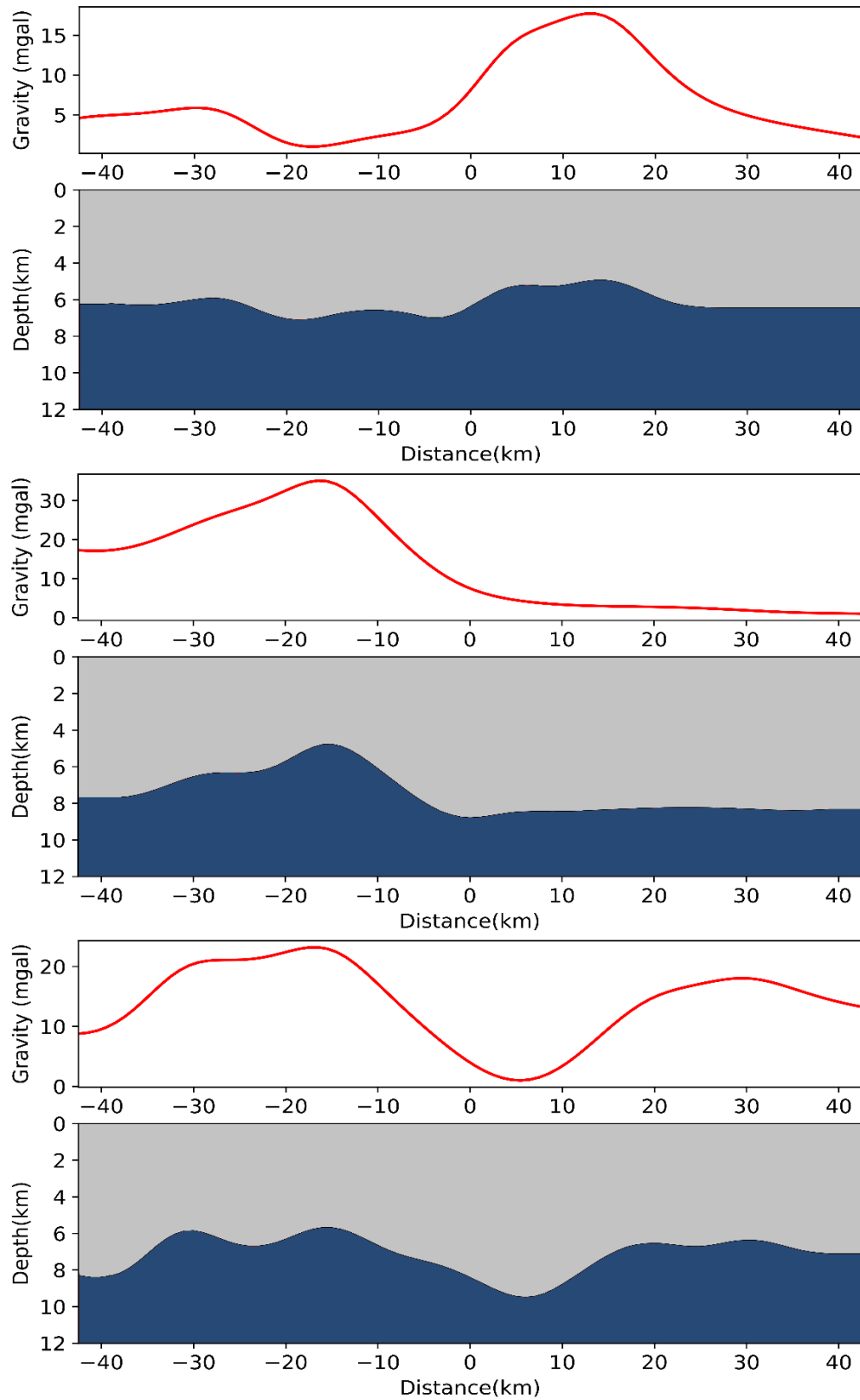


Figure 6-2: Samples of a simulated dataset. The red curve represents the synthetic gravity in mGal. The subsurface model is depicted with gray and dark blue colors, corresponding to sediments, and basement layers, respectively.

6.3 DNN Gravity Inversion

Using the simulated dataset, a DNN model is trained to conduct the nonlinear inversion of gravity data. Finding the optimal hyperparameters is a tedious task if conducted through a trial-and-error approach. The grid search algorithm is applied using the validation set to optimize the hyperparameters. The grid search algorithm is a hyperparameter optimization technique used in ML to find the best combination of hyperparameters for a given model. Hyperparameters are parameters that are not learned from the data but are set before training the model. The grid search algorithm works by creating a grid of all possible hyperparameter values and then evaluating the model's performance using cross-validation for each combination of values. Accordingly, the optimal DNN model consisted of three hidden layers, each with 300 neurons. Glorot Normal and Elu were the weight initializer and the activation function of the model. The RMSprop technique is chosen to optimize the model parameters. The initial learning rate obtained from the grid search was 0.0003. To avoid overfitting in the DNN model training, the dropout regularization technique is used with a dropout rate of 0.1. In other words, 10 percent of the neurons are randomly selected and removed during each update.

The DNN model was trained using the TensorFlow library with a batch size of 32 and 30 epochs and conducted on an NVIDIA GeForce GTX 1660 Ti GPU.

The training workflow is as follows. A DNN model is built and trained using the Keras library, a high-level API of TensorFlow developed by Google. A model is defined using the Sequential class. For the DNN model to be trained, a set of hyperparameters need to be configured, including: the number of hidden layers and the units in each layer; an initializer to start the random weights of the layers; an activation function for the hidden layers through which the sum of weighted inputs is passed; an optimizer and its parameters including the learning rate, through which the model is updated; a regularization technique to avoid overfitting the model; and a loss function to measure the difference between the network outputs and the actual labels.

Random Search technique from Scikit-learn is applied (Pedregosa et al., 2011), which samples combinations of the parameters from a specified parameter space. The parameter space includes: the options for the number of hidden layers, [2,3,5]; the number of units in each layer, [100, 200, 300,400]; and the hidden layers activation function, ['elu', 'tanh'].

The DNN model is fed with the simulated dataset to learn a function that maps the input features to the output values with the lowest possible error. The simulated dataset contains

examples of gravity anomalies with their corresponding basement topography as labels. Since the basement depths are continuous numerical values, the problem turns out to be a DNN regression task. Correspondingly, no activation function is applied to the last layer. Furthermore, MSE is used as the loss function which calculates the square of the difference between the predictions and the targets.

6.3.1 Error Analysis

Regarding model evaluation, the dataset is split into training (%90) and test (%10) sets. The model is trained using the training set and evaluated on a hold-out validation dataset after each epoch. The resulting learning curve is plotted for training and validation MSE versus epochs (Figure 6-3). As can be noticed, both training and validation MSE decrease as the number of epochs increases to a point of stability with a minimal gap between them. This means that the model is performing well on the training data and generalizing well to new data. To evaluate the performance of the trained DNN model prediction, MSE is also employed on the test set. The evaluation scores show a test loss of 0.08 km^2 .

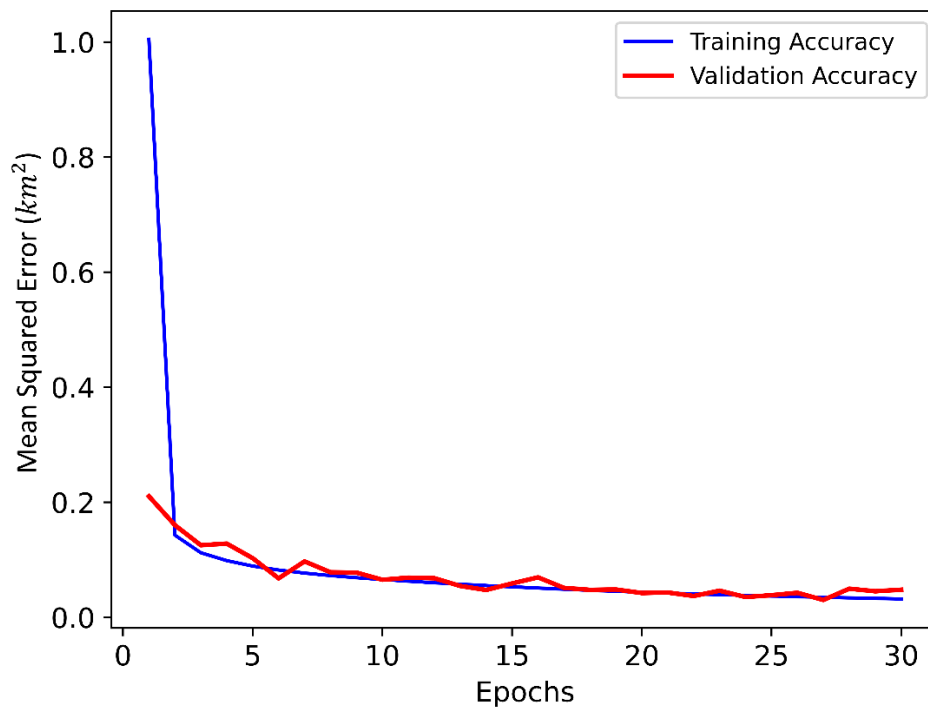


Figure 6-3: Plot of Training versus and validation accuracy against epochs.

6.4 DNN Gravity Model Evaluation

The model performance is tested using unseen synthetic gravity data to predict the basement topography. Following, the MSE value between the true and predicted basement depths is calculated. Figure 6-4 illustrates some examples of basement topography predictions against the actual synthetic data. The average MSE value comes to 0.07 km^2 . As illustrated, the predicted basement topography correlates with the true simulation (white dashed line) including the average depth of the basement and the shape and location of the basement anomalies.

Additionally, the model's performance against noise was tested on gravity data with added Gaussian noise values of 5% and 10%. The average MSE values were obtained to be 0.14 km^2 and 0.17 km^2 respectively. The results of model predictions on the noise-added gravity data are illustrated in Figure 6-5 and Figure 6-6 respectively. This demonstrates that our DNN inversion model has satisfactory robustness against noise-contaminated data and can estimate the basement topography with desirable accuracy.

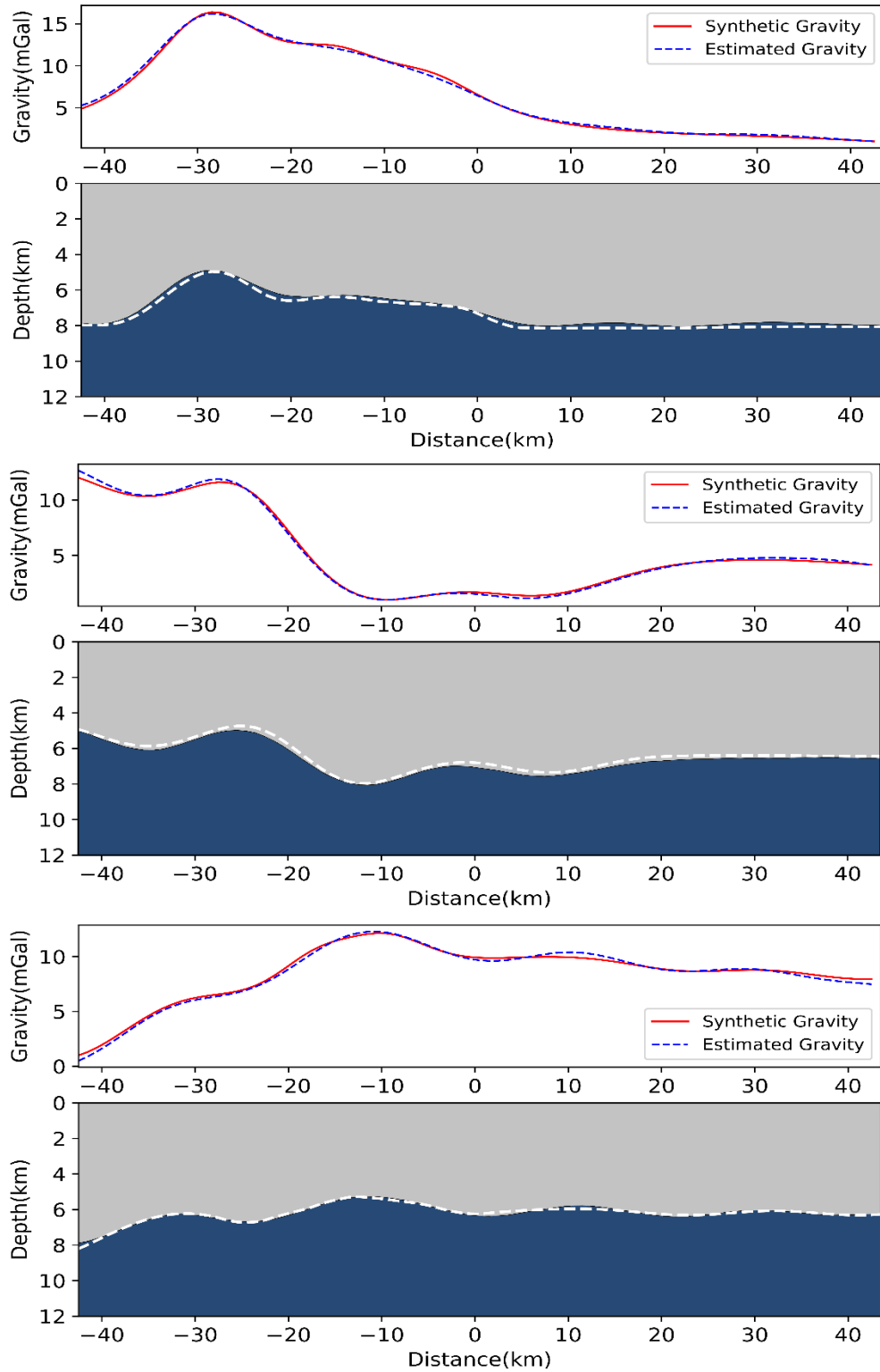


Figure 6-4: Samples of DNN gravity model prediction results. The red curve represents the synthetic gravity fed into the DNN model. The dashed blue curve represents the estimated gravity of the predicted subsurface structure. The predicted subsurface structure is depicted with gray, and dark blue colors, corresponding to sediments, and basement layers, respectively. The white dashed curve represents the actual basement topography.

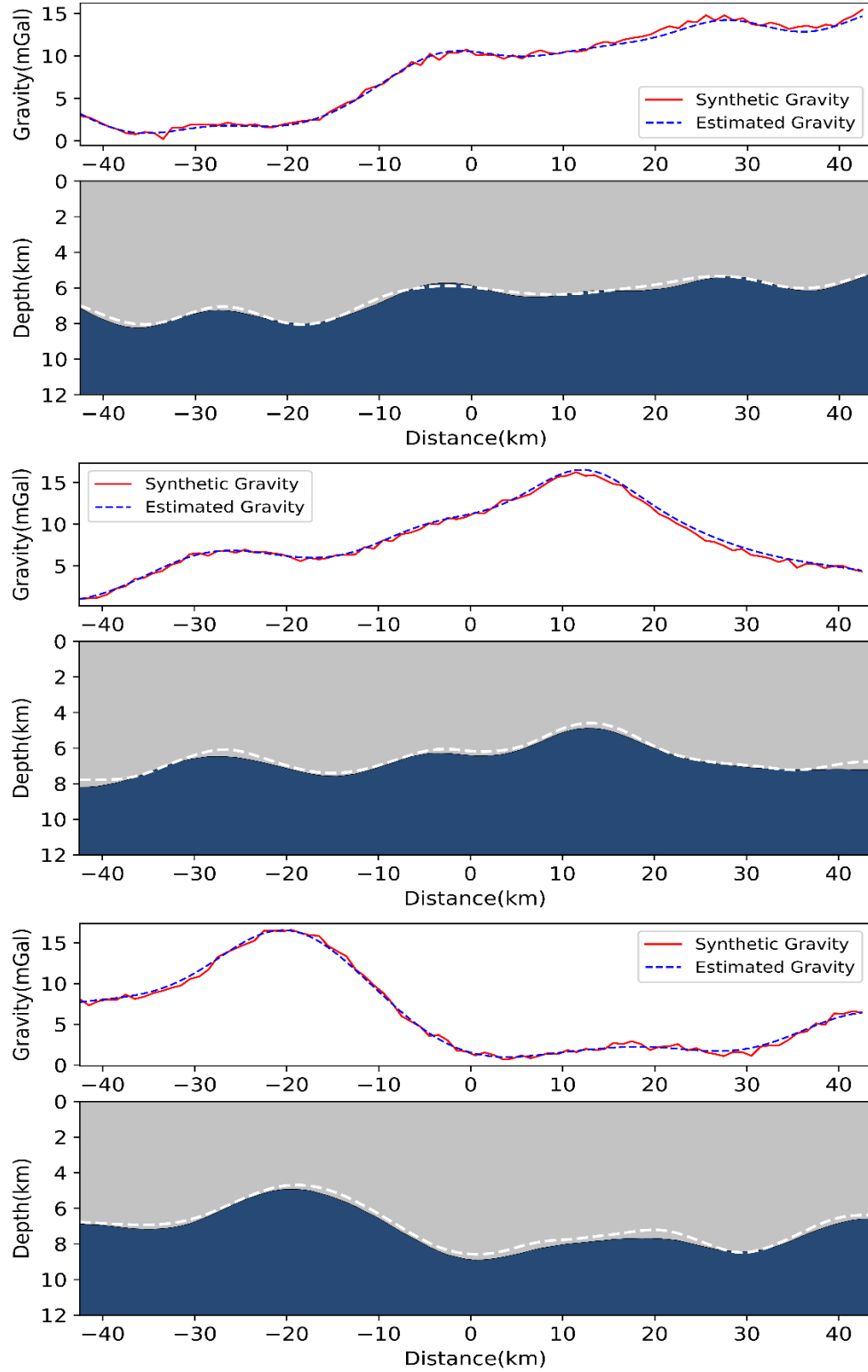


Figure 6-5: Samples of DNN model prediction results. The red curve represents the 5% Gaussian noise-added synthetic gravity anomaly fed into the DNN model. The dashed blue curve represents the estimated gravity anomaly of the predicted subsurface structure. The predicted subsurface structure is depicted with gray, and dark blue colors, corresponding to sediments, and basement layers, respectively. The white dashed curves represent true basement topography.

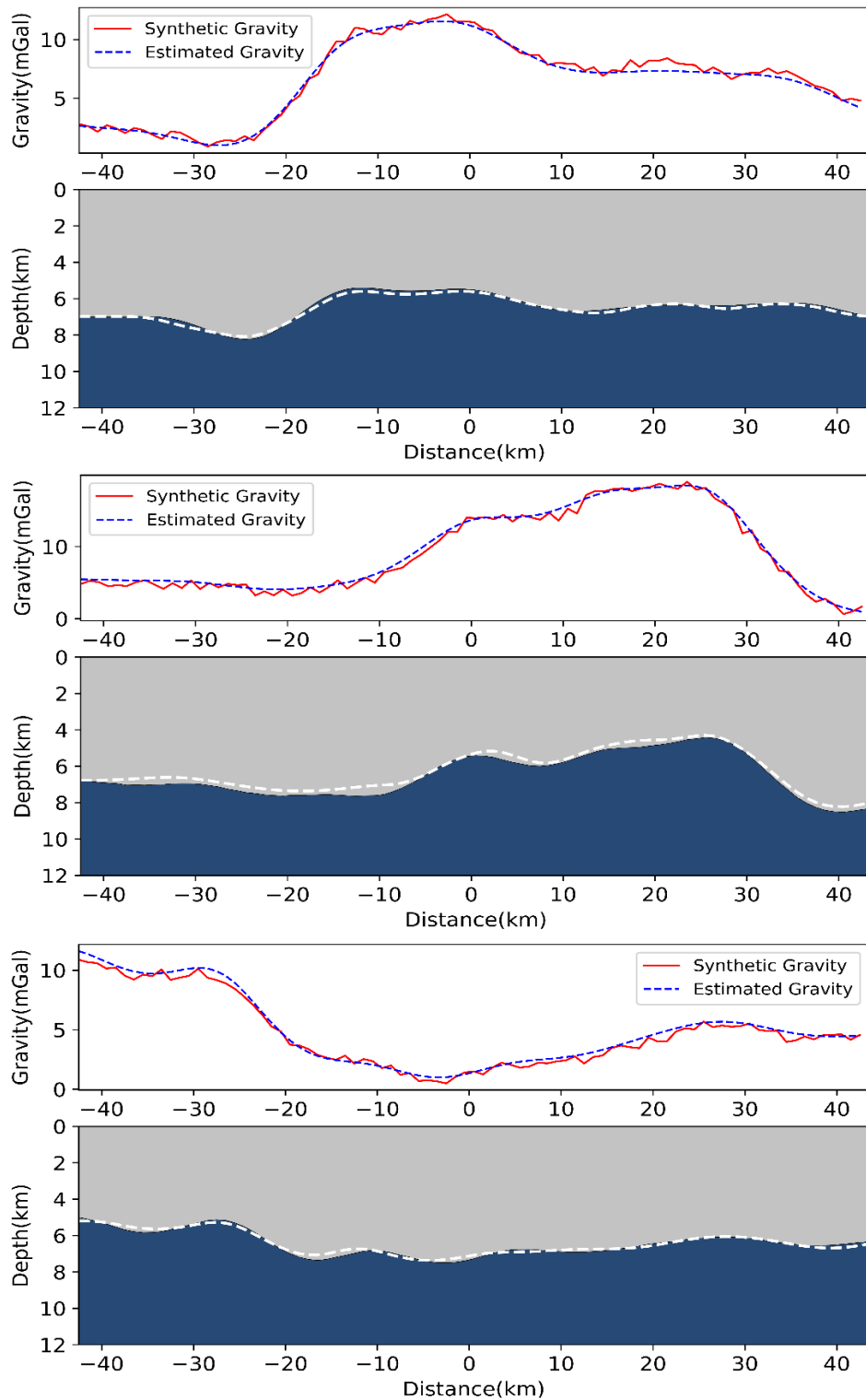


Figure 6-6: Samples of DNN model prediction results. The red curve represents the 10% Gaussian noise-added synthetic gravity anomaly fed into the DNN model. The dashed blue curve represents the estimated gravity anomaly of the predicted subsurface structure. The predicted subsurface structure is depicted with gray, and dark blue colors, corresponding to sediments, and basement layers, respectively. The white dashed curves represent true basement topography.

6.5 Results and Discussion

Determining basement structure is essential for the exploration of hydrocarbon reservoirs (Hodgson, 1965). Basement structures play an important role in the trapping mechanisms of hydrocarbon reservoirs as they propagate into the overlying sedimentary rocks and influence the fluid flow and the distribution of hydrocarbon traps (Palumbo et al., 2002). Moreover, tectonic processes that form basement structures also influence source rock distribution, heat flow, trap timing, and sediment supply. Therefore, a better understanding of basement structures eventually provides us with prospects to locate the optimal sites for hydrocarbon exploration wells.

The gravity anomaly of the basement is required to model the basement topography of the target region using our DNN model. The complete Bouguer gravity anomaly (Figure 2-2a) encompasses the gravity effects of the sediments, salt bodies, the basement, etc. To obtain the gravity anomaly of the basement, the portion of the gravity anomaly caused by mass changes above the basement needs to be removed from the total Bouguer gravity anomaly. Obscured by the negative gravity of the salt bodies, it is not feasible to distinguish the positive gravity effect of the basement from the anomaly of the sedimentary layers. Our alternative solution to this problem is to use pseudo-gravity anomalies instead of gravity anomalies. The pseudo-gravity anomaly is obtained from the converted magnetic anomaly. Disregarding the insignificant magnetic effects of sedimentary formations and igneous rock bodies, the magnetic anomaly originates mainly from the Proterozoic basement.

The Poisson theorem constructs the basis of the pseudo-gravity transform by linearly connecting the magnetic potential to the gravity potential under a few assumptions. This theorem requires that causative density and magnetic sources be common and that magnetization direction and magnetization-to-density ratio be constant. The pseudo-gravity transform is defined in the Fourier domain (Blakely, 1995).

$$\begin{aligned} F[g^{psg}] &= \frac{\gamma}{C_m |k| \theta_f \theta_m} \frac{\rho}{M_I} F[T] \\ \theta_f &= \hat{f}_z + i \frac{\hat{f}_x k_x + \hat{f}_y k_y}{|k|}, \\ \theta_m &= \hat{m}_z + i \frac{\hat{m}_x k_x + \hat{m}_y k_y}{|k|} \end{aligned} \quad (6.1)$$

In these equations, g^{psg} is the pseudo-gravity transform of magnetic anomaly field T , k is the wavenumber, and \hat{f} and \hat{m} are the unit vectors parallel to the magnetization and ambient field,

respectively. In addition, $C_m = 1$ denotes the dimensionless magnetic constant in electromagnetic units, whereas its value is considered $C_m = 10^{-7} H/m$ in the international system of units (SI), γ represents the gravitational constant, ρ is the density, and M_I is the induced magnetization in the direction of the geomagnetic field. $\frac{\rho}{M_I}$ defines the density-to-magnetization ratio.

The pseudo-gravity anomaly map over the largest hydrocarbon reservoir of the region Ghasha has been obtained and displayed in Figure 6-7.

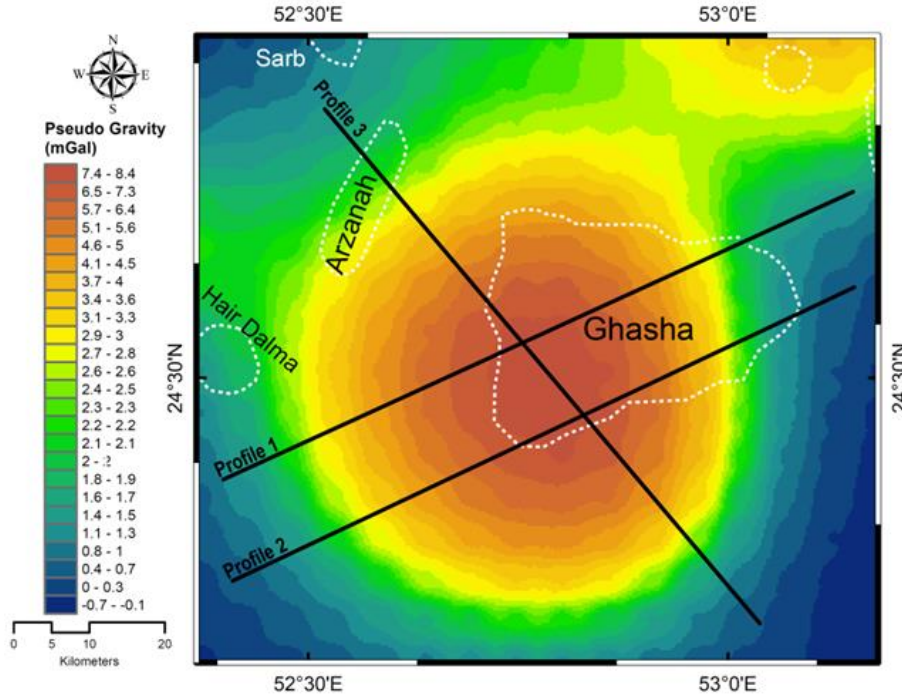


Figure 6-7: Location of the profiles over pseudo-gravity anomalies map of the study area together with its hydrocarbon reservoir (oil-water) boundaries.

We applied the trained DNN inverse model to estimate the basement topography in offshore UAE across three profiles extracted from the pseudo-gravity map of the region (Figure 6-7). Profile 1 and Profile 2 cross the largest hydrocarbon field of the region (Ghasha) along the SW-NE direction and Profile 3 bisects the first two profiles and crosses the Ghasha reservoir from NW to SE. The results of our basement topography predictions are shown in Figure 6-8 through Figure 6-11. They demonstrate a satisfactory fit between the observed and predicted gravity data. The basement topography range is obtained between 7.4 km to 9.3 km with the shallowest part located below the Ghasha oil field reservoir. Our results also show that the deepest part of the basement appears toward the east of the profile.

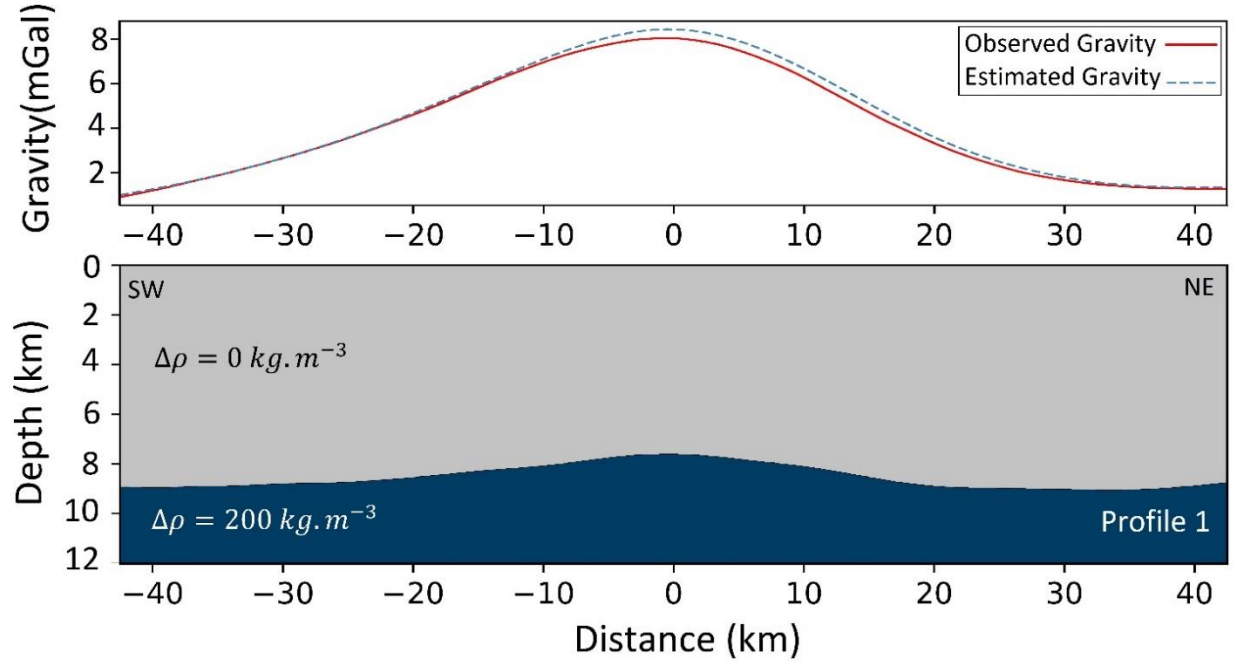


Figure 6-8: Result of the DNN inverse model prediction across profile 1. The predicted subsurface structure is depicted with gray, and dark blue colors, corresponding to sediments, and basement layers, respectively.

The structural parameters including the average depth of the basement and the length and height of the anomalies that change the topography of the basement during database simulation are chosen from ranges of values. The DNN model was also trained using these values and predicted the topography within these ranges. The geological and geophysical studies conducted in the region can provide us with an initial estimate of the parameter ranges. Previous studies in UAE suggest a thick sedimentary layer between ~ 5 to ~ 10 km (Geng et al., 2022; Ghalenoei et al., 2022; Salem and Ali, 2016). Given this information, we set the average depth and topography ranges to 5 km to 9 km and 3 km to 11 km respectively.

If the structural information is limited, we need to broaden the random parameter ranges to ensure that they cover the solution. In this case, more simulated data is required that comprises various subsurface structures whose shapes and depths are different. This causes data simulation and model training to be computationally more expensive while the accuracy of model predictions would remain the same.

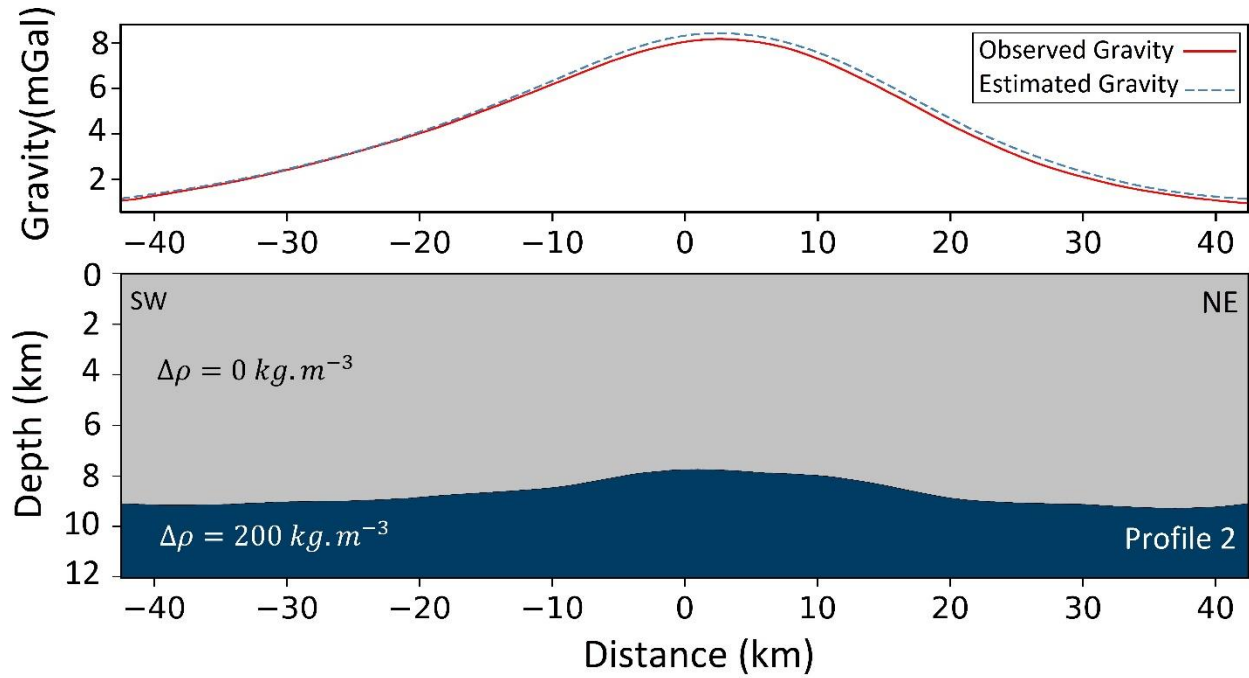


Figure 6-9: Result of the DNN inverse model prediction across profile 2. The predicted subsurface structure is depicted with gray, and dark blue colors, corresponding to sediments, and basement layers, respectively.

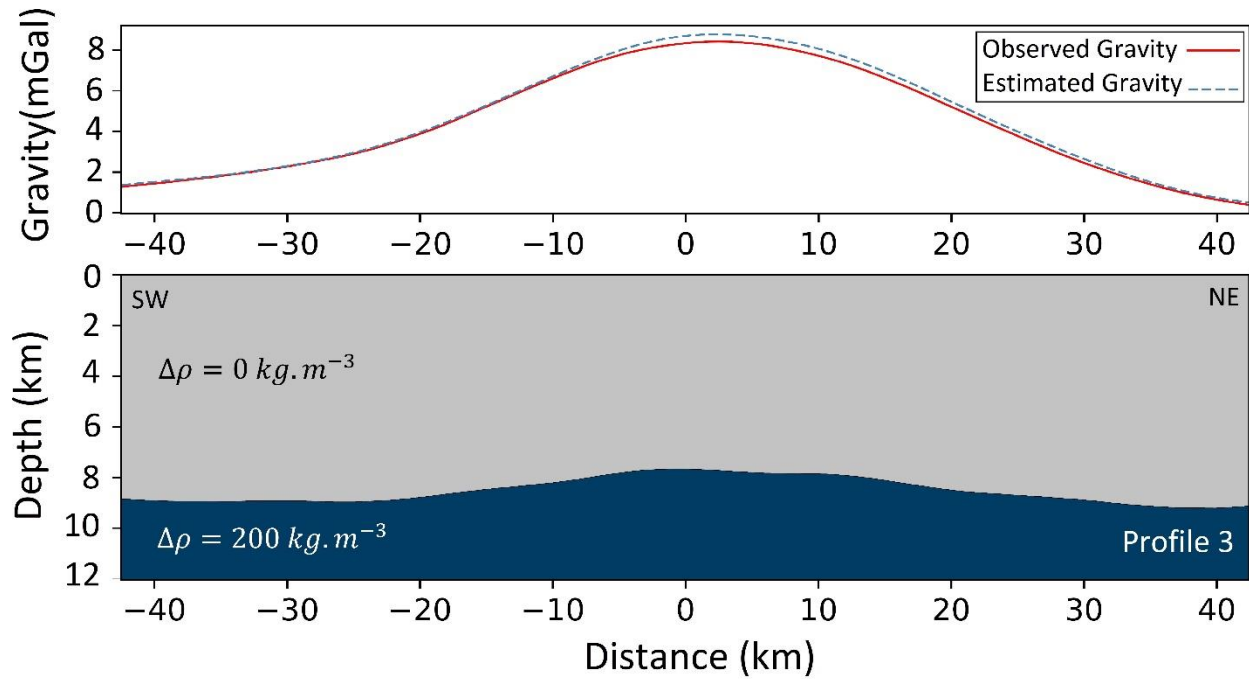


Figure 6-10: Result of the DNN inverse model prediction across profile 3. The predicted subsurface structure is depicted with gray, and dark blue colors, corresponding to sediments, and basement layers, respectively.

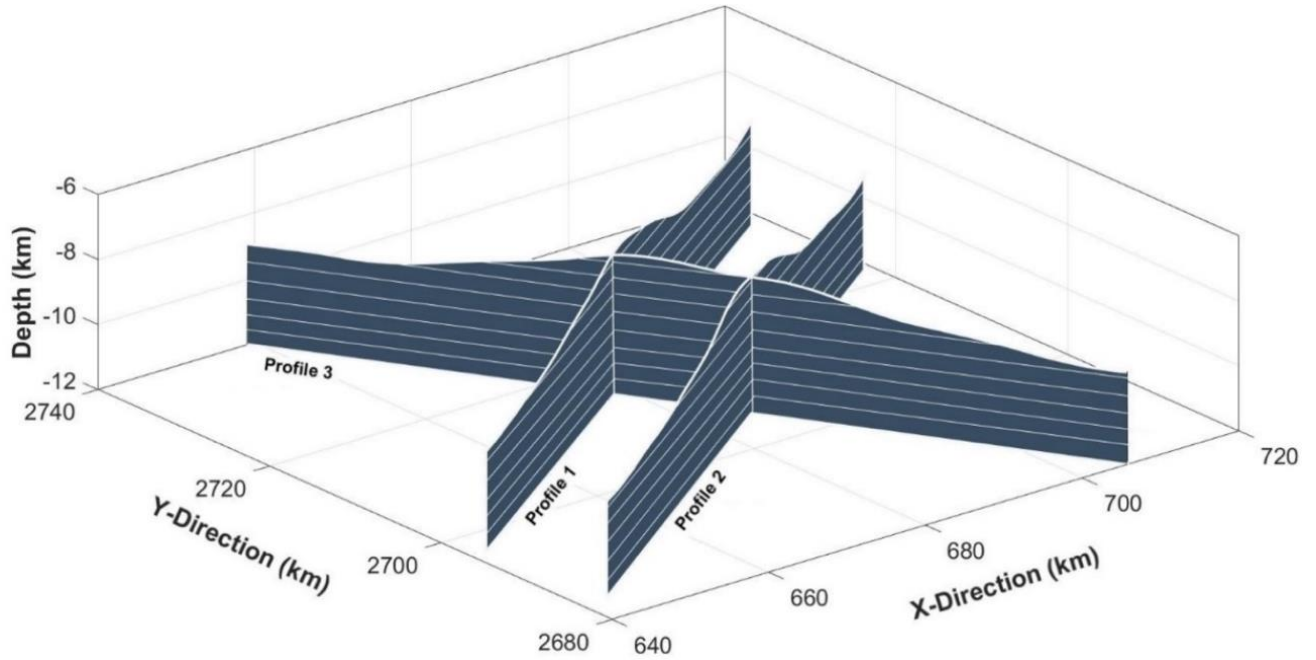


Figure 6-11: Representation of the 3 profiles, profile 1, profile 2, and profile 3.

It is necessary to discuss different assumptions about the data and subsurface parameters that impact the accuracy and resolution of the obtained models. Inversion of gravity anomalies is the mathematical derivation of geometry or density distributions of the subsurface. However, gravity inversion is a notoriously non-unique problem. It means that there are always infinite solutions that fit the gravity data adequately well. The ambiguity arises from the trade-off between the depth of the anomalous mass and its density distribution. Therefore, one of those parameters must be constrained by a priori information. A priori information which is mandatory for gravity inversion is usually acquired from geological and geophysical studies conducted in the target region. Nonetheless, if this information is missing or incorrect, uncertainties may be introduced to the predicted models. In the context of geophysical modeling, accurate density estimates are crucial for interpreting gravity data and inferring the distribution of subsurface anomalies. Estimating density can be challenging, as it often requires making assumptions about the composition and properties of the subsurface.

As explained previously, in DNN gravity inversion the density contrast is invoked as a priori information. To illustrate how uncertainties in density contrasts can affect the accuracy of solutions, we trained four DNN models with density contrasts that are $\pm 15\%$ and $\pm 30\%$ of the assumed density contrast of 200 kg.m^3 . Each model was then used to make estimations on 1000 samples of synthetic data followed by calculating the root mean square error (RMSE) between

the corresponding synthetic basement and the estimated basement. The average RMSE values of the DNN models are summarized in Table 6-2. Figure 6-12 demonstrates the model estimations on an example of synthetic data with an average depth of 8.5 km. Our findings indicate that a 15% error in density contrast can result in roughly a 3% error in topography estimation. In addition, the estimated basement approximately offsets the assumed basement by ~0.5 km if a 30% error is applied in the density contrast.

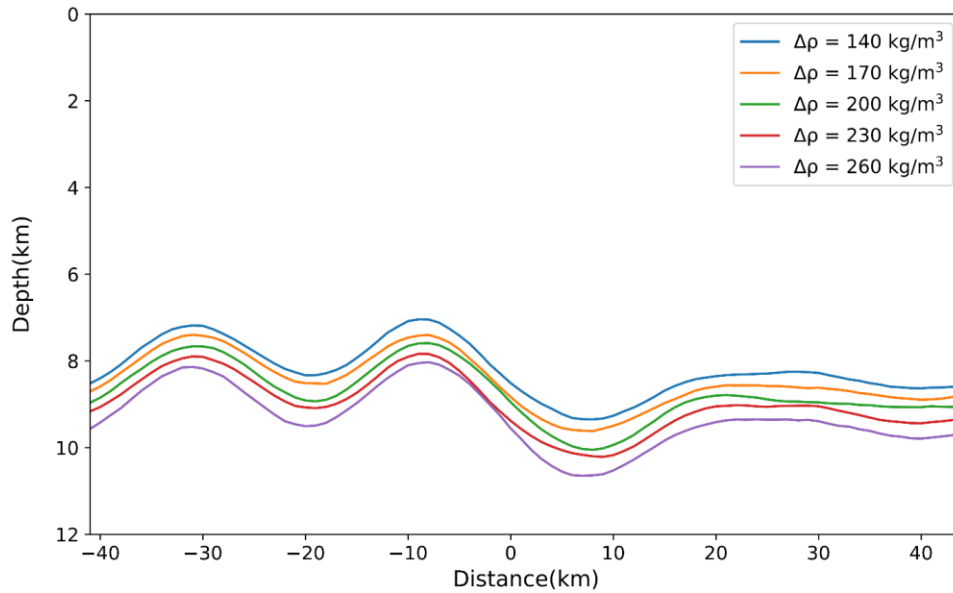


Figure 6-12: Basement topography estimation results using different density contrasts.

As illustrated in Figure 6-12, the estimated topography by different models roughly follows the same trend as density contrast decreases or increases, however, the average depths are shifted. This can be attributed to the relationship between gravity and density. Since gravity is directly proportional to mass, changes in the density of subsurface materials can cause corresponding changes in the measured gravity. Consequently, we expect to predict a deeper basement for larger density contrast.

Table 6-2: Density uncertainty analysis results on basement topography estimations.

Density contrast error (%)	RMSE (km)
-30	0.53
-15	0.27
15	0.26
30	0.56

It is important to note that the topography estimated by different models may differ in shape due to variations in the weights and parameters of the DNN model. These variations arise from differences in the weights and parameters of the respective DNN models employed in the inversion processes. The DNN models used for inversion are trained to learn the complex relationships between the input features and the output variables. During the training phase, the models adjust their internal weights and parameters to minimize the discrepancy between the predicted values and the true values of the subsurface properties.

The other factor that affects the resolution and accuracy of the dataset simulation and DNN model predictions is the quality and quantity of the gravity data. The data is usually contaminated with measurement and correction errors. If data is collected over scattered locations, the chance of capturing the short wavelength variations of the topography is reduced. As a result, a smaller number of anomalies with longer lengths can be selected for the forward model simulation. Moreover, based on Newton's gravitation law, gravity attenuates with increasing distance. This implies that the chance of capturing the gravity effects of short wavelength anomalies decreases as their depths increase. The number and length of the anomalies are dependent on the sparsity of the observed gravity data. This can also affect the resolution of the predicted results of the model.

We used pseudo-gravity data to model the basement of UAE. To do so we converted the magnetic anomaly (Figure 2-3a) to the pseudo-gravity anomaly. The magnetic data is acquired on a grid with a grid cell size of 400 m (Ali and Watts, 2009). We sampled the pseudo-gravity anomaly over the three profiles with a spacing of ~1 km. This spacing is adequate for capturing the short and long wavelengths of the topography. However, the pseudo-gravity anomaly over the target region implies a smooth variation of the basement topography, as predicted by our DNN model.

DNN has significantly contributed to solving the non-uniqueness and non-linearity aspects of our inverse problems. Nevertheless, DNN models trained for a specific region are impractical for interpreting regions with different dimensionality and geological properties. In fact, such models need to be re-trained if the major physical and structural parameters are modified. In addition, database simulation and model training is time-consuming. When encountering such issues, incorporating high-level programming languages on modern computers has been promising for optimizing the training processes.

6.6 Conclusion

A new technique for DNN inversion of gravity anomalies to estimate basement topography was developed. A gravity dataset was simulated by random assignment of several parameters to a two-layer forward model. Subsequently, a DNN model was trained using the simulated dataset to conduct nonlinear mapping of gravity anomaly to basement topography. The model performance was tested on the unseen actual and noise-added synthetic gravity anomalies. The outputs show a significant fit between the predicted and simulated basement topography even after adding 10% noise to the gravity data.

The DNN model was employed to estimate the basement topography over the Ghasha hydrocarbon reservoir in offshore Abu Dhabi, UAE. The predictions were conducted using pseudo-gravity anomalies over three profiles. The basement topography obtained between 7.3km to 9.4 km supports the results of other research conducted in the same region.

Furthermore, chapter seven delves into the estimation of basement topography using magnetic data. The procedures for dataset simulation, DNN model training, and prediction follow similar approaches to those employed in this chapter.

Chapter Seven: DNN Inversion of Magnetic Data

7.1 Introduction

The objective of magnetic inversion is to determine the distribution of subsurface magnetic anomalies. By analyzing the magnetic anomalies, we can infer valuable information about the geological formations and structural characteristics of the anomalous bodies.

In this chapter, the focus is on applying the DNN inversion technique to model the basement topography using magnetic anomalies. The methodology for dataset simulation, as described in chapter five, is followed to generate the required training dataset. The simulated dataset includes magnetic anomalies as input features and the corresponding depth-to-basement values as labels.

The DNN inversion model is trained using the simulated dataset, where the network learns the complex mapping between the magnetic anomalies and the underlying basement topography.

To assess the performance of the trained model, evaluations are conducted using both noise-free and noise-added synthetic data. The noise-free data allows for a baseline assessment of the model's accuracy and robustness. The noise-added data provides a more realistic representation of the actual measurement conditions, accounting for potential noise and uncertainties in the observed magnetic anomalies.

Finally, the trained DNN inversion model is applied to estimate the basement topography from actual aeromagnetic anomalies offshore UAE.

By leveraging the power of DNN inversion and utilizing the magnetic anomalies, this chapter contributes to the understanding and characterization of the basement topography in the study area. The results obtained from the DNN inversion provide valuable information for geological and geophysical interpretations, aiding in the exploration and assessment of potential hydrocarbon reservoirs offshore UAE.

7.2 Magnetic Dataset Simulation

The forward model is created by dividing the subsurface into two layers: sediments and basement. Two separate datasets are simulated, each targeting different lengths of observation profiles of 140 *km* and 200 *km*. Since the sediment layer is transparent to magnetic effects, its susceptibility is set to zero. The basement of the UAE is composed of high-grade metamorphic and igneous rocks (Allen, 2007; Bowring et al., 2007). The basement susceptibility ranges from

~ 0.001 SI to ~ 0.016 (Ghalenoei et al., 2022; Salem and Ali, 2016). Therefore, the average susceptibility of -0.008 SI is chosen for the basement.

The lower boundary of the lower layer is fixed at 12 km. The heights of the prisms are adjusted during the dataset creation process. The random forward model parameter ranges are provided in Table 6-1. The average depth and topography parameters are set to 5 *km* to 9 *km* and 3 *km* to 11 *km*. Moreover, the number of anomalies and length of the anomalies are again set to be 1 to 8 anomalies and 8 km to 40 km respectively. The model is then extended at both lateral sides to avoid potential edge effects.

Dataset creation was completed in 14 minutes using the multiprocessing library on a PC with Intel Core-i7CPU 3GHz and 16.0 GB RAM. The final simulated datasets comprise 200,000 instances with the magnetic anomaly of each forward model as the input features and corresponding basement topography as labels. Figure 7-1 shows three random simulated forward models together with their magnetic anomalies.

7.3 DNN Magnetic Inversion

The DNN model is configured adopting the same procedure and hyperparameters as for the inversion of gravity data (chapter six).

The Sequential class of the Keras library is used to train the DNN inverse model. The grid search algorithm (Pedregosa et al., 2011) is applied to optimize the hyperparameters. Accordingly, the optimal DNN model consisted of 3 hidden layers, each with 300 neurons. The weight initializer and the activation function are chosen to be Glorot Normal and Elu. The RMSprop technique optimizes the model parameters with an initial learning rate of 0.0001. The dropout regularization technique with a dropout rate of 0.1 is used to avoid overfitting in the DNN model training.

The DNN model was trained using the TensorFlow library with a batch size of 32 and in 30 epochs and conducted on an NVIDIA GeForce GTX 1660 Ti GPU.

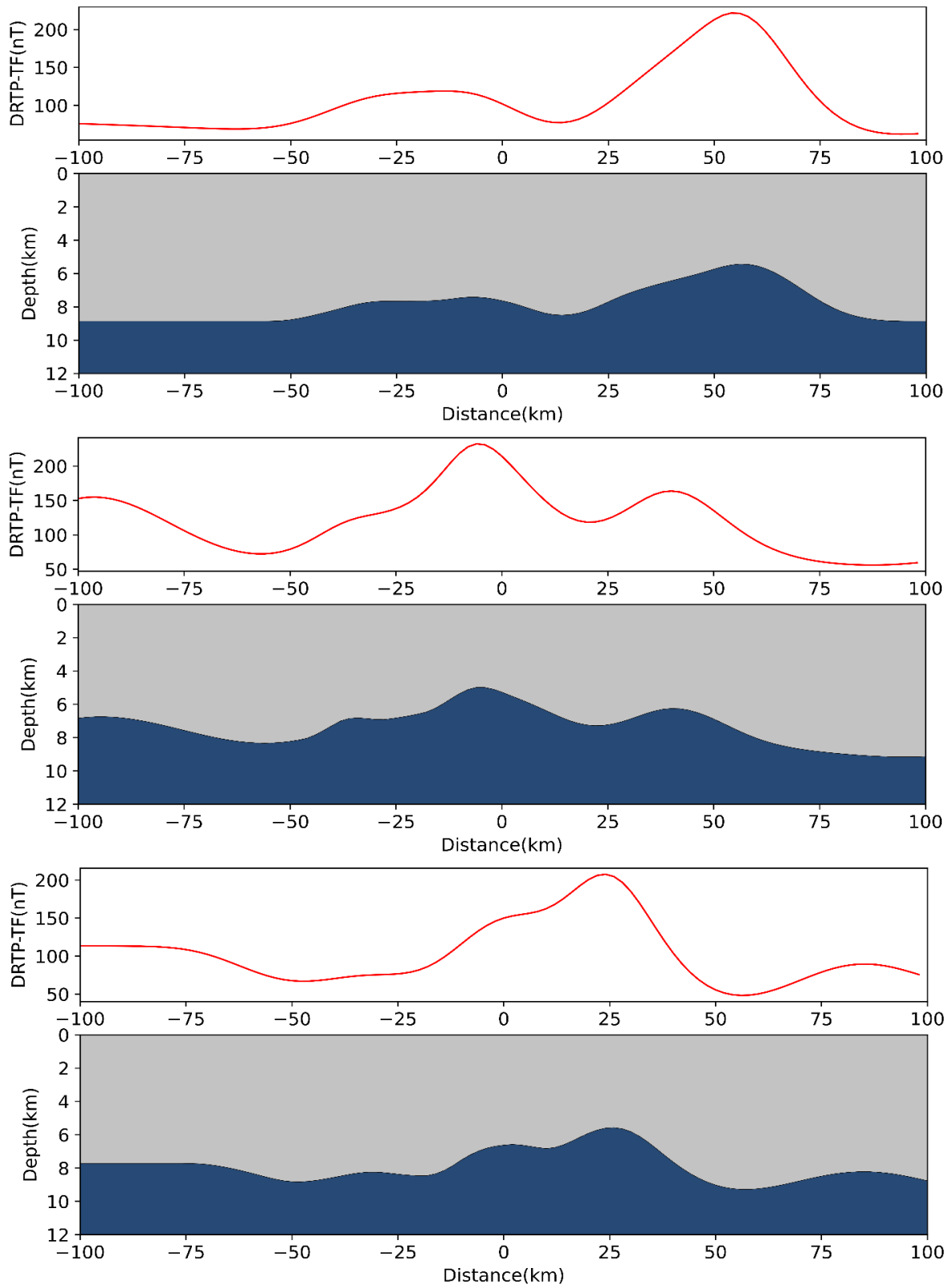


Figure 7-1: Samples of a simulated dataset. The red curve represents the synthetic magnetic in nT. The subsurface model is depicted with magnetic and dark blue colors, corresponding to sediments, and basement layers, respectively.

7.3.1 Error Analysis

To evaluate the performance of the Deep Neural Network (DNN) model, the dataset is divided into three subsets: the training set, the validation set, and the test set. The training set is used to train the DNN model by adjusting its parameters. The validation set is utilized to fine-tune the hyperparameters of the model, ensuring optimal performance. The test set is employed to assess the final performance of the trained model.

The evaluation of the model involves the use of the cross-validation technique, which involves splitting the data into three folds. This technique helps to adjust the hyperparameters of the model during training, ensuring optimal performance.

The MSE metric is employed to score the model's performance. This metric quantifies the average squared difference between the predicted and actual values. A lower MSE score indicates better model performance.

During the training process, the accuracy of the model on both the training and validation sets is monitored after each epoch. This monitoring allows for the assessment of the model's progress and helps identify any overfitting or underfitting issues. The learning curve, depicting the model's performance over the number of epochs, is plotted to visualize the training progress (Figure 7-2). The evaluation score on the test set is 0.05 km^2 . Both training and validation MSE decrease as the number of epochs increases to a point of stability with a minimal gap between them. This means that the model is performing well on the training data and generalizing well to new data.

7.4 DNN Magnetic Model Evaluation

The performance of the trained model is assessed on unseen synthetic magnetic anomalies to ensure it can generalize well to new data and is not overfitting to the training data. Correspondingly, the DNN model is made to predict the basement topography on several unseen magnetic data with some examples illustrated in Figure 7-3.

Accordingly, the predicted basement topography correlates with the true simulation including the average depth of the basement and the shape and location of the basement anomalies. Following, the average MSE value between the true and predicted basement topography is calculated to be 0.02 km^2 .

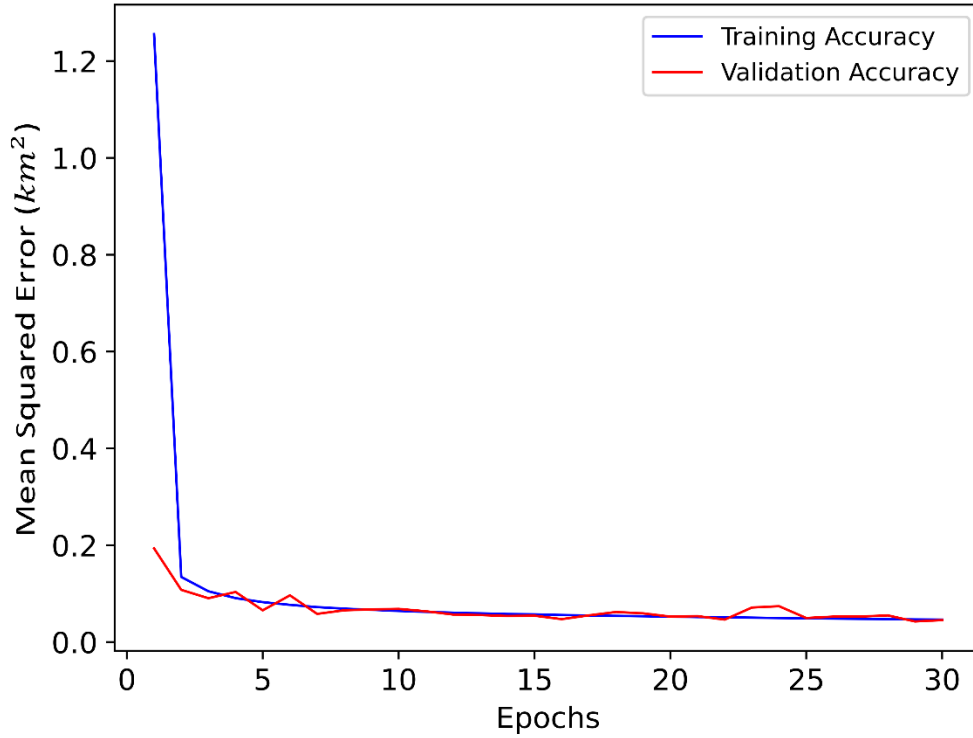


Figure 7-2: Plot of Training and validation accuracy against epochs.

It is also important to test the DNN inversion model's performance against noise to assess its robustness and generalization capabilities. Furthermore, adding noise to the input simulated magnetic data allows us to simulate real-world scenarios where the data may contain noise. Gaussian noise is used to simulate the effects of noise in real-world data. It is characterized by a normal distribution with zero mean and standard deviation equal to that of simulated magnetic data. The DNN model's performance against noise was tested on magnetic data with added Gaussian noise values of 5% and 10% which means the noise amplitude is 5% and 10% of the signal's amplitude. The results are shown in Figure 7-4 and Figure 7-5 with average MSE values of 0.027 km^2 and 0.03 km^2 , respectively.

Since the model fits the simulated data well and also performs well on noise-added data, it suggests that the model has good generalization capabilities and is not overfitting the training data. In other words, it demonstrates that the DNN magnetic inversion model has satisfactory robustness against noise-contaminated data and can perform well on real magnetic data.

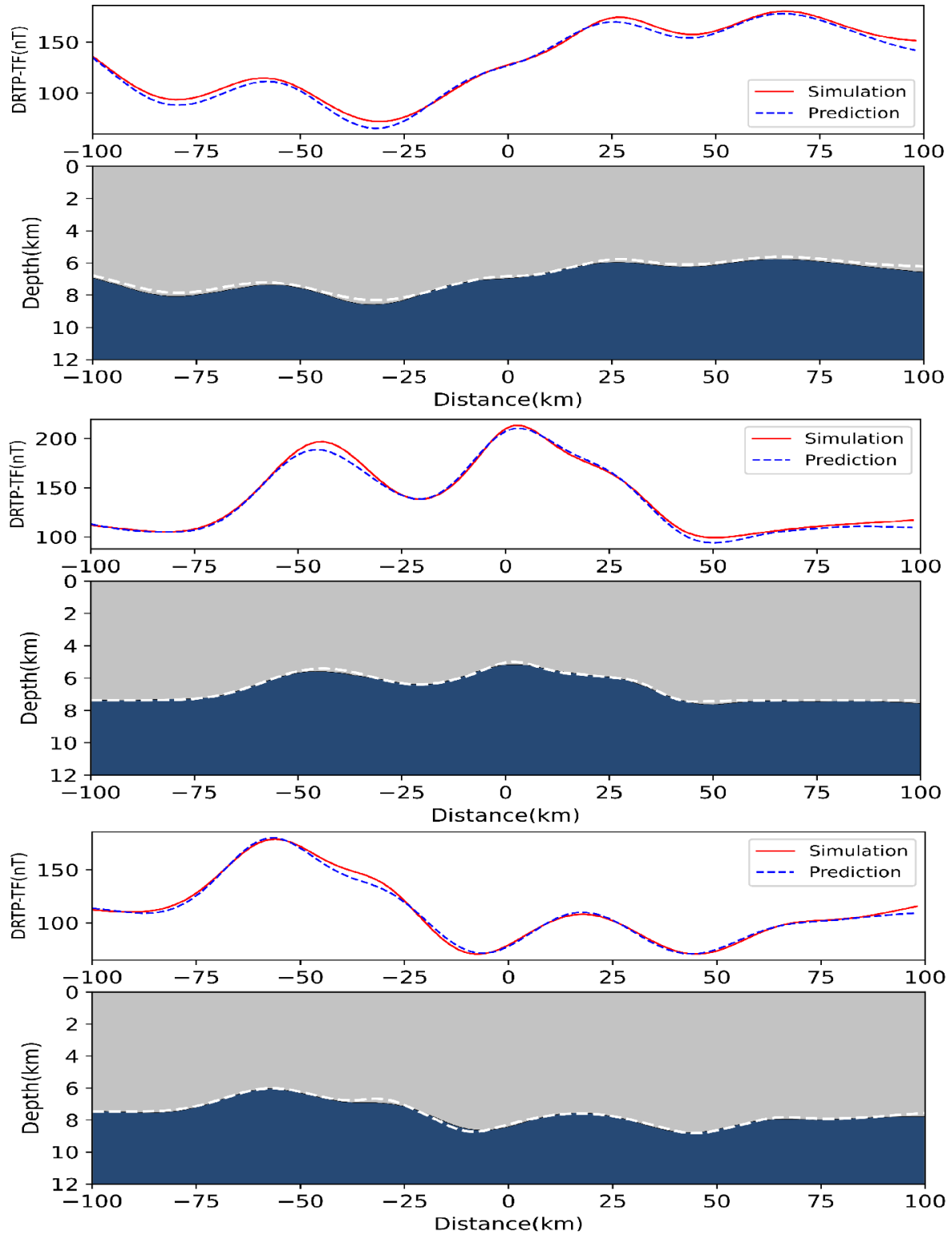


Figure 7-3: Samples of DNN magnetic model prediction results. The red curve represents the synthetic magnetic fed into the DNN model. The dashed blue curve represents the estimated magnetic of the predicted subsurface structure. The predicted subsurface structure is depicted with gray and dark blue colors, corresponding to sediments and basement layers, respectively. The white dashed curve represents the actual basement topography.

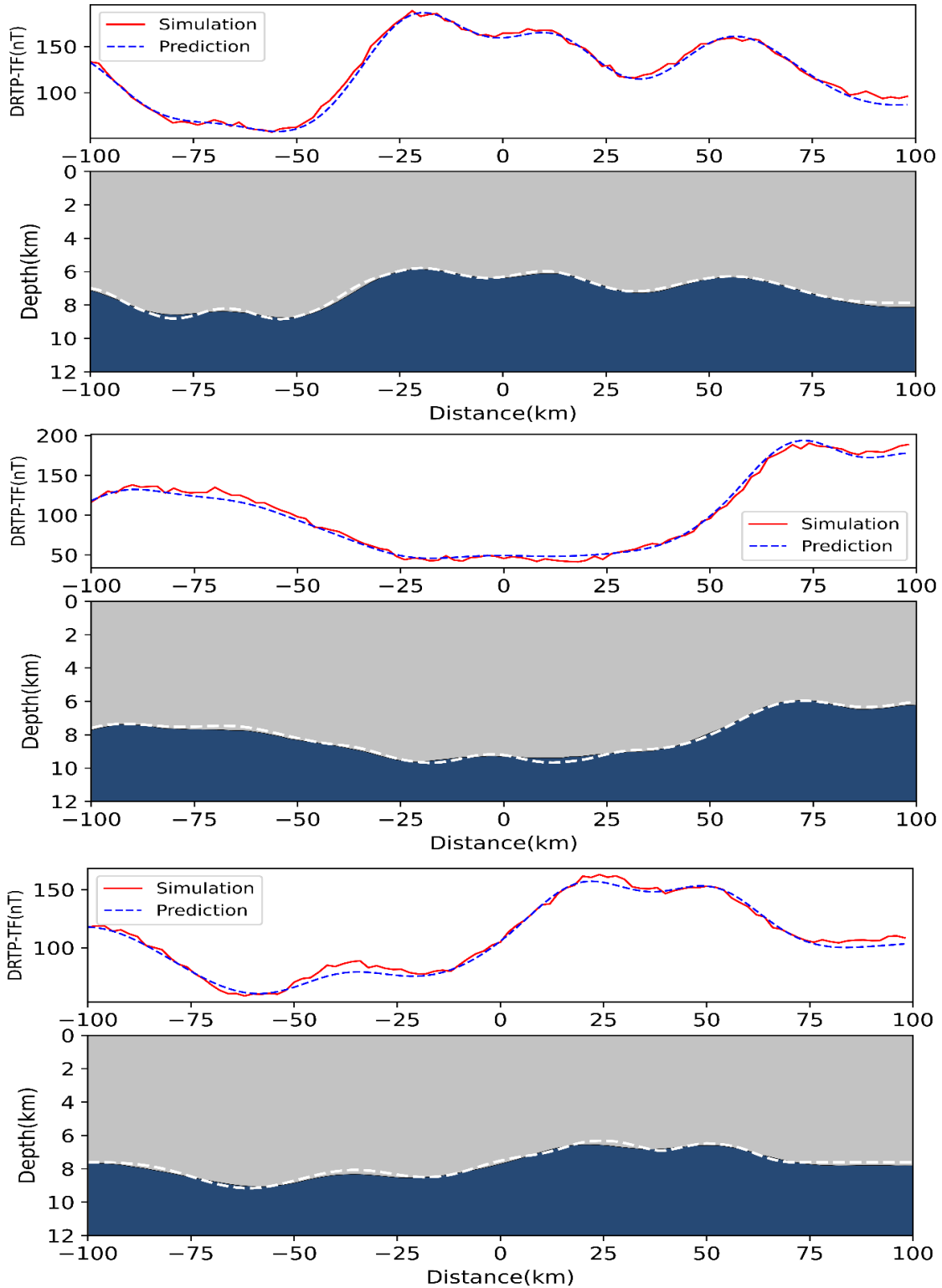


Figure 7-4: Samples of DNN model prediction results. The red curve represents the 5% Gaussian noise-added synthetic magnetic anomaly fed into the DNN model. The dashed blue curve represents the estimated magnetic anomaly of the predicted subsurface structure. The predicted subsurface structure is depicted with gray and dark blue colors, corresponding to sediments and basement layers, respectively. The white dashed curves represent true basement topography.

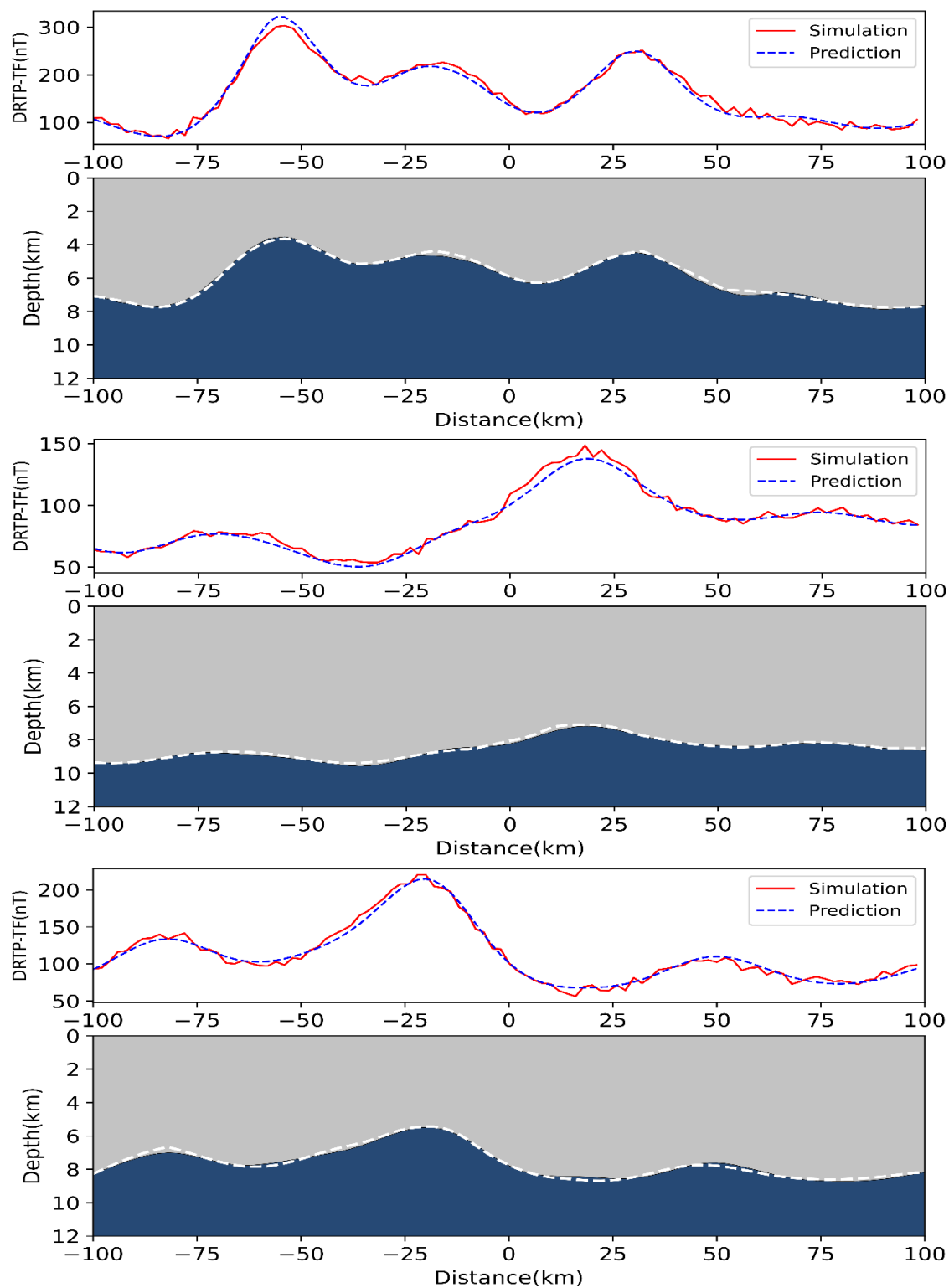


Figure 7-5: Samples of DNN model prediction results. The red curve represents the 10% Gaussian noise-added synthetic magnetic anomaly fed into the DNN model. The dashed blue curve represents the estimated magnetic anomaly of the predicted subsurface structure. The predicted subsurface structure is depicted with gray and dark blue colors, corresponding to sediments and basement layers, respectively. The white dashed curves represent true basement topography.

7.5 Results and Discussion

Basement modeling is important for understanding the geology and hydrocarbon potential of a region and can aid in the identification and exploration of hydrocarbon resources (Palumbo et al., 2002). Furthermore, the structure and properties of the basement can influence the formation and distribution of sedimentary basins, which in turn can impact the occurrence and distribution of hydrocarbons. For example, the presence of faults or folds within the basement can influence the location and shape of sedimentary basins, which can impact the trapping and accumulation of hydrocarbons.

Magnetic data are inverted to obtain the structural model of the high susceptibility anomalous sources in the subsurface. The accuracy and resolution of the subsurface models are affected by the choice of the synthetic model parameters and the quality of the observations. A priori information is required to constrain the susceptibility distribution of the subsurface. The structural parameters are chosen from ranges of values that best serve the characteristics of the subsurface.

The trained DNN inverse model is applied to estimate the basement topography in offshore UAE across three profiles extracted from the magnetic map of the region (Figure 7-6). Profile 1 crosses the giant hydrocarbon fields of the region, Ghasha and Zakum along the SW-E direction. Profile 2 passes through Arzanah, Bu Haseer, and Umm Shaif reservoirs from SW to NE. Profile 3 bisects the first two profiles and crosses the Umm Shaif and Zakum reservoirs along NW to SE.

The results of the basement topography estimations are shown in Figure 7-6 through Figure 7-8. The top of the basement ranges from ~ 6.4 km to ~ 9.75 km over Profile 1 with the shallowest part located below the Ghasha oil field reservoir. The deepest basement below the Zakum oil field is between ~ 9.45 km to ~ 9.75 km as derived from Profile 1 and Profile 3. The results also show that the basement reaches another high approaching the Nasr and the Umm Shaif fields around 6.9 km.

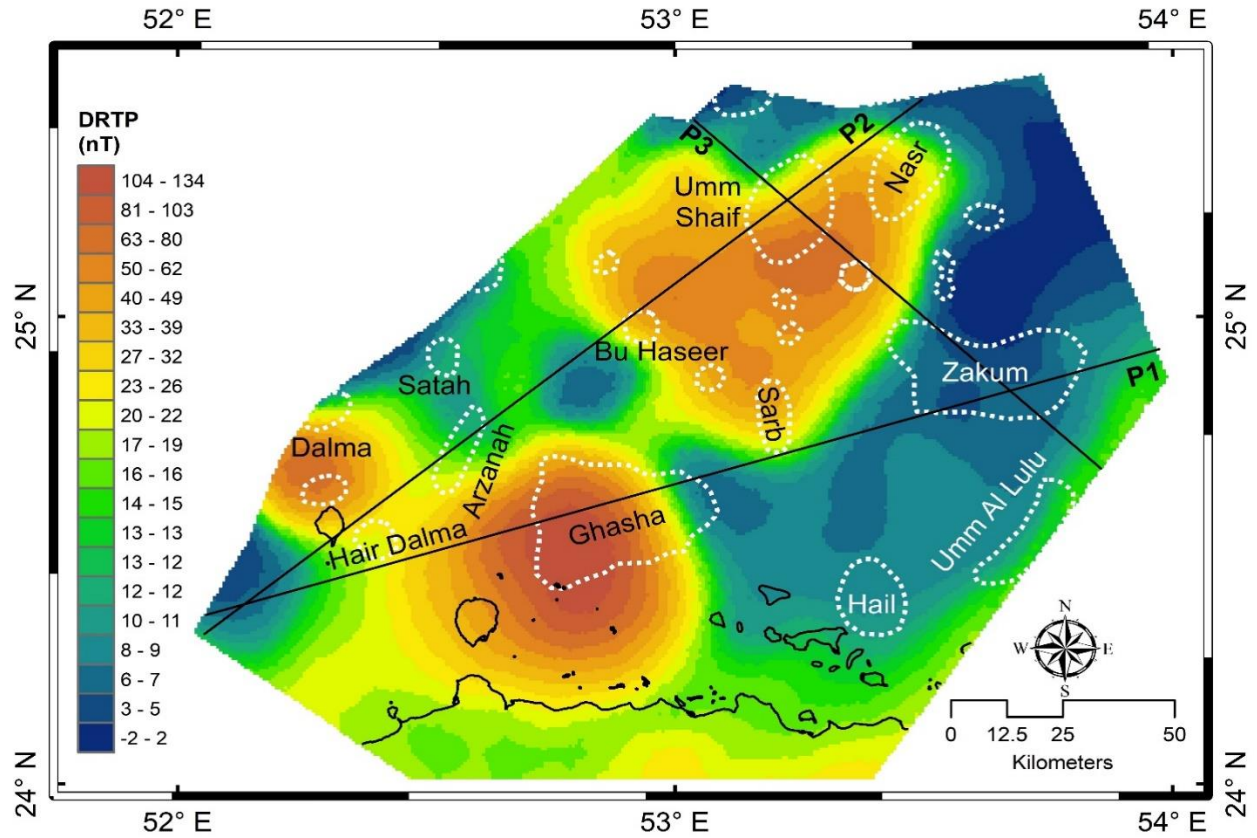


Figure 7-6: Location of the profiles over pseudo-gravity anomalies map of the study area together. The dotted white enclosures illustrate the boundaries of oilfields.

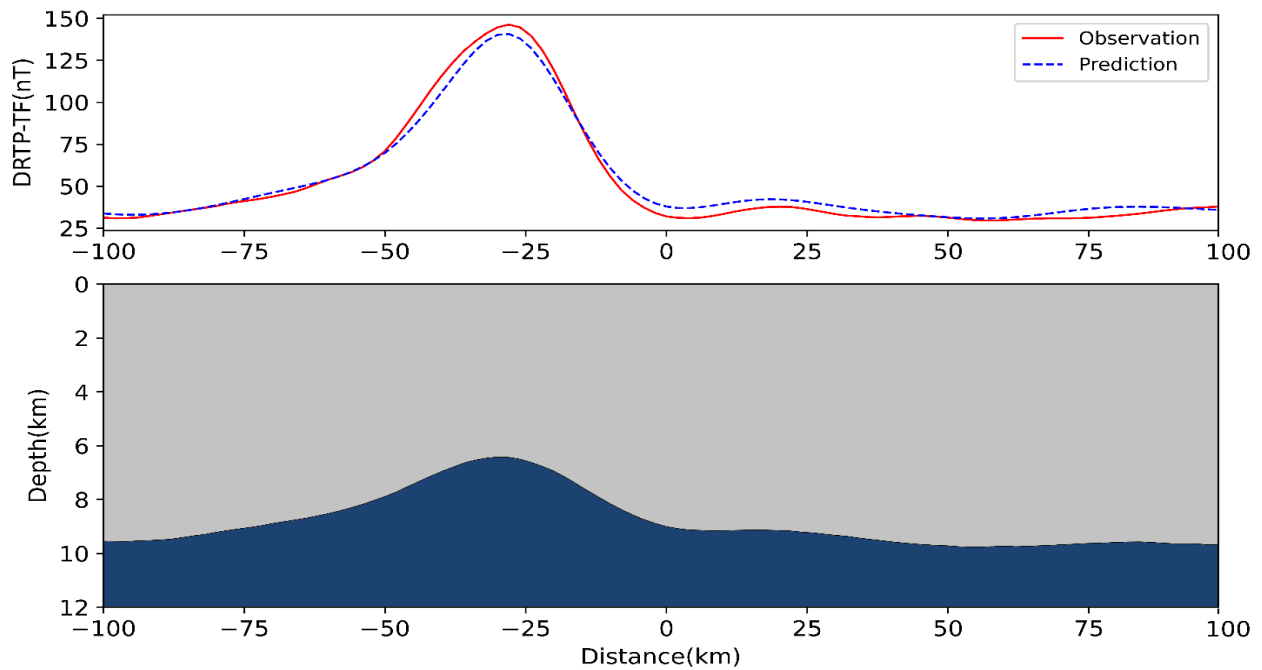


Figure 7-7: Result of the DNN inverse model prediction across Profile 1. The predicted subsurface structure is depicted with gray and dark blue colors, corresponding to sediments and basement layers, respectively.

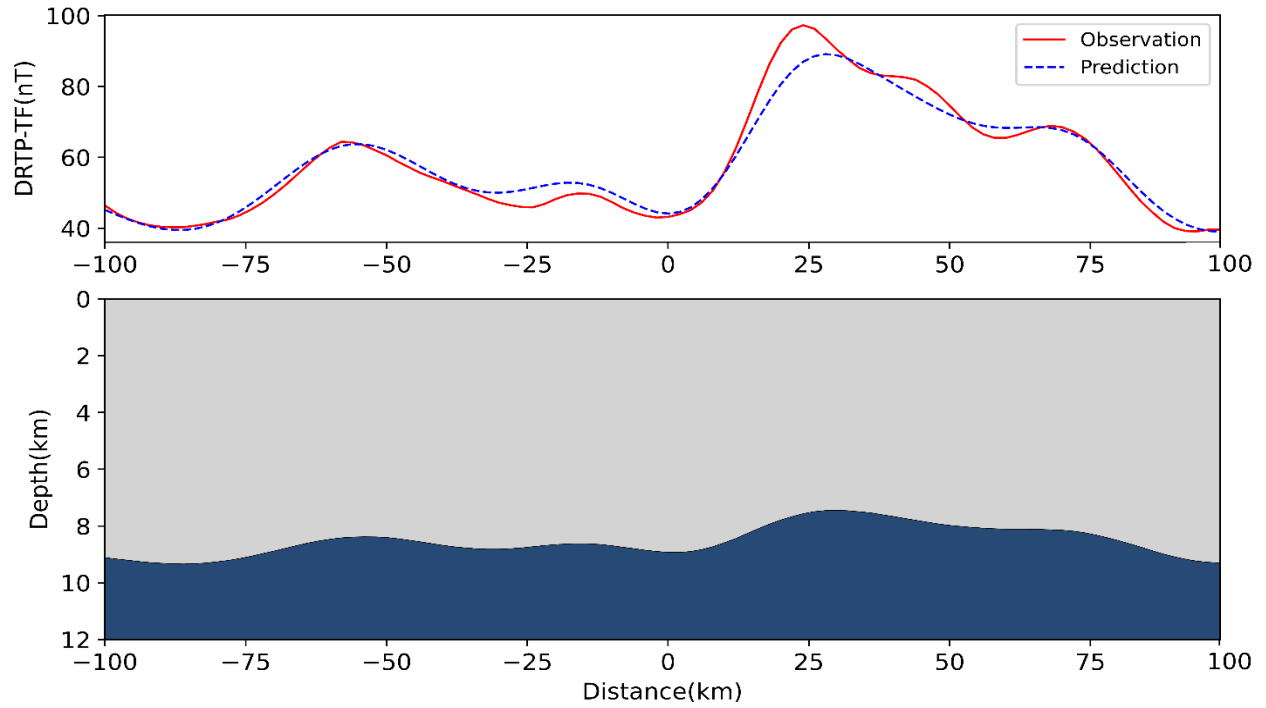


Figure 7-8: Result of the DNN inverse model prediction across Profile 2. The predicted subsurface structure is depicted with gray and dark blue colors, corresponding to sediments and basement layers, respectively.

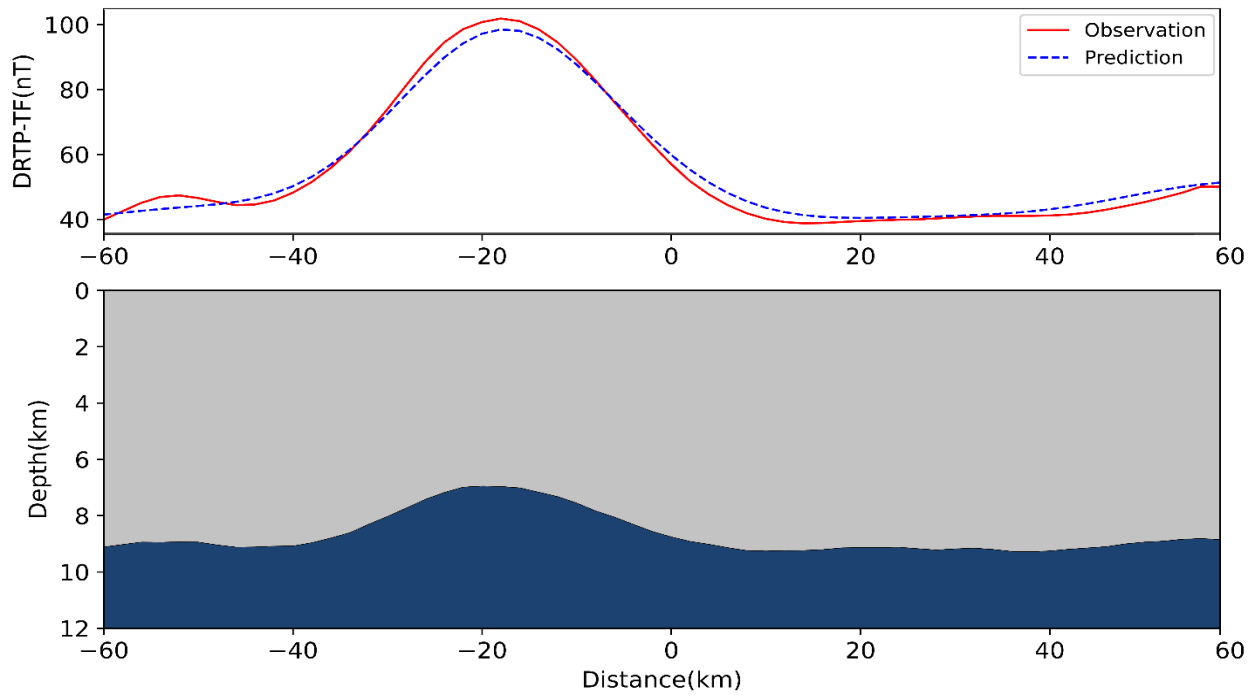


Figure 7-9: Result of the DNN inverse model prediction across Profile 3. The predicted subsurface structure is depicted with gray and dark blue colors, corresponding to sediments and basement layers, respectively.

7.6 Conclusion

This chapter focused on the application of the DNN inversion technique for modeling the basement topography using magnetic anomalies. To generate the necessary training dataset, the dataset simulation methodology described in chapter five was followed.

By implementing the DNN inversion technique on the real magnetic anomaly, this chapter contributed to advancing our understanding of the subsurface geology offshore UAE.

Chapter eight focuses on the joint inversion of gravity and magnetic data and its application in interpreting salt-basement structures over hydrocarbon reservoirs offshore UAE. The joint inversion approach offers enhanced insights into the complex geological structures, contributing to more effective hydrocarbon exploration and resource evaluation in the region.

Chapter Eight: Joint DNN Inversion of Gravity and Magnetic Data

8.1 Introduction

As previously stated, one of the fundamental problems of geophysical inversions is the inherent non-uniqueness of their solutions. This means that multiple models can fit the observed data equally well, making it difficult to determine the true subsurface structures. Regularization techniques have traditionally addressed this issue, by introducing various constraints and simplifications to inversion parameters and subsurface solutions (Fernández-Martínez et al., 2014; Lin and Zhdanov, 2018; Zhdanov, 2002).

As suggested by multiple researchers introduced below and further developed by this research, another effective solution toward solving the non-uniqueness, is the joint inversion of geophysical data that pertains to different subsurface physical properties. Integrated interpretation of geophysical data applies complementary information that enhances the quality and accuracy of the subsurface models. Several techniques have been conducted on joint inversion of geophysical data including sequential inversion, cross-gradient, and Bayesian approaches (Carrillo et al., 2022; Ghalenoei et al., 2022; Kabirzadeh et al., 2021; Fregoso et al., 2020; Gross, 2019; Lin and Zhdanov, 2018; Gallardo and Meju, 2007; Haber and Oldenburg, 1997).

Nonetheless, joint inversion of geophysical data can be a challenging task as different datasets are sensitive to various subsurface properties. Combining datasets that are not compatible in resolution and accuracy can lead to inconsistencies in the final interpretation. Moreover, the computational complexity of combining multiple geophysical datasets can be significant, especially when dealing with large datasets or computationally intensive inversion methods. This can result in long computation times and can make the joint inversion process impractical for certain applications.

Joint geophysical inversion using DNNs is a state-of-the-art technique that involves learning the complex relationship between the geophysical datasets and the subsurface properties. DNN joint inversion has several advantages over traditional techniques. It can drive complex nonlinear

relationships between the features in high-dimensional datasets while being computationally efficient. Furthermore, DNNs can be trained to incorporate prior knowledge about the subsurface structure, thereby improving inversion accuracy.

However, there are some limitations to using DNNs for geophysical inversion. For example, the results are dependent on the quality and quantity of the input data. Furthermore, DNNs are susceptible to overfitting, which occurs when the network becomes too complex and begins to fit the noise in the data rather than the underlying signal. Therefore, it is important to carefully design the network architecture and regularization techniques to avoid overfitting.

Targeting complex subsurface structures, a joint inversion technique of gravity and magnetic anomalies is developed using DNN to prevail over the non-uniqueness and nonlinearity of the inverse problems. This thesis aims to apply the proposed method to image the salt-basement structures of hydrocarbon reservoirs in offshore UAE.

The step-by-step procedure for DNN joint inversion of gravity and magnetic data to construct a 2.5D model of the subsurface structure is as follows: First, a training dataset is simulated using the technique proposed in chapter five. Accordingly, the subsurface is partitioned into sediments, salts, and basement layers representing our base forward model. By changing a few random parameters, tens of thousands of different versions of the model are generated and their gravity and magnetic anomalies are calculated. The dataset is created by putting together the gravity and magnetic anomalies as input and depth-to-salts and depth-to-basement as labels. A DNN model is trained using the simulated dataset to conduct nonlinear inverse projection of the gravity-magnetic anomalies to the salts-basement topography. The DNN model performance is evaluated by making predictions on actual and noise-added synthetic gravity and magnetic anomalies. Finally, the verified DNN model has been applied to predict the salts and the basement over the profiles extracted on the gravity and magnetic anomalies of the hydrocarbon reservoirs in UAE.

8.2 Joint Gravity and Magnetic Dataset Simulation

The dataset simulation technique proposed in chapter five is implemented to simulate the required dataset for the DNN joint inversion of UAE gravity and magnetic data. For this purpose, a 2.5D forward model is designed to divide the subsurface into three layers: sediments, salts, and the basement. The physical parameters of the forward model including density and susceptibility of the layers are assigned based on the a priori information on the region. The average density of

the salt layer obtained from the Infracambrian Hormuz salts outcropping in the Jabal Dhanna (Figure 2-1) is 2200 kg.m^{-3} . The average density of 2550 kg.m^{-3} is assumed for the sediments as derived by well logs (Geng et al., 2020). The susceptibilities of the sediments and salt layers are negligible and thus are set to zero. The basement of the UAE is composed of high-grade metamorphic and igneous rocks (Allen, 2007; Bowring et al., 2007) with an assigned density of 2800 kg.m^{-3} . The basement susceptibility ranges from $\sim 0.001 \text{ SI}$ to ~ 0.016 (Ghalenoei et al., 2022; Salem and Ali, 2016). Therefore, the average susceptibility of 0.008 SI is chosen for the basement.

The layers are composed of rectangular prisms (Figure 5-1). The length of the layers and each of the prisms is specified based on the dimensions and resolutions of the anomalies being investigated and the length of the observation profiles. A width of 20 times the prism's length is used for the layers to mathematically satisfy the infinite width of the 2.5-D model. The model is then extended at both lateral sides to avoid potential edge effects. It should be noted that the adopted dimensions of the forward model cannot be modified during the dataset simulation and remain fixed.

The lower boundary of the model is set to 12 km depth while the topography of the salt and basement layers are iteratively changing throughout dataset simulation to create different representations of the forward model. To accomplish this, several random parameters are defined that modify the depths and configurations of the salt and basement layers (Table 8-1).

Studies conducted on the UAE hydrocarbon reservoirs suggest a deep basement overlain by thick sedimentary and salt strata (Ali et al., 2017; Obaid et al., 2014). As a result, the average depth of the basement is chosen to fall between 5 km to 9 km with its topography ranges from 3 km to 11 km . The average depth of the salt layer is set to fall between 3 km and the selected average depth of the basement. The salt topography fluctuates between 2 km and 8 km , respectively. To prevent the salt and basement layers to overlap, a tolerance of 200 m is imposed as the required minimum gap between these two layers. To create both short-wavelength and long-wavelength anomalies, the algorithm randomly selects 1 to 8 the number of anomalies with lengths between 2 km to half the length of the observation profile. For example, if the length of the model is 80 km , the maximum length of the model would be 40 km .

Given the number of data to be simulated, in each iteration, a forward model randomly selects parameters from the predefined ranges of values. The salt and basement layers are initially given

two average depths that are chosen at random from the respective ranges. Then, a random number of anomalies of various lengths and heights are generated and distributed at random positions loaded on top of each layer's average depth. The Gaussian function is used to generate anomalies with zero mean and standard deviation equal to the lengths of the anomalies.

Following the simulation of each forward model, their gravity and magnetic effects are calculated over the observation points.

Table 8-1: Random parameter ranges of the salt and basement layers considering a forward model with 80 km length.

Parameter	Salts	Basement
Average depth (km)	3-Average basement depth	5-9
Topography range(km)	2-8	3-11
Length of anomalies (km)	2-40	4-40
Number of anomalies	1-10	1-8

Targeting two different lengths of observation profiles, two forward models are simulated with 140 km and 200 km and 2 km spacing respectively. The resulting simulated dataset comprises gravity and magnetic anomalies as input features and depth-to-salts and depth-to-basement values as their associate labels. Dataset creation was completed in 47 minutes for 200000 samples using the multiprocessing library on a PC with Intel Core-i7CPU 3GHz and 16.0 GB RAM.

Figure 8-1 illustrates three examples of the simulated dataset as pairs of synthetic gravity and magnetic anomalies and corresponding subsurface structure including sediments, salts, and basement as illustrated with gray, light blue, and dark blue colors, respectively.

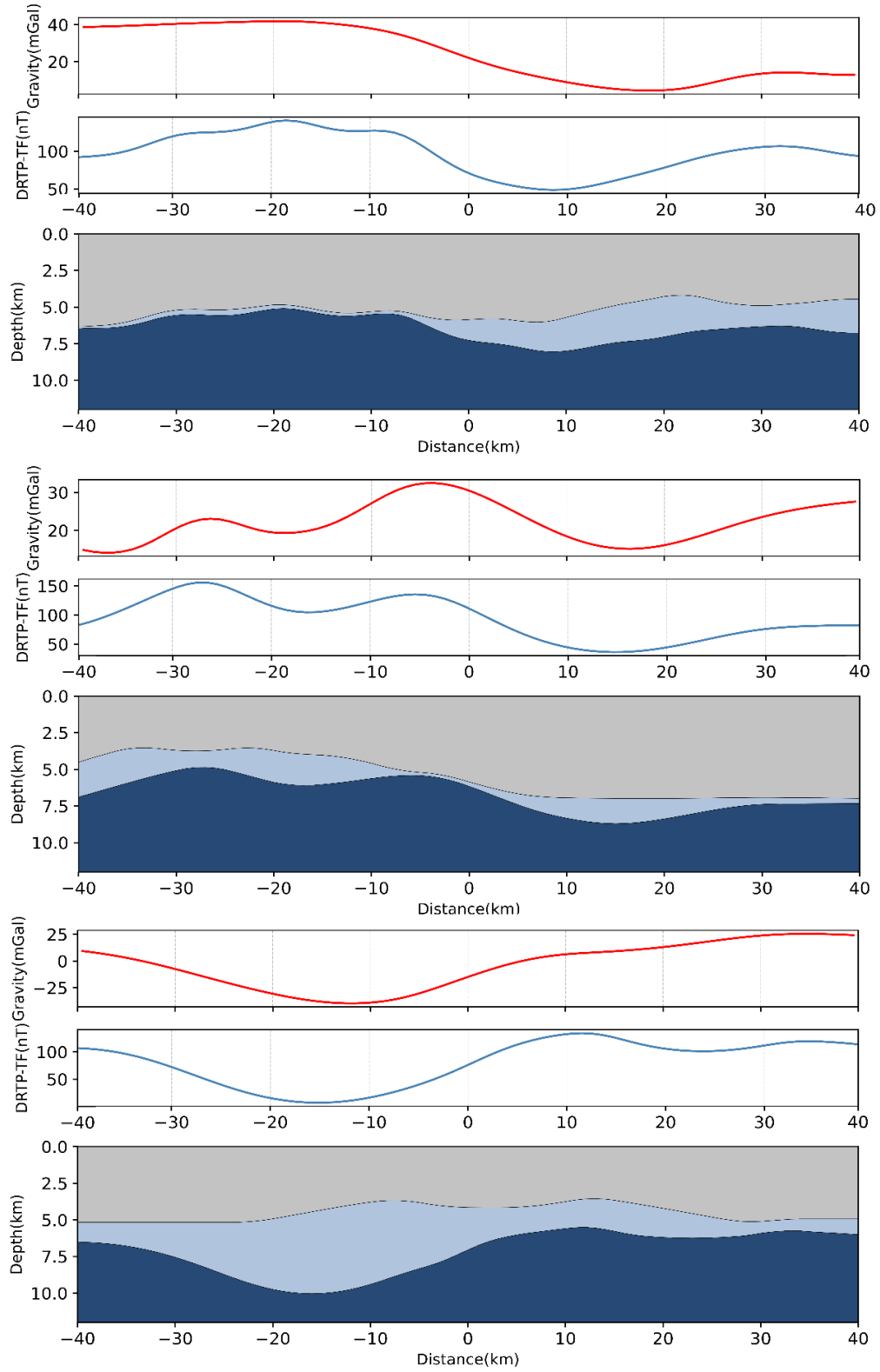


Figure 8-1: Samples of a simulated dataset. The red curve represents the synthetic gravity in mGal, and the blue curve represents the DRTP anomaly in nT. The subsurface model is depicted with gray, light blue, and dark blue colors, corresponding to sediments, salts, and basement layers, respectively.

8.3 DNN Joint Inversion of the Gravity and Magnetic Data

This section describes the procedures of training and configuring the DNN model to conduct nonlinear joint inversion of gravity and magnetic data.

A DNN model has been trained to learn the mapping between the input observed gravity and magnetic anomalies and the output subsurface structure. The Sequential class of the Keras library is used in Python to construct the perceptron feedforward model. Some of the hyperparameters are configured the same as those used in chapter six.

The number of hidden layers and the units in each layer are chosen to be 3 and 300 respectively. The Glorot initializer is used to assign initial random weights to the layers. The sum of weighted inputs of the hidden layers is passed through the Elu activation function. The DNN model is trained using the RMSprop optimizer to minimize the difference between the predicted model parameters and the true model parameters. The initial learning rate is set to 0.0001. To avoid overfitting in the DNN model training, the dropout regularization technique is used with a dropout rate of 0.1. Moreover, Mean Square Error (MSE) is used as the loss function to measure the difference between the network outputs and the actual labels.

The DNN model was trained using the TensorFlow library with 32 batch sizes in 30 epochs. The model training is conducted on an NVIDIA GeForce GTX 1660 Ti GPU.

8.3.1 Error Analysis

Regarding model evaluation during and after the training, the dataset is split into training (90%) and test (10%) sets. The training set is used to learn the parameters of the DNN model. During model training, 10% is held out to validate the model. To monitor the accuracy of the model, the MSE metric is calculated for both training and validation sets after each epoch. The learning curve, depicted in Figure 8-2, illustrates the trend of the MSE values throughout the training. It demonstrates that the MSE gradually decreases as the number of training epochs increases, eventually reaching a point of plateauing. Notably, the gap between the MSE values of the training and validation sets remains minimal, indicating that the model performs well on the training data while still generalizing effectively to new data. Furthermore, the model's performance is evaluated on the test set, providing an evaluation score in the form of a test loss of 0.04 km^2

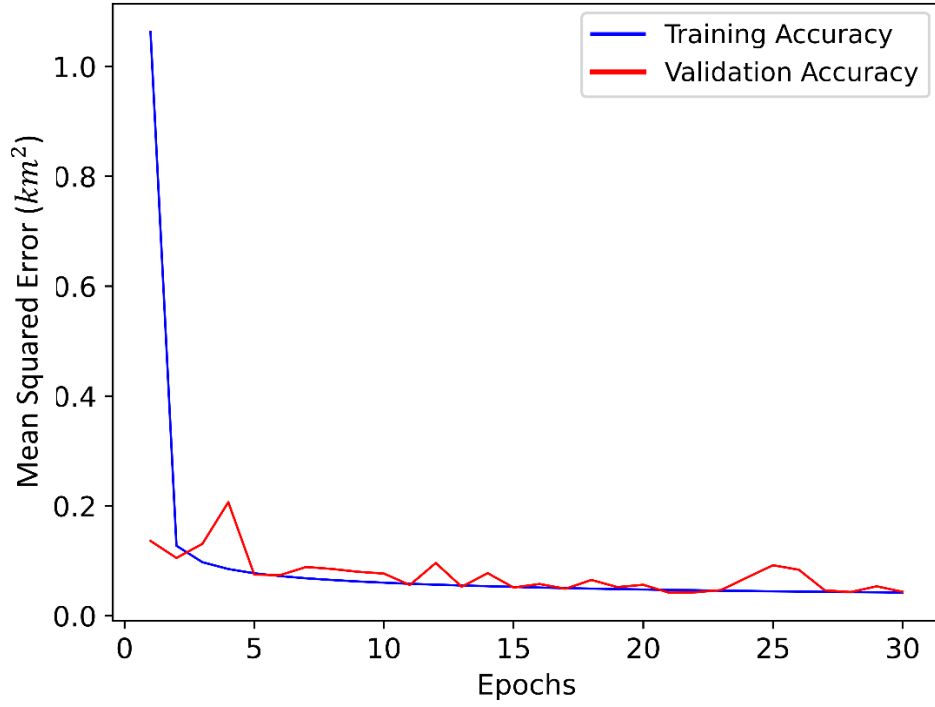


Figure 8-2: Plot of Training versus and validation accuracy against epochs.

This metric indicates the accuracy of the model's predictions on unseen data, highlighting its capability to effectively generalize beyond the training and validation sets. Overall, these evaluations demonstrate the reliable performance and generalization ability of the trained DNN model.

8.4 DNN Joint Inversion Model Evaluation

To assess the reliability and effectiveness of the trained DNN model in real-world scenarios, it needs to generalize well on unseen data. To evaluate how the DNN model can handle unseen examples, we have fed it with several synthetic joint gravity and magnetic anomalies to estimate the salts and basement structures. The corresponding average MSE value is obtained as 0.035 km^2 . Three examples are randomly selected and illustrated in Figure 8-3. The true synthetic salt and basement topography are plotted on top of the estimated subsurface with white dashed lines. A significant fit between true and estimated subsurface and their corresponding gravity and magnetic anomalies are observed.

Incorporating noise-added synthetic data into the model evaluation process can provide a more comprehensive assessment of the model's performance and robustness. Therefore, we evaluated the model against noise by adding % 5 and %10 Gaussian noise to unseen synthetic

gravity-magnetic anomalies with obtained average MSE values of 0.05 km^2 and 0.055 km^2 , respectively.

The results of model estimations on the noise-added data are illustrated in Figure 8-4 and Figure 8-5. As demonstrated the estimated subsurface fits the true one with reliable accuracy which proves the robustness of our DNN model against noise-contaminated data.

In the next section, the approved model is used to determine the salt and basement structures on real case data.

8.5 Results and Discussion

Gravity and magnetic anomalies are essential in hydrocarbon reservoir exploration to investigate the distribution of salts and basement structures. Salts formations, which exhibit lower densities compared to surrounding rocks, give rise to distinct negative gravity anomalies. Analyzing these anomalies allows for estimating the geometry of salt formations as major trapping mechanisms for hydrocarbons.

In hydrocarbon exploration, identifying basement structures is important due to their impact on hydrocarbon migration and accumulation. Basement rocks typically have higher densities and susceptibilities than overlying sedimentary rocks, resulting in observable anomalies in gravity and magnetic maps. Detecting the structure of the basement can be achieved through inversion of gravity or magnetic anomalies.

The composite variations in subsurface rock densities create challenges in delineating the positive gravity anomalies of the basement from the negative effect of salts. A promising practice is to combine gravity and magnetic anomalies to provide a more comprehensive understanding of subsurface geology. Gravity anomalies reflect density variations in both salts and the basement, while magnetic anomalies are influenced by susceptibility variations of the basement. Consequently, simultaneous interpretation of gravity and magnetic anomalies enhances salts and basement delineation required to map the distribution of hydrocarbon traps.

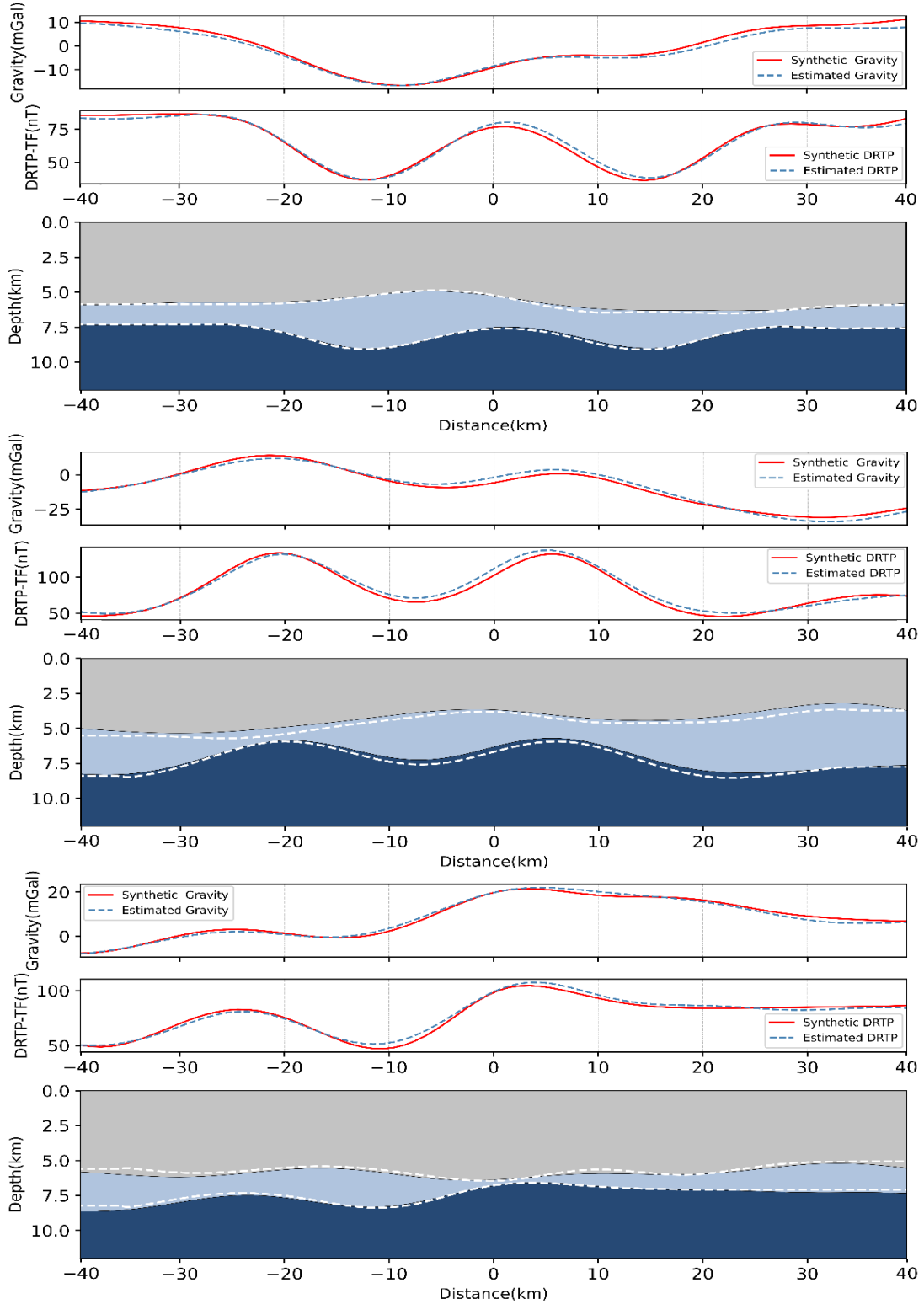


Figure 8-3: Samples of DNN model prediction results. The red curve represents the synthetic gravity and DRTP anomalies fed into the DNN model. The dashed blue curve represents the estimated gravity and magnetic anomalies of the predicted subsurface structure. The predicted subsurface structure is depicted with gray, light blue, and dark blue colors, corresponding to sediments, salts, and basement layers, respectively. The white dashed curves represent actual salt and basement topography.

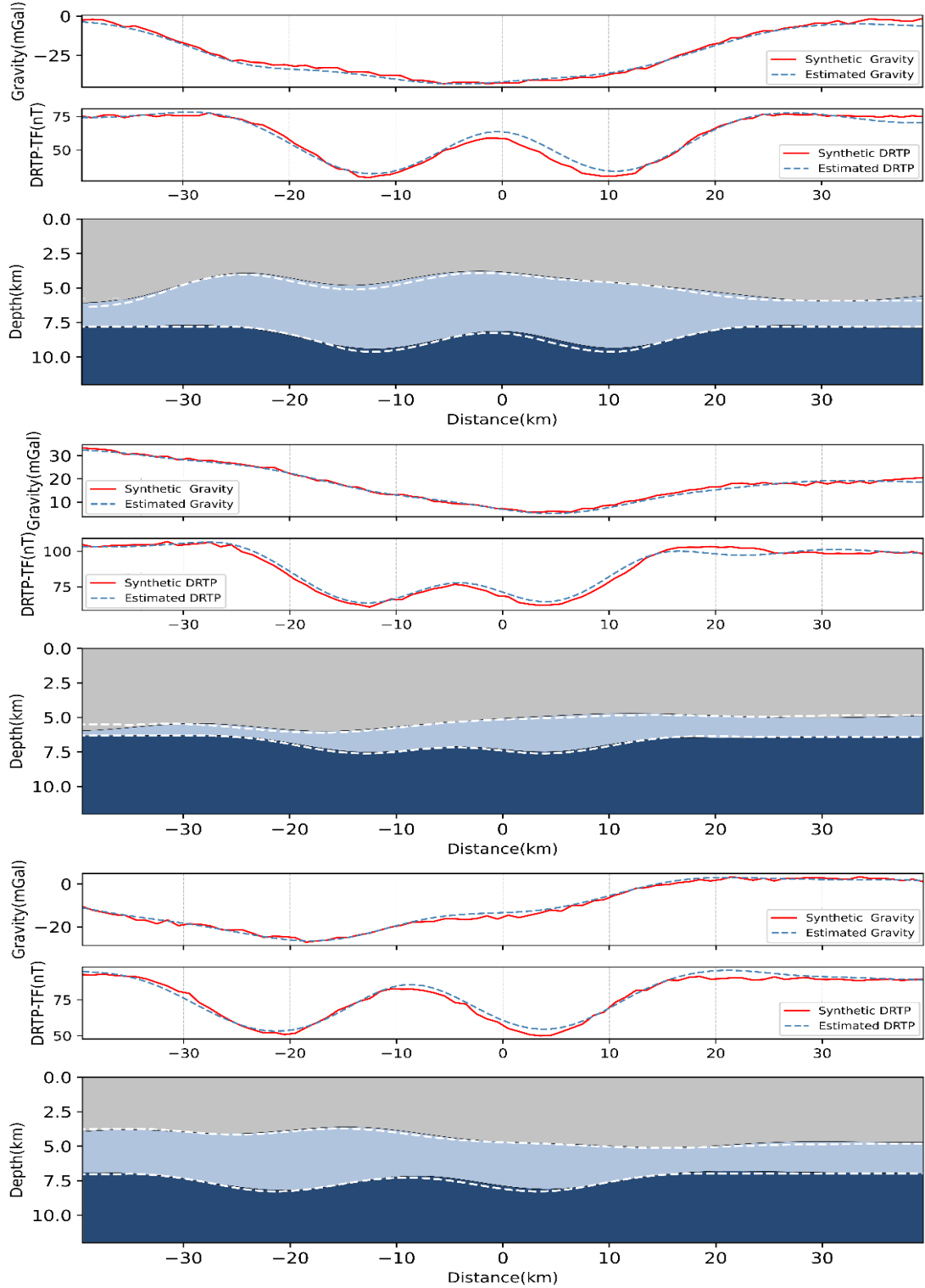


Figure 8-4: Samples of DNN model prediction results. The red curve represents the 5% Gaussian noise-added synthetic gravity and DRTP anomalies fed into the DNN model. The dashed blue curve represents the estimated gravity and magnetic anomalies of the predicted subsurface structure. The predicted subsurface structure is depicted with gray, light blue, and dark blue colors, corresponding to sediments, salts, and basement layers, respectively. The white dashed curves represent true actual salt and basement topography.

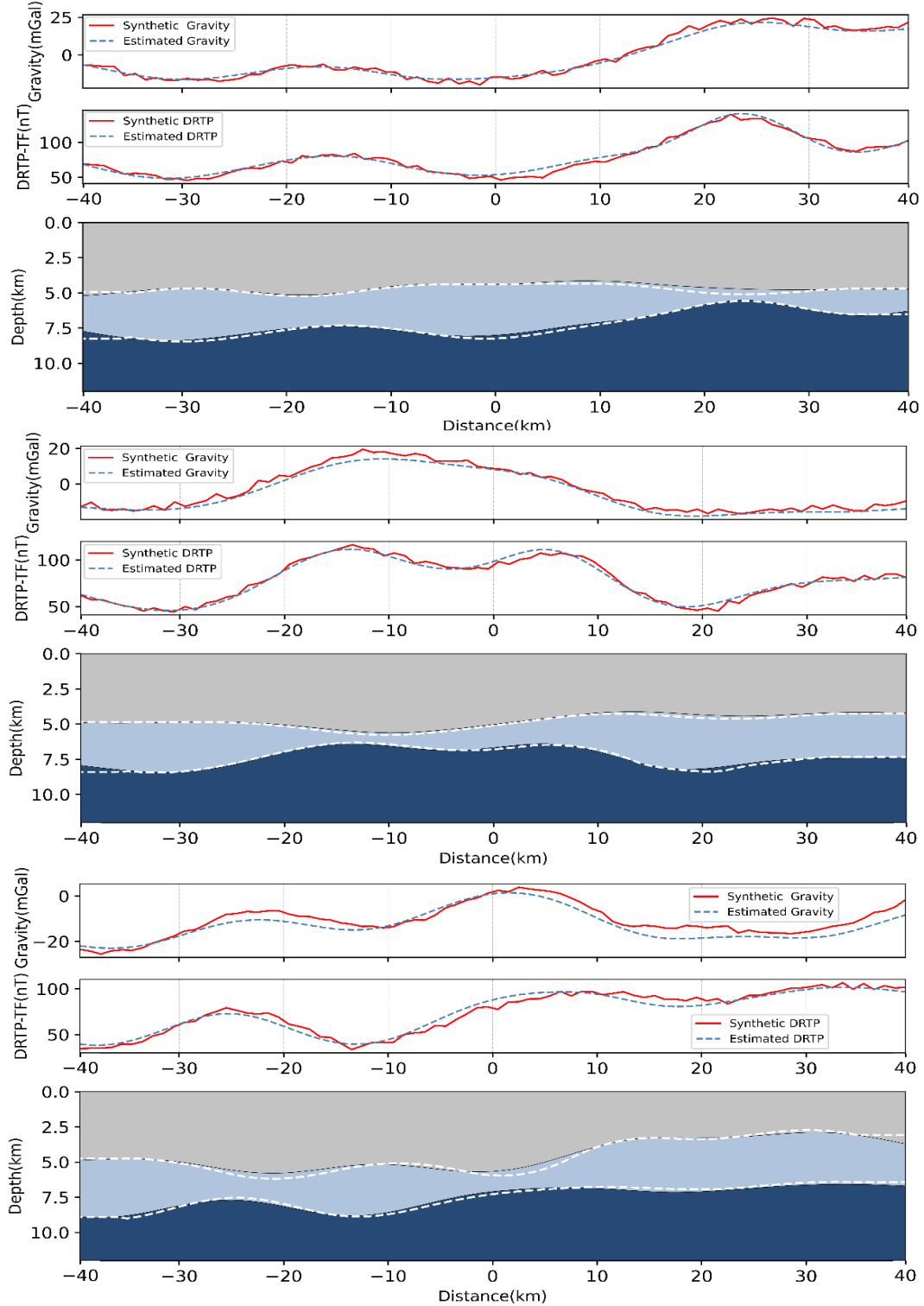


Figure 8-5: Samples of DNN model prediction results. The red curve represents the 10% Gaussian noise-added synthetic gravity and DRTP anomalies fed into the DNN model. The dashed blue curve represents the estimated gravity and magnetic anomalies of the predicted subsurface structure. The predicted subsurface structure is depicted with gray, light blue, and dark blue colors, corresponding to sediments, salts, and basement layers, respectively. The white dashed curves represent true actual salt and basement topography.

The DNN joint inversion model is applied to three profiles of airborne gravity and aeromagnetic anomalies to estimate salts and basement structures offshore UAE (Figure 8-6). Profiles are chosen to intersect the giant hydrocarbon fields of the region with significant gravity and magnetic anomalies.

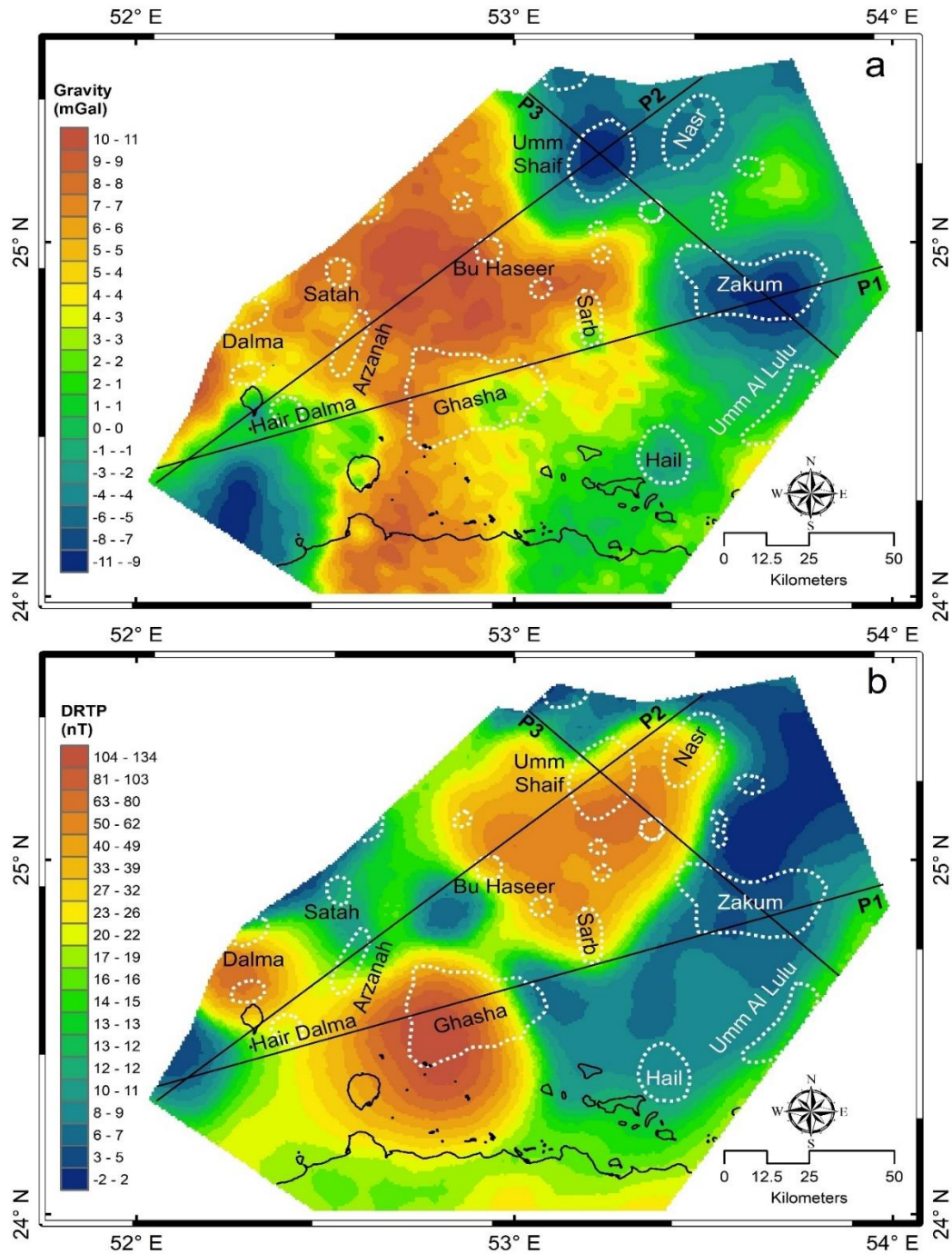


Figure 8-6: (a) Bouguer gravity anomaly; (b) reduced-to-pole magnetic (DRTP) anomaly. The dotted white enclosures illustrate the boundaries of oilfields. Profiles P1, P2, and P3 are used for the DNN joint inversion modeling.

Profile 1 extends from southwest to east and passes through the largest hydrocarbon fields of the region, Ghasha, and Zakum. Starting from the southwest and progressing towards the northeast, Profile 2 encompasses several significant locations in the studied region. It passes in proximity to Dalma and Hair Dalma, then proceeds to traverse Arzanah and Bu Haseer fields, ultimately reaching the Umm Shaif fields and Naser at the northeastern end of the profile. Profile 3 serves as a control profile that bisects Umm Shaif at the northwest and Zakum at the southeast.

The results of the joint interpretation of the gravity and magnetic anomalies over the profiles are presented in Figures 8-7 to Figure 8-10. The lowest gravity anomalies exhibit along Zakum and Umm Shaif. On the other hand, the magnetic anomaly map illustrates a high over the Umm Shaif field and a low at Zakum. Around Ghasha, both gravity and magnetic indicate high anomalies.

The results indicate variations in the depth of the basement across different areas. Over Ghasha, the shallowest basement is estimated at around 6.7 km . In contrast, the deepest basement is observed below the Zakum region ranging from $\sim 9.3\text{ km}$ to $\sim 9.7\text{ km}$. Moreover, another basement low is identified at $\sim 9.3\text{ km}$ in the southwest of the region. Across Profile 2, from Bu Haseer to Umm Shaif, the basement gradually rises to reach a maximum of 7.4 km . Moving to the north, around the Umm Shaif field, the average basement is estimated at $\sim 8\text{ km}$.

The analysis of the gravity and magnetic profiles provides insights into the thickness of the salt layers in the study region. The results reveal variations in the depth to the top of the salt layer across different areas. The shallowest depth to the salts occurs around the Umm Shaif field at $\sim 5.6\text{ km}$. In the Ghasha region, the depth to the salts is estimated to be approximately 6 km . Toward the northeast, the salts get deeper with the top of the salts ranging $\sim 7\text{ km}$ to $\sim 8\text{ km}$ over Zakum.

The salt thickness also shows variations across the study region. At the southwestern part where Profile 1 and Profile 2 intersect, the salt thickness ranges from 0.7 km to 1.7 km . The salt thickness gradually decreases between Arzanah and Bu Haseer fields, reaching a minimum value of 0.6 km . Continuing toward the north, the maximum salt thickness of 2.3 km is observed over the Umm Shaif field. As we progress toward the northeast and east, salt thickness reaches another high around Zakum ranging from $\sim 1.5\text{ km}$ to $\sim 1.9\text{ km}$.

The results of the DNN inversion of gravity and magnetic anomalies are in good agreement with other studies conducted in the region.

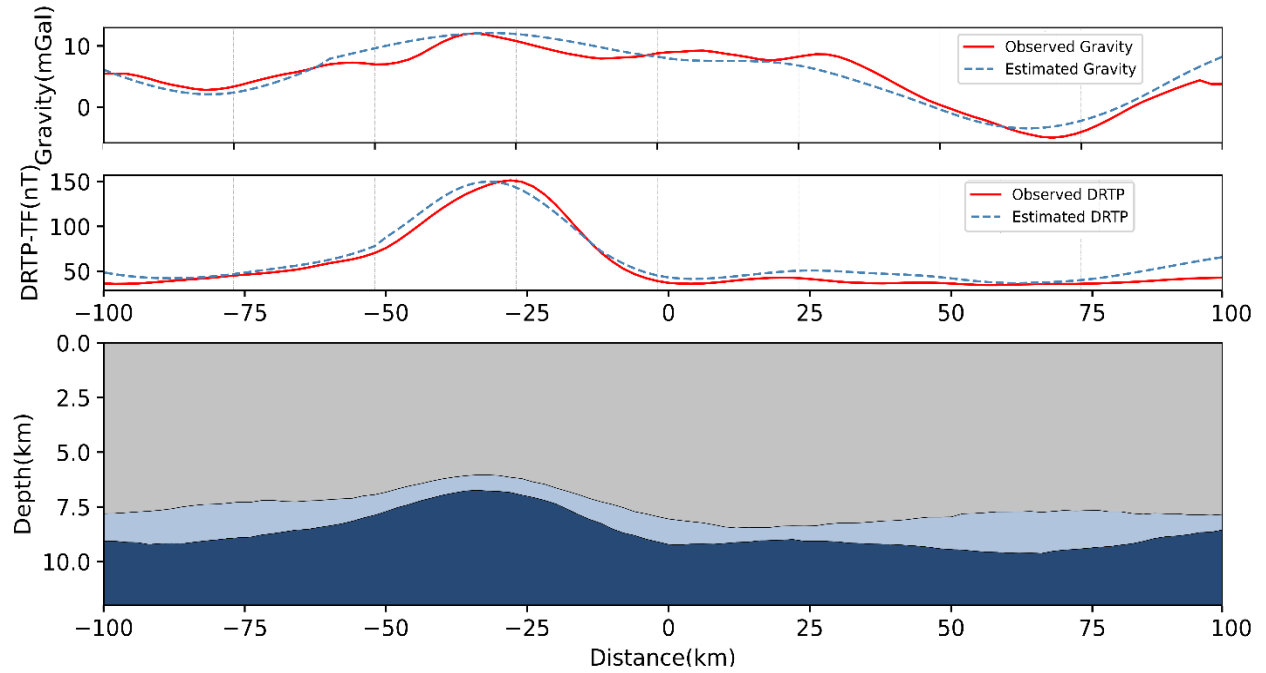


Figure 8-7: Results of the DNN joint inversion model prediction across Profile 1. Sediments, salts, and basement are illustrated with gray, light blue, and dark blue colors, respectively.

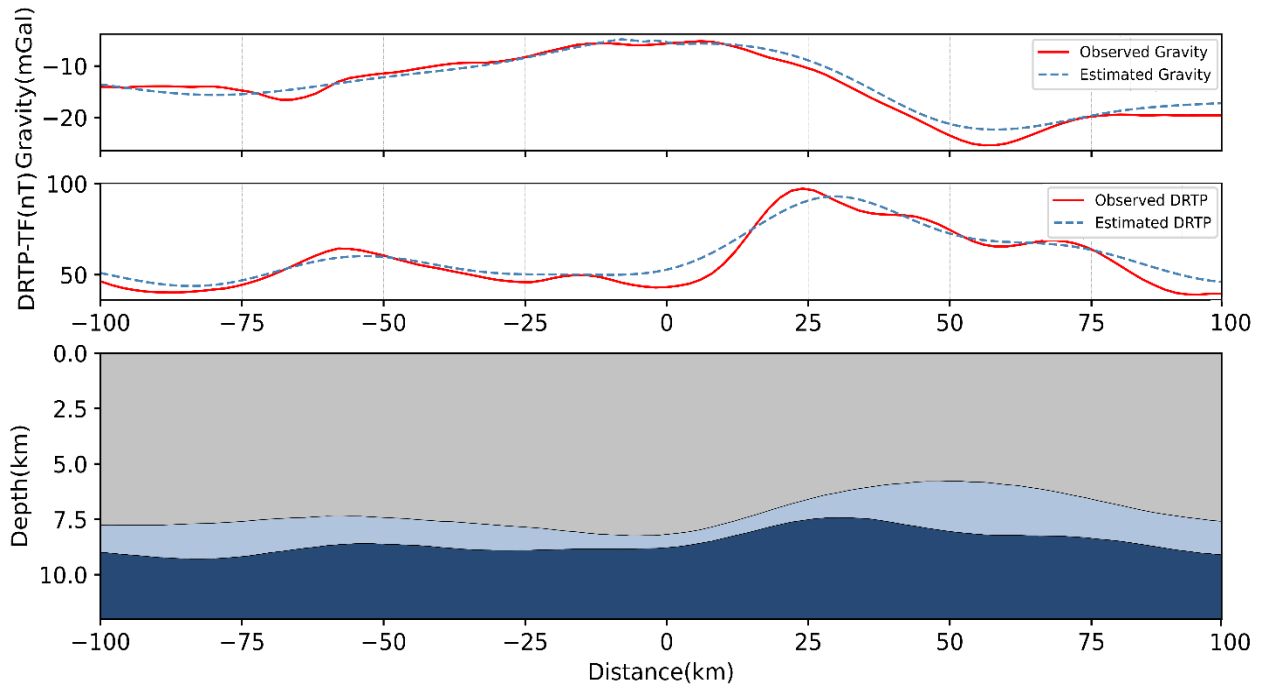


Figure 8-8: Results of the DNN joint inversion model prediction across Profile 2. Sediments, salts, and basement are illustrated with gray, light blue, and dark blue colors, respectively.

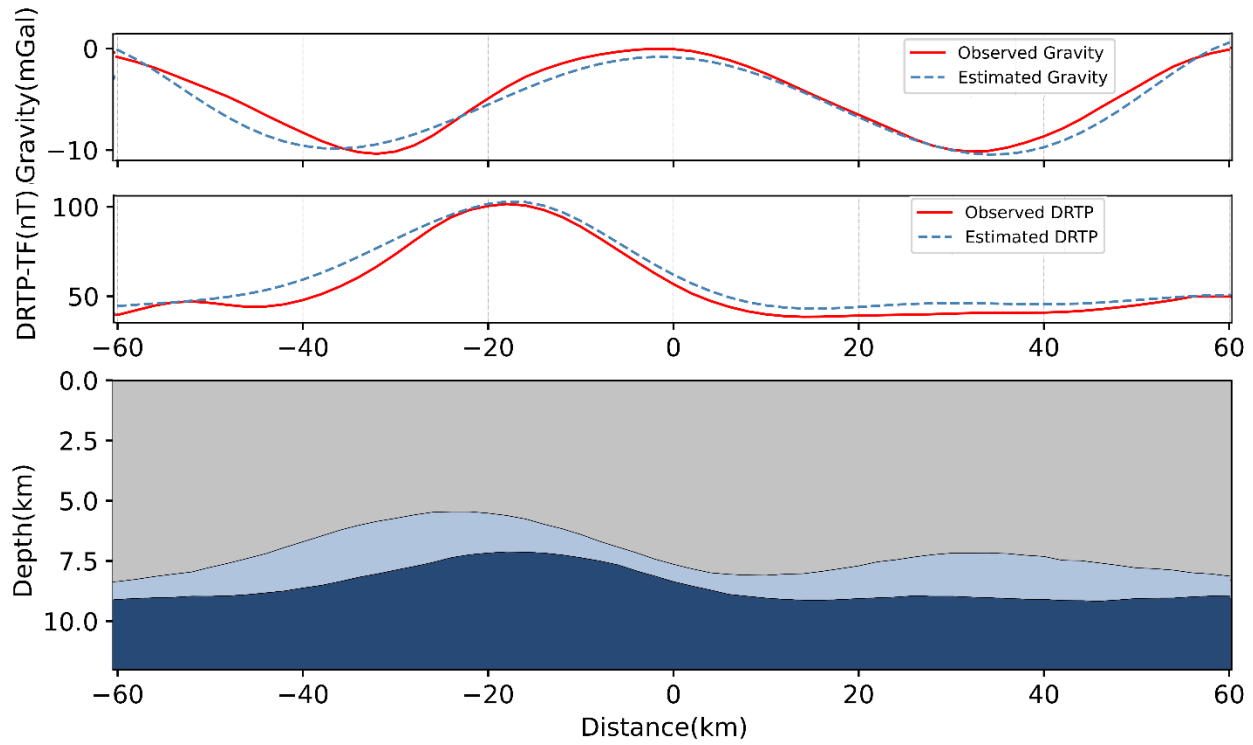


Figure 8-9: Results of the DNN joint inversion model prediction across Profile 3. Sediments, salts, and basement are illustrated with gray, light blue, and dark blue colors, respectively.

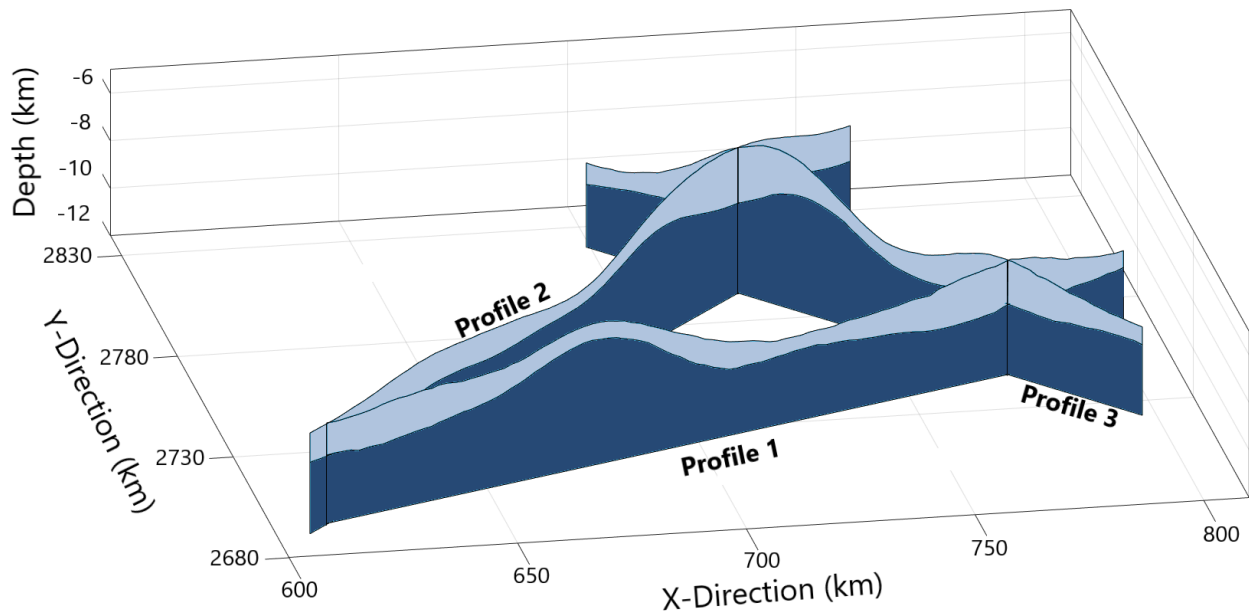


Figure 8-10: Representation of the 3 profiles, profile 1, profile 2, and profile 3.

To facilitate a better comparison between the results obtained from magnetic inversion and joint inversion of gravity and magnetic anomalies, the basement topography variations along the

three profiles are illustrated in Figure 8-11, Figure 8-12, and Figure 8-13. It can be observed that the topography estimated by both magnetic inversion and joint inversion exhibits a general agreement across all the profiles. The overall trends and patterns in the basement topography are consistent between the two techniques, indicating a reasonable correlation.

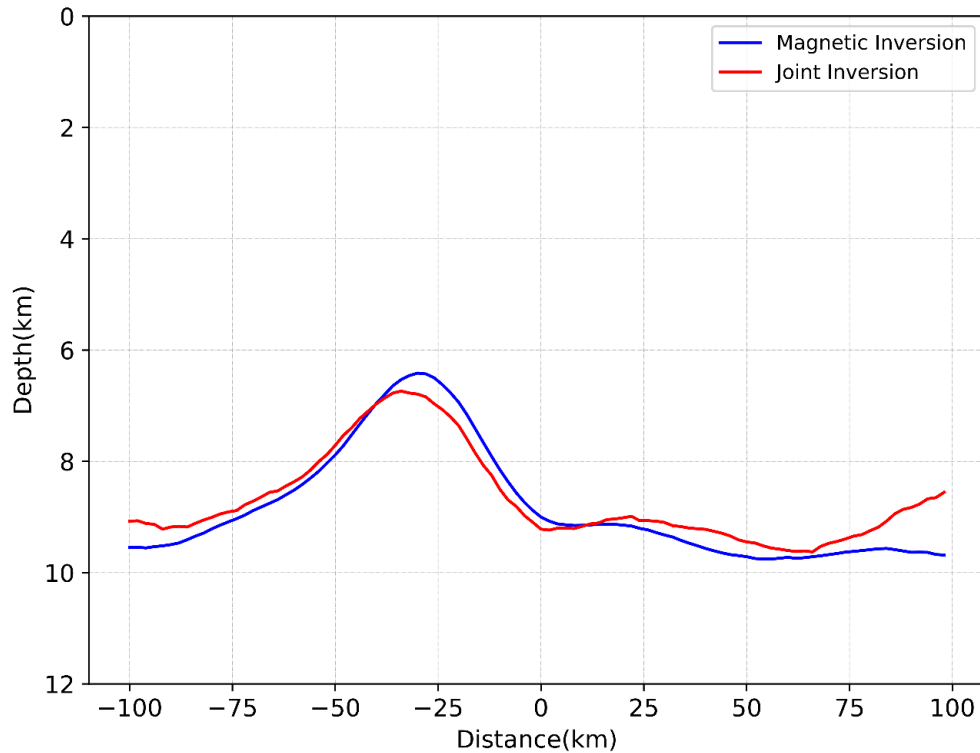


Figure 8-11: Basement topography estimation from magnetic inversion and joint gravity and magnetic inversion over Profile 1.

However, in the case of Profile 1, a slight discrepancy of approximately 300 meters is evident in the topography variation over the Ghasha region. Additionally, toward the end of the profile and below Zakum, there is a noticeable deviation between the joint inversion estimation and the magnetic inversion results. This discrepancy could be attributed to the presence of edge effects or the inherent complexity arising from the joint inversion method.

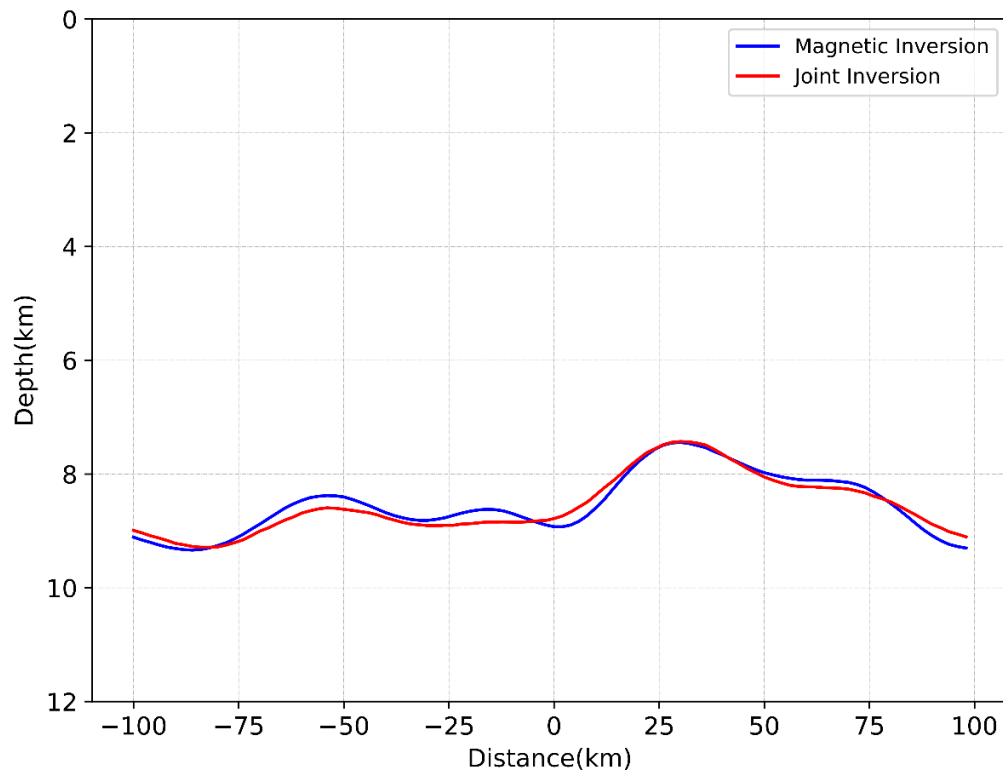


Figure 8-12: Basement topography estimation from magnetic inversion and joint gravity and magnetic inversion over Profile 2.

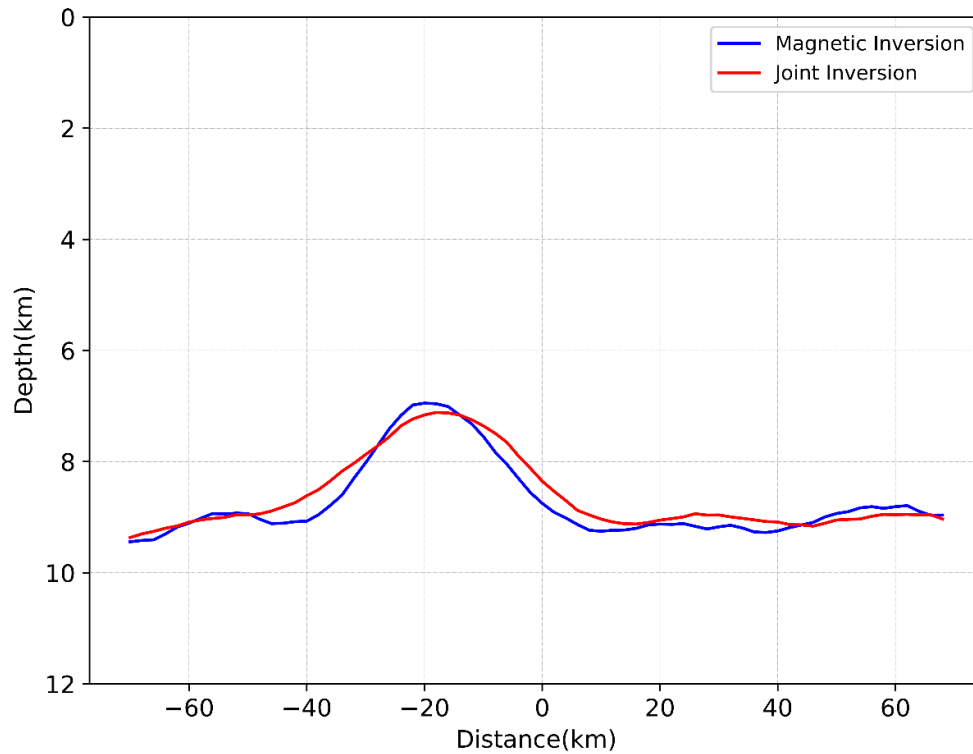


Figure 8-13: Basement topography estimation from magnetic inversion and joint gravity and magnetic inversion over Profile 3.

8.6 Conclusion

Joint inversion of gravity and magnetic anomalies using DNN was conducted to estimate the salt and basement structures in offshore UAE. The training dataset is a combination of gravity and magnetic datasets used to train a DNN model conducting nonlinear mapping of gravity and magnetic anomaly to salts and basement structures. The model performance on the unseen actual and noise-added synthetic anomalies demonstrated a significant fit between the predicted and simulated data even after adding 10% noise to the gravity and magnetic anomalies.

The analysis of the gravity and magnetic data provides valuable insights into the basement topography and salt thickness in offshore UAE. The basement topography ranges between 6.7 km to 9.7 km with the shallowest part located below the Ghasha hydrocarbon reservoir. The results also demonstrate that the deepest part of the basement appears toward the northeast and east of the region below Zakum.

The salt thickness also shows variations across the study region. In the southwestern part, the salt thickness ranges from 0.7 km to 1.7 km. It decreases between Arzanah and Bu Haseer fields, reaching a minimum value of 0.6 km. Continuing toward the north, the maximum salt thickness of 2.3 km is observed over the Umm Shaif field. As we progress toward the northeast and east of the study region, salt thickness reaches another high around Zakum ranging from ~ 1.5 km to ~1.9 km.

Chapter Nine: Conclusion and Recommendations for Future Studies

9.1 Conclusion

This thesis introduced a novel technique for inversion of gravity and magnetic anomalies to model subsurface structures. By integration of gravity and magnetic anomalies, the inherent non-uniqueness problem of geophysical inversions has been effectively addressed. Targeting the nonlinear inverse problem, DNN has efficiently mapped gravity and magnetic anomalies to subsurface models. The large training dataset required to train the DNN model is simulated through a novel technique. Correspondingly, using multi-processing algorithms, thousands of training examples are simulated comprising gravity and magnetic anomalies as input features and depth-to-salt and depth-to-basement as labels.

The application of the proposed techniques has been demonstrated to investigate salts and basement structures offshore UAE. In chapter six, the DNN gravity inversion is conducted to estimate the basement topography over the Ghasha region. The results obtained from analyzing three pseudo-gravity profiles demonstrated the range of basement topography to be between 7.4 km to 9.3 km.

The DNN inversion of magnetic anomalies is implemented in chapter seven. The results of the basement topography estimations over three profiles revealed the deepest basement below Zakum between ~ 9.45 km to ~ 9.75 km. Additionally, the basement topography shows a maximum over Ghasha at ~ 6.4 km.

In chapter eight, the focus shifted to the joint inversion of gravity and magnetic anomalies to estimate the salts and basement structures over the same profiles examined in the magnetic inversion. The results obtained from the joint inversion provide further insights into the salts and basement geology of the study area. It was determined that the shallowest basement depth observes over the Ghasha region, measuring approximately ~ 6.7 km. On the other hand, the deepest basement depth was found beneath Zakum, with a range between ~ 9.35 km to ~ 9.65 km. Depth to the top of the salts and basement over Umm Shaif was estimated to be ~ 5.6 km and ~ 8 km, respectively. Moreover, the top of the salts over the giant hydrocarbon reservoirs of Ghasha and Zakum was identified to reach ~ 6 km and ~ 8.45 km.

The results of the DNN inversion of gravity and magnetic anomalies are in good agreement with other studies conducted in the region. Kabirzadeh et al. (2021) investigated the basement and Hormuz salt structures in the offshore UAE by joint analysis of gravity and magnetic anomalies. Their results showed the ranges of the basement depth of 6.9 km to 9.7 km and a significant variation of 200 m to 3 km in salt thickness. Ghalenoei et al. (2021) researched a joint inversion of gravity and magnetic data using a trans-dimensional model to study salt and basement structures of UAE. They estimated the depth to the top of the salt over the Ghasha field of ~ 5 km to ~7 km. The depth to the basement was estimated at 8.75 km to 9.35 km. Geng et al., 2020 implemented a 3-D constrained inversion of aerogravity and aeromagnetic anomalies in offshore Abu Dhabi. Their magnetic inversion over the entire region estimated a basement model with a depth range of 8 km to 10 km with two highs at 8 and 8.5 km highlighting possible magmatic bodies. Moreover, the depth to the top of Hormuz salt obtained from the 3-D inversion of residual gravity varied from 4.5 km to 8.5 km.

The discrepancy between our results and the other studies conducted in the region could arise from several factors:

- **Methodology:** Each study may employ different methodologies, techniques, and algorithms for the inversion of geopotential anomalies. Variations in the inversion methods, model assumptions, and parameter choices can lead to differences in the resulting subsurface models.
- **Model Complexity:** The complexity of the subsurface models considered in the inversion can also affect the results. Different studies may have different assumptions and constraints regarding the subsurface structures, including the number of layers, geometry, and physical properties considered. These differences can lead to variations in the estimated depths and thicknesses of the salt and basement structures.
- **Noise and Uncertainties:** The presence of noise in the data and uncertainties in the inversion process can also contribute to differences in the results. The accuracy of the data preprocessing, noise filtering techniques, and inversion regularization methods can influence the final estimates.

- Interpretation and Validation: Differences in the interpretation and validation of the results can also play a role. Studies may have different criteria for evaluating the goodness of fit or may focus on specific regions or features of interest, leading to variations in the reported results.

It is essential to carefully compare the methodologies, datasets, and assumptions used in your study with those of the other studies to identify the sources of the differences. Additionally, considering the uncertainties and limitations associated with geophysical inversions, it is crucial to assess the robustness and reliability of the results through further validation and comparison with other independent data or well data, if available.

ML techniques are a subset of artificial intelligence that involves training models on large datasets to make predictions or decisions without being explicitly programmed. These models can then be used to automate tasks, make predictions, classify data, etc. ML techniques are incredibly versatile and can be applied to a wide range of problems. As more data becomes available and computing power increases, we can expect to see even more innovative and impactful applications of ML.

The application of DNNs for geophysical inversion offers several advantages compared to conventional techniques. DNN has significantly contributed to solving the non-uniqueness and non-linearity aspects of our inverse problems. For instance, DNNs can capture the complex nonlinear relationship between geophysical data and subsurface models. Additionally, they can incorporate prior knowledge about subsurface structures, so to enhance the accuracy of the inversion results.

However, the quality and quantity of the training dataset have a significant impact on the accuracy and reliability of the inversion results. To obtain meaningful and accurate subsurface models, the simulated dataset must accurately represent the desired subsurface structure. When designing the forward models for data simulation, it is essential to consider the target characteristics of the subsurface. For instance, if the goal is to capture both short and long-wavelength variations in topography, the dimensions of the forward models should be appropriately configured to accommodate this requirement. This criterion is also affected by the distribution and resolution of the observed data. If data is collected over scattered locations, the chance of capturing short-wavelength anomalies is reduced. Therefore, the numbers and length

of anomalies of the forward model must be specified accordingly to account for the data coverage.

Implementing DNN inversion does have limitations when it comes to generalizing the trained models to different regions with varying dimensionality and geological properties. Models trained for a specific region may not be directly applicable to provide accurate interpretations for regions with different characteristics. Major modifications to the physical and structural parameters of a region may require re-training of the models to ensure reliable results.

Additionally, the process of dataset simulation and model training can be time-consuming. Nevertheless, leveraging high-level programming languages and utilizing modern computing resources can help optimize these processes and reduce the computational time required.

9.2 Recommendations for Future Studies

Geophysical inversion involves determining the subsurface properties of the earth by analyzing geophysical data. To do so, conventional inversion methodologies have relied on mathematical and physical concepts/formulations to interpret geophysical data. Such methods, however, can be time-consuming and computationally expensive, and require expert knowledge to implement.

In search of a solution to address the issues listed above, we came to notice and then affirmed throughout our research, the benefits of DNNs techniques for a new approach toward geophysical inversion. Briefly put, by learning patterns and relationships in large datasets, DNNs can often provide faster and more accurate results. The following points list some of the benefits of using DNNs for geophysical inversion:

- Enhanced speed and efficiency as capable of analyzing large volumes of geophysical data.
- Improved accuracy of inversion results as they can learn complex patterns and relationships in geophysical data.
- Higher flexibility and adaptability than conventional methods as better fitted for incorporating a variety of data layers and hypotheses.
- Less subjectivity to human biases and interpretations.
- Suitable for handling noisy geophysical data.
- Computationally cheaper than conventional methods; particularly for large-scale data.

Despite the promising advantages of using DNNs for geophysical inversion, certain challenges need to be further addressed:

- Inevitable need for more high-quality training data: This could involve either developing new simulation tools to generate synthetic data or collecting more high-quality field data. As promisingly tried by us, the development of simulation tools to generate synthetic data is worth further research regarding the variety of factors involved. Synthetic data is created by simulating geophysical measurements based on known geological models or properties. By accurately modeling the physics of the measurement process and incorporating as much realistic noise and uncertainty as possible, synthetic data becomes an encouraging source for controlled and repeatable training datasets. Synthetic datasets can be particularly useful where limited field data is available or when exploring different subsurface scenarios.
- 3D high-resolution models: Such models have the potential to provide detailed and realistic images of the subsurface; enabling a better understanding of geological structures. However, reconstructing such models sounds expensive in terms of computational resources and time. To address this challenge, futuristic techniques should focus on reducing the complexity of subsurface models while ensuring the essential characteristics of the subsurface are enclosed. One way to do so is to instead of representing every small-scale geological feature, have the models focused on capturing the dominant structural properties that significantly impact the subsurface behavior; thus, constructing a simplified representation that retains their essential characteristics.
- The need for interpretable models: In many cases, the end-users of geophysical inversion results require an understanding of the underlying physics and geology. By incorporating physical principles and geological information into the training process of machine learning algorithms, the resulting models can provide interpretable insights. Consequently, the models can leverage the interpretability of conventional geophysical inversion methods while benefiting from the predictive power of DNNs techniques.
- Integration of geophysical data: Geophysical data often come from a variety of sources differing in spatial, semantic, and temporal representation, absolute and

relative accuracy, horizontal and spatial references, format, metadata, and several other properties. Therefore, it can be challenging to efficiently combine data from different sensors, surveys, and practices. We suggest further research on mechanisms for integrating geophysical data with other sources of information such as geological maps and well data. Such research may focus on enhancing various aspects of data interoperability like the use of standardized data and metadata schemas, etc. By doing so, it would be possible to provide a more reliable understanding of the subsurface and improve the accuracy of interpretations.

In conclusion, geophysical inversion using DNNs techniques has shown the potential to revolutionize the field of geophysics. However, there are several challenges that need to be further addressed before this potential can be fully realized. The development of more interpretable models, more sophisticated yet standardized data integration methods, and more high-quality training data are among the areas of active research recommended by us.

References

- Al-Husseini, M.I., 2000. Origin of the Arabian Plate Structures: Amar Collision and Najd Rift. *GeoArabia* 5, 527–542. <https://doi.org/10.2113/geoarabia0504527>
- Ali, M.Y., Fairhead, J.D., Green, C.M., Noufal, A., 2017. Basement structure of the United Arab Emirates derived from an analysis of regional gravity and aeromagnetic database. *Tectonophysics* 712–713, 503–522. <https://doi.org/10.1016/j.tecto.2017.06.006>
- Ali, M.Y., Farid, A., 2016. Cretaceous – Neogene Structural Evolution of Se Abu Dhabi, United Arab Emirates. *J. Pet. Geol.* 39, 221–245. <https://doi.org/10.1111/jpg.12644>
- Ali, M.Y., Watts, A.B., 2009. Subsidence history, gravity anomalies and flexure of the United Arab Emirates (UAE) foreland basin. *GeoArabia* 14, 17–44. <https://doi.org/10.2113/geoarabia140217>
- Allen, P.A., 2007. The Huqf Supergroup of Oman: Basin development and context for Neoproterozoic glaciation. *Earth-Sci. Rev.* 84, 139–185. <https://doi.org/10.1016/j.earscirev.2007.06.005>
- Alsharhan, A.S., Salah, M.G., 1997. Tectonic implications of diapirism on hydrocarbon accumulation in the United Arab Emirates. *Bull. Can. Pet. Geol.* 45, 279–296.
- Ashena, Z., Kabirzadeh, H., Kim, J.W., Wang, X., Ali, M., 2023. A Novel 2.5D Deep Network Inversion of Gravity Anomalies to Estimate Basement Topography. *SPE Reserv. Eval. Eng.* 1–14. <https://doi.org/10.2118/211800-PA>
- Ashena, Z., Kabirzadeh, H., Wang, X., Lee, Y., Woo, I., Ali, M., Kim, J.W., 2022. DNN Inversion of Gravity Anomalies for Basement Topography Mapping. Presented at the ADIPEC, OnePetro. <https://doi.org/10.2118/211800-MS>
- Aster, R.C., Borchers, B., Thurber, C.H. (Eds.), 2019. Copyright, in: *Parameter Estimation and Inverse Problems (Third Edition)*. Elsevier, p. iv. <https://doi.org/10.1016/B978-0-12-804651-7.00003-1>
- B. Ashena, Z., E. Ardestani, V., G. Camacho, A., Dehghani, A., Fernández, J., 2018. Moho depth determination beneath the Zagros Mountains from 3D inversion of gravity data. *Arab. J. Geosci.* 11, 52. <https://doi.org/10.1007/s12517-018-3385-x>
- B. Ashena, Z., Kabirzadeh, H., Wang, X., Ali, M., Lee, G.H., Woo, I., Kim, J.W., 2019. Unsupervised Learning Analysis of a Multi-Parameter Geophysical Database for Abu Dhabi Hydrocarbon Reservoirs. Presented at the Abu Dhabi International Petroleum Exhibition & Conference, OnePetro. <https://doi.org/10.2118/197140-MS>
- Bear, G.W., Al-Shukri, H.J., Rudman, A.J., 1995. Linear inversion of gravity data for 3-D density distributions. *Geophysics* 60, 1354–1364. <https://doi.org/10.1190/1.1443871>
- Bengio, Y., Grandvalet, Y., 2003. No unbiased estimator of the variance of K-fold cross-validation, in: *Proceedings of the 16th International Conference on Neural Information Processing Systems, NIPS'03*. MIT Press, Cambridge, MA, USA, pp. 513–520.
- Blakely, R.J., 1995. *Potential Theory in Gravity and Magnetic Applications*. Cambridge University Press, Cambridge. <https://doi.org/10.1017/CBO9780511549816>

Boschetti, F., Dentith, M.C., List, R.D., 1996. Inversion of seismic refraction data using genetic algorithms. *Geophysics* 61, 1715–1727. <https://doi.org/10.1190/1.1444089>

Boullanger, O., Chouteau, M., 2001. Constraints in 3D gravity inversion. *Geophys. Prospect.* 49, 265–280. <https://doi.org/10.1046/j.1365-2478.2001.00254.x>

Bowring, S.A., Grotzinger, J.P., Condon, D.J., Ramezani, J., Newall, M.J., Allen, P.A., 2007. Geochronologic constraints on the chronostratigraphic framework of the Neoproterozoic Huqf Supergroup, Sultanate of Oman. *Am. J. Sci.* 307, 1097–1145. <https://doi.org/10.2475/10.2007.01>

Calderón-Macías, C., Sen, M., Stoffa, P., 2001. Artificial neural networks for parameter estimation in geophysics. *Geophys. Prospect.* 48, 21–47. <https://doi.org/10.1046/j.1365-2478.2000.00171.x>

Camacho, A.G., Montesinos, F.G., Vieira, R., 2002. A 3-D gravity inversion tool based on exploration of model possibilities. *Comput. Geosci.* 28, 191–204. [https://doi.org/10.1016/S0098-3004\(01\)00039-5](https://doi.org/10.1016/S0098-3004(01)00039-5)

Camacho, A.G., Montesinos, F.G., Vieira, R., 1999. Gravity inversion by means of growing bodies. *Geophysics* 65, 95–101. <https://doi.org/10.1190/1.1444729>

Carrillo, J., Perez-Flores, M.A., Gallardo, L.A., Schill, E., 2022. Joint inversion of gravity and magnetic data using correspondence maps with application to geothermal fields. *Geophys. J. Int.* 228, 1621–1636. <https://doi.org/10.1093/gji/ggab416>

Cella, F., Fedi, M., 2012. Inversion of potential field data using the structural index as weighting function rate decay. *Geophys. Prospect.* 60, 313–336. <https://doi.org/10.1111/j.1365-2478.2011.00974.x>

Chen, Y., 2020. Automatic microseismic event picking via unsupervised machine learning. *Geophys. J. Int.* 222, 1750–1764. <https://doi.org/10.1093/gji/ggaa186>

Chollet, F., 2021. *Deep Learning with Python*, Second Edition. Simon and Schuster.

Chunduru, R.K., Sen, M.K., Stoffa, P.L., 1997. Hybrid optimization methods for geophysical inversion. *GEOPHYSICS* 62, 1196–1207. <https://doi.org/10.1190/1.1444220>

Coléou, T., Poupon, M., Azbel, K., 2003. Unsupervised seismic facies classification: A review and comparison of techniques and implementation. *Lead. Edge* 22, 942–953. <https://doi.org/10.1190/1.1623635>

Constable, S.C., Parker, R.L., Constable, C.G., 1987. Occam's inversion: A practical algorithm for generating smooth models from electromagnetic sounding data. *GEOPHYSICS* 52, 289–300. <https://doi.org/10.1190/1.1442303>

Das, S., Chen, X., Hobson, M.P., Phadke, S., van Beest, B., Goudswaard, J., Hohl, D., 2018. Surrogate regression modelling for fast seismogram generation and detection of microseismic events in heterogeneous velocity models. *Geophys. J. Int.* 215, 1257–1290. <https://doi.org/10.1093/gji/ggy283>

Devilee, R.J.R., Curtis, A., Roy-Chowdhury, K., 1999. An efficient, probabilistic neural network approach to solving inverse problems: Inverting surface wave velocities for Eurasian crustal thickness. *J. Geophys. Res. Solid Earth* 104, 28841–28857. <https://doi.org/10.1029/1999JB900273>

- Di, H., Shafiq, M., AlRegib, G., 2018. Multi-attribute k-means clustering for salt-boundary delineation from three-dimensional seismic data. *Geophys. J. Int.* 215, 1999–2007. <https://doi.org/10.1093/gji/ggy376>
- Farrell, S.M., Jessell, M.W., Barr, T.D., 1996. Inversion of geological and geophysical data sets using genetic algorithms, in: SEG Technical Program Expanded Abstracts 1996, SEG Technical Program Expanded Abstracts. Society of Exploration Geophysicists, pp. 1404–1406. <https://doi.org/10.1190/1.1826374>
- Fernández-Martínez, J.L., Pallero, J.L.G., Fernández-Muñiz, Z., Pedruelo-González, L.M., 2014. The effect of noise and Tikhonov's regularization in inverse problems. Part I: The linear case. *J. Appl. Geophys.* 108, 176–185. <https://doi.org/10.1016/j.jappgeo.2014.05.006>
- Florio, G., Lo Re, D., 2018. Terracing of potential fields by clustering methods. *Geophysics* 83, G47–G58. <https://doi.org/10.1190/geo2017-0140.1>
- Fregoso, E., Palafox, A., Moreles, M.A., 2020. Initializing Cross-Gradients Joint Inversion of Gravity and Magnetic Data with a Bayesian Surrogate Gravity Model. *Pure Appl. Geophys.* 177, 1029–1041. <https://doi.org/10.1007/s00024-019-02334-w>
- Gallardo, L.A., Meju, M.A., 2007. Joint two-dimensional cross-gradient imaging of magnetotelluric and seismic traveltime data for structural and lithological classification. *Geophys. J. Int.* 169, 1261–1272. <https://doi.org/10.1111/j.1365-246X.2007.03366.x>
- Geng, M., Ali, M.Y., Fairhead, J.D., Bouzidi, Y., Barkat, B., 2020. Morphology of the basement and Hormuz salt distribution in offshore Abu Dhabi from constrained 3-D inversion of gravity and magnetic data. *Tectonophysics* 791, 228563. <https://doi.org/10.1016/j.tecto.2020.228563>
- Géron, A., 2019. Hands-On Machine Learning with Scikit-Learn, Keras, and TensorFlow: Concepts, Tools, and Techniques to Build Intelligent Systems. O'Reilly Media, Inc.
- Ghalenoei, E., Dettmer, J., Ali, M.Y., Kim, J.W., 2022. Trans-dimensional gravity and magnetic joint inversion for 3-D earth models. *Geophys. J. Int.* 230, 363–376.
- Glorot, X., Bordes, A., Bengio, Y., 2011. Deep Sparse Rectifier Neural Networks, in: Proceedings of the Fourteenth International Conference on Artificial Intelligence and Statistics. Presented at the Proceedings of the Fourteenth International Conference on Artificial Intelligence and Statistics, JMLR Workshop and Conference Proceedings, pp. 315–323.
- Goodfellow, I., Bengio, Y., Courville, A., 2016. Deep Learning. MIT Press.
- Grana, D., 2020. Bayesian petroelastic inversion with multiple prior models. *Geophysics* 85, M57–M71. <https://doi.org/10.1190/geo2019-0625.1>
- Gross, L., 2019. Weighted cross-gradient function for joint inversion with the application to regional 3-D gravity and magnetic anomalies. *Geophys. J. Int.* 217, 2035–2046. <https://doi.org/10.1093/gji/ggz134>

Guillemoteau, J., Vignoli, G., Barreto, J., Sauvin, G., 2022. Sparse laterally constrained inversion of surface-wave dispersion curves via minimum gradient support regularization. *Geophysics* 87, R281–R289. <https://doi.org/10.1190/geo2021-0247.1>

Guo, J., Li, Y., Jessell, M., Giraud, J., Li, C., Wu, L., Li, F., Liu, S., 2021. 3D geological structure inversion from Noddy-generated magnetic data using deep learning methods. *Comput. Geosci.* 149, 104701. <https://doi.org/10.1016/j.cageo.2021.104701>

Haber, E., Oldenburg, D., 1997. Joint inversion: a structural approach. *Inverse Probl.* 13, 63. <https://doi.org/10.1088/0266-5611/13/1/006>

Hodgson, R.A., 1965. Genetic and Geometric Relations Between Structures in Basement and Overlying Sedimentary Rocks, with Examples from Colorado Plateau and Wyoming1. *AAPG Bull.* 49, 935–949. <https://doi.org/10.1306/A6633684-16C0-11D7-8645000102C1865D>

Hu, Z., Liu, S., Hu, X., Fu, L., Qu, J., Wang, H., Cheng, Q., 2021. Inversion of magnetic data using deep neural networks. *Phys. Earth Planet. Inter.* 311, 106653. <https://doi.org/10.1016/j.pepi.2021.106653>

Huang, R., Liu, S., Qi, R., Zhang, Y., 2021. Deep Learning 3D Sparse Inversion of Gravity Data. *J. Geophys. Res. Solid Earth* 126, e2021JB022476. <https://doi.org/10.1029/2021JB022476>

Hudec, M.R., Jackson, M.P.A., 2007. Terra infirma: Understanding salt tectonics. *Earth-Sci. Rev.* 82, 1.

Ioffe, S., Szegedy, C., 2015. Batch Normalization: Accelerating Deep Network Training by Reducing Internal Covariate Shift. <https://doi.org/10.48550/arXiv.1502.03167>

Izquierdo, K., Lekić, V., Montési, L.G.J., 2020. A Bayesian approach to infer interior mass anomalies from the gravity data of celestial bodies. *Geophys. J. Int.* 220, 1687–1699. <https://doi.org/10.1093/gji/ggz544>

Kabirzadeh, H., Ali, M.Y., Lee, G.H., Kim, J.W., 2021. Determining infracambrian Hormuz salt and basement structures offshore Abu Dhabi by joint analysis of gravity and magnetic anomalies. *SPE Reserv. Eval. Eng.* 24, 238–249.

Klemelä, J.S., 2009. Smoothing of Multivariate Data: Density Estimation and Visualization. John Wiley & Sons.

Last, B.J., Kubik, K., 1983. Compact gravity inversion. *GEOPHYSICS* 48, 713–721. <https://doi.org/10.1190/1.1441501>

Li, Y., Jia, Z., Lu, W., 2022. Self-Supervised Deep Learning for 3D Gravity Inversion. *IEEE Trans. Geosci. Remote Sens.* 60, 1–11. <https://doi.org/10.1109/TGRS.2022.3225449>

Li, Y., Oldenburg, D.W., 1998. 3-D inversion of gravity data. *GEOPHYSICS* 63, 109–119. <https://doi.org/10.1190/1.1444302>

Li, Y., Oldenburg, D.W., 1996. 3-D inversion of magnetic data. *GEOPHYSICS* 61, 394–408. <https://doi.org/10.1190/1.1443968>

Lin, W., Zhdanov, M.S., 2018. Joint multinary inversion of gravity and magnetic data using Gramian constraints. *Geophys. J. Int.* 215, 1540–1557. <https://doi.org/10.1093/gji/ggy351>

Lines, L. r., TreiTEL, S., 1984. A Review of Least-Squares Inversion and Its Application to Geophysical Problems*. *Geophys. Prospect.* 32, 159–186. <https://doi.org/10.1111/j.1365-2478.1984.tb00726.x>

MacQueen, J., 1965. Some methods for classification and analysis of multivariate observations, in: *Proc. 5th Berkeley Symposium on Math., Stat., and Prob.* p. 281.

Meier, U., Curtis, A., Trampert, J., 2007. Global crustal thickness from neural network inversion of surface wave data. *Geophys. J. Int.* 169, 706–722. <https://doi.org/10.1111/j.1365-246X.2007.03373.x>

Melo, A., Li, Y., 2016. Geological characterization applying k-means clustering to 3D magnetic, gravity gradient, and DC resistivity inversions: A case study at an iron oxide copper gold (IOCG) deposit. Presented at the 2016 SEG International Exposition and Annual Meeting, OnePetro.

Menke, W., 2018. *Geophysical Data Analysis: Discrete Inverse Theory*. Academic Press.

Mercolli, I., Briner, A.P., Frei, R., Schönberg, R., Nägler, T.F., Kramers, J., Peters, T., 2006. Lithostratigraphy and geochronology of the Neoproterozoic crystalline basement of Salalah, Dhofar, Sultanate of Oman. *Precambrian Res.* 145, 182–206. <https://doi.org/10.1016/j.precamres.2005.12.002>

Moghadas, D., 2020. One-dimensional deep learning inversion of electromagnetic induction data using convolutional neural network. *Geophys. J. Int.* 222, 247–259. <https://doi.org/10.1093/gji/ggaa161>

Nehlig, P., Genna, A., Asfirane, F., BRGM, F., Guerrot, C., Eberlé, J.M., Kluyver, H.M., Lasserre, J.L., Le Goff, E., Nicol, N., BRGM, F., Salpeteur, N., Shanti, M., Thiéblemont, D., Truffert, C., BRGM, F., 2002. A review of the Pan-African evolution of the Arabian Shield. *GeoArabia* 7, 103–124. <https://doi.org/10.2113/geoarabia0701103>

Obaid, K., Neves, F., Mahgoub, M., Taher, A., Noufal, A., Matarid, T., Inoue, H., 2014. Enhanced Interpretation Of Salt-Related Structures In Abu Dhabi Using Improved Seismic Data Processing And Interpretation Techniques. Presented at the Abu Dhabi International Petroleum Exhibition and Conference, OnePetro. <https://doi.org/10.2118/171837-MS>

Oldenburg, D., Li, Y., 2005. 5. Inversion for Applied Geophysics: A Tutorial. -Surf. *Geophys.* <https://doi.org/10.1190/1.9781560801719.ch5>

Paasche, H., Eberle, D.G., 2009. Rapid integration of large airborne geophysical data suites using a fuzzy partitioning cluster algorithm: a tool for geological mapping and mineral exploration targeting. *Explor. Geophys.* 40, 277–287. <https://doi.org/10.1071/EG08028>

Paasche, H., Tronicke, J., Dietrich, P., 2010. Automated integration of partially colocated models: Subsurface zonation using a modified fuzzy c-means cluster analysis algorithm. *Geophysics* 75, P11–P22. <https://doi.org/10.1190/1.3374411>

Palumbo, F., Main, I., Zito, G., 2002. The thermal evolution of sedimentary basins and its effect on the maturation of hydrocarbons. *Geophys. J. Int.* 139, 248–260. <https://doi.org/10.1046/j.1365-246X.1999.00877.x>

Pedregosa, F., Varoquaux, G., Gramfort, A., Michel, V., Thirion, B., Grisel, O., Blondel, M., Prettenhofer, P., Weiss, R., Dubourg, V., Vanderplas, J., Passos, A., Cournapeau, D., Brucher, M., Perrot, M., Duchesnay, É., 2011. Scikit-learn: Machine Learning in Python. *J. Mach. Learn. Res.* 12, 2825–2830.

Putra, A.S., Sukono, Srigutomo, W., Hidayat, Y., Lesmana, E., 2019. A Comparative Study of Simulated Annealing and Genetic Algorithm Method in Bayesian Framework to the 2D-Gravity Data Inversion. *J. Phys. Conf. Ser.* 1204, 012079. <https://doi.org/10.1088/1742-6596/1204/1/012079>

Puzyrev, V., 2019. Deep learning electromagnetic inversion with convolutional neural networks. *Geophys. J. Int.* 218, 817–832.

Raiche, A., 1991. A pattern recognition approach to geophysical inversion using neural nets. *Geophys. J. Int.* 105, 629–648. <https://doi.org/10.1111/j.1365-246X.1991.tb00801.x>

Rasht-Behesht, M., Huber, C., Shukla, K., Karniadakis, G.E., 2022. Physics-Informed Neural Networks (PINNs) for Wave Propagation and Full Waveform Inversions. *J. Geophys. Res. Solid Earth* 127, e2021JB023120. <https://doi.org/10.1029/2021JB023120>

Rossi, L., Reguzzoni, M., Sampietro, D., Sansò, F., 2016. Integrating Geological Prior Information into the Inverse Gravimetric Problem: The Bayesian Approach, in: Sneeuw, N., Novák, P., Crespi, M., Sansò, Fernando (Eds.), *VIII Hotine-Marussi Symposium on Mathematical Geodesy*, International Association of Geodesy Symposia. Springer International Publishing, Cham, pp. 317–324. https://doi.org/10.1007/1345_2015_57

Röth, G., Tarantola, A., 1994. Neural networks and inversion of seismic data. *J. Geophys. Res. Solid Earth* 99, 6753–6768. <https://doi.org/10.1029/93JB01563>

Rousseeuw, P.J., 1987. Silhouettes: A graphical aid to the interpretation and validation of cluster analysis. *J. Comput. Appl. Math.* 20, 53–65. [https://doi.org/10.1016/0377-0427\(87\)90125-7](https://doi.org/10.1016/0377-0427(87)90125-7)

Salem, A., Ali, M.Y., 2016. Mapping basement structures in the northwestern offshore of Abu Dhabi from high-resolution aeromagnetic data. *Geophys. Prospect.* 64, 726–740. <https://doi.org/10.1111/1365-2478.12266>

Sambridge, M., 1999. Geophysical inversion with a neighbourhood algorithm—II. Appraising the ensemble. *Geophys. J. Int.* 138, 727–746. <https://doi.org/10.1046/j.1365-246x.1999.00900.x>

Sambridge, M., Jackson, A., Valentine, A.P., 2022. Geophysical inversion and optimal transport. *Geophys. J. Int.* 231, 172–198. <https://doi.org/10.1093/gji/ggac151>

Sambridge, M., Mosegaard, K., 2002. Monte Carlo Methods in Geophysical Inverse Problems. *Rev. Geophys.* 40, 3-1-3–29. <https://doi.org/10.1029/2000RG000089>

Sen, M.K., Stoffa, P.L., 2013. *Global Optimization Methods in Geophysical Inversion*. Cambridge University Press, Cambridge. <https://doi.org/10.1017/CBO9780511997570>

Sen, M.K., Stoffa, P.L., 1996. Bayesian inference, Gibbs' sampler and uncertainty estimation in geophysical inversion1. *Geophys. Prospect.* 44, 313–350. <https://doi.org/10.1111/j.1365-2478.1996.tb00152.x>

Sen, M.K., Stoffa, P.L., 1991. Nonlinear one-dimensional seismic waveform inversion using simulated annealing. *Geophysics* 56, 1624–1638. <https://doi.org/10.1190/1.1442973>

Song, Y.-C., Meng, H.-D., O'Grady, M.J., O'Hare, G.M.P., 2010. The application of cluster analysis in geophysical data interpretation. *Comput. Geosci.* 14, 263–271. <https://doi.org/10.1007/s10596-009-9150-1>

Spichak, V., Popova, I., 2000. Artificial neural network inversion of magnetotelluric data in terms of three-dimensional earth macroparameters. *Geophys. J. Int.* 142, 15–26. <https://doi.org/10.1046/j.1365-246x.2000.00065.x>

Srivastava, N., Hinton, G., Krizhevsky, A., Sutskever, I., Salakhutdinov, R., 2014. Dropout: A Simple Way to Prevent Neural Networks from Overfitting. *J. Mach. Learn. Res.* 15, 1929–1958.

Tarantola, A., 2005. Inverse Problem Theory and Methods for Model Parameter Estimation, Other Titles in Applied Mathematics. Society for Industrial and Applied Mathematics. <https://doi.org/10.1137/1.9780898717921>

Thomas, R.J., Ellison, R.A., Goodenough, K.M., Roberts, N.M.W., Allen, P.A., 2015. Salt domes of the UAE and Oman: Probing eastern Arabia. *Precambrian Res.* 256, 1–16. <https://doi.org/10.1016/j.precamres.2014.10.011>

van der Baan, M., Jutten, C., 2000. Neural networks in geophysical applications. *GEOPHYSICS* 65, 1032–1047. <https://doi.org/10.1190/1.1444797>

Vatankhah, S., Renaut, R.A., Huang, X., Mickus, K., Gharloghi, M., 2022. Large-scale focusing joint inversion of gravity and magnetic data with Gramian constraint. *Geophys. J. Int.* 230, 1585–1611. <https://doi.org/10.1093/gji/ggac138>

Yang, F., Ma, J., 2019. Deep-learning inversion: A next-generation seismic velocity model building method. *GEOPHYSICS* 84, R583–R599. <https://doi.org/10.1190/geo2018-0249.1>

Yang, X., Chen, X., Smith, M.M., 2022. Deep learning inversion of gravity data for detection of CO₂ plumes in overlying aquifers. *J. Appl. Geophys.* 196, 104507. <https://doi.org/10.1016/j.jappgeo.2021.104507>

Zhang, C., Zhang, D., Wu, G., Wang, Z., Yan, J., 2019. Gravity inversion by improved iteration with variable density and its application in Xujiaweizi area. *Arab. J. Geosci.* 12, 432. <https://doi.org/10.1007/s12517-019-4573-z>

Zhang, X., Curtis, A., 2021. Bayesian Geophysical Inversion Using Invertible Neural Networks. *J. Geophys. Res. Solid Earth* 126, e2021JB022320. <https://doi.org/10.1029/2021JB022320>

Zhdanov, M.S., 2002. Geophysical Inverse Theory and Regularization Problems. Elsevier.